The Dissertation Committee for Wei Lu
certifies that this is the approved version of the following dissertation:

FABRICATION AND CHARACTERIZATION OF A DOUBLE TORSIONAL MECHANICAL OSCILLATOR AND ITS APPLICATIONS IN GOLD MICROMASS MEASUREMENTS

Committee:

____
John T. Markert, Supervisor

____
Alejandro de Lozanne

____
Maxim Tsoi

____
Qian Niu

____
David Hoffman

FABRICATION AND CHARACTERIZATION OF A DOUBLE TORSIONAL MECHANICAL OSCILLATOR AND ITS APPLICATIONS IN GOLD MICROMASS MEASUREMENTS

by

WEI LU, B.S.; M.S.

DISSERTATION
Presented to the Faculty of the Graduate School of
The University of Texas at Austin
in Partial Fulfillment
of the Requirements
for the Degree of

DOCTOR OF PHILOSOPHY

The University of Texas at Austin

December 2008

Dedicated to my wife, my daughter, my parents and my brother.

Acknowledgements

First, I would like to acknowledge my supervisor, Dr. John T. Markert for his kindness, patience, advice and endless support. During the past 6 years, I have learned a lot from Dr. Markert, the most knowledgeable advisor I have ever met. This dissertation could not have been written without Dr. Markert who not only served as my supervisor but also encouraged me throughout my academic program. He always patiently guided me through the dissertation process, never accepting less than my best efforts. Thank you, Dr. Markert!

To Markert lab members, I thank you all! I am especially thankful to Dr. Yong Lee. I really have learned so much from you. Thank you for your friendship and help you gave to me. I would never forget those hours working with you. Thank you, Yong! Best wishes to your families. I would like to thank Dr. Keeseong Park for everything you have done for me and happiness you have shared with me. I hope you and your families live happily at Suny Stony Brook. I am thankful to Dr. Utkir. When you were here, you always brought joyful time to this lab. I thank Dr. Samaresh for your help when I asked you. I wish you could make more progress in Dr. Banerjee’s group. I also would like to thank Rosie, Han-Jong, Isaac, and Mark for your very helpful support. Thank you Rosie especially for your greeting card when my daughter was born. Thank you Han-Jong for your help since you came to this lab. Thank you Isaac for your useful suggestion. I love the discussion with you, especially about Spanish soccer. Thank you Mark. Your ardor, generosity, and wisdom impress me. I greatly appreciate for support and help from each group member. I love this cooperative and friendly atmosphere in Markert lab, and I will cherish it in my memory.

I am thankful to Jack, Allan, and everyone one in machine shop. Thank you all for teaching me how to properly use each tool, for providing materials I need, and for preparing mechanical parts for me. I also would like to thank Lanny and Ed of cryogenic shop for their constant help.

I would like to thank my friends: Tianchun Zhou, Junwei Huang, Kang Luo, Zhiquan Luo, Shuqiang Yang, Junjin Bao, Shengyong Qin, Wei Zhen, Hualiang Shi, and Tianming. Getting along with you all makes my life much more joyful and colorful. Thank you all!

Lastly, I will give my gratitude to my wife, Li Sun, the most important person in my whole life. No matter what we have experienced during the past four years, I always remember the love and support you gave to me when I was in difficulties. Thank you Li, my loved one! I thank my daughter Angela. Thank you for the happiness you brought to me since your birth. I thank my parents in law, Yinsheng Sun and Suzhen Hao. Thank you for everything you have done for our family. Finally I must thank my parents Shaoquan Chen and Chunyi Lu. Thank you for bringing me to this wonderful world. Your support, love, and encouragement let me pursue my dream. Thank you! Also, I thank my elder brother, Ke Chen, thank you for your support and understanding. Thank you all, my dear families!

FABRICATION AND CHARACTERIZATION OF A DOUBLE TORSIONAL MECHANICAL OSCILLATOR AND ITS APPLICATIONS IN GOLD MICROMASS MEASUREMENTS

Publication No. _______________

Wei Lu, Ph.D.

The University of Texas at Austin, 2008

Supervisor: John T. Markert

We report the design and fabrication of a micro-mechanical oscillator for use in extremely small force detection experiments such as transverse force measurements of a moving vortex and Nuclear Magnetic Resonance Force Microscopy (NMRFM). We study the basic physics of the double torsional mechanical oscillator, and pursue double torsional oscillators with small spring constants, high resonance frequencies, and high quality factors. Using a series of semiconductor manufacturing techniques, especially using the electron-beam lithography technique, we successfully micro-fabricate double torsional mechanical oscillators from silicon-on-insulator wafers. We conduct characterization experiments to extract important parameters of a mechanical oscillator, including the resonance frequencies, spring constants, and quality factors. We focus on

the four typical resonance modes of these oscillators, and then compare the force detection sensitivity of each mode. Eventually we apply these force sensitive oscillators to gold micro-mass measurements, and achieve very small mass detection.

In the future we are going to continue to micro-fabricate thinner oscillators to reduce the spring constants, and improve the quality factors by designing more suitable geometric shapes and by pursuing annealing studies. Thus, we might be able to achieve single nuclear spin measurements using NMRFM.

Table of Contents

List of Figures

Chapter 1 Introduction of Mechanical Oscillator

Micromechanical oscillators are commonly used for detection of small forces in micro-electromechanical sensors and in scientific instruments. One of the typical mechanical oscillators in scientific measurements is the mechanical cantilever used in the Atomic Force Microscopy (AFM). It has a pyramid tip on the free end, which is used to make a contact with the surface of the sample to be measured. Many of these micro-fabricated oscillators are capable of measuring surprisingly small forces, thus they have numerous applications, especially in Scanning Probe Microscopy (SPM), including Atomic Force Microscopy (AFM), Magnetic Force Microscopy (MFM), etc.

The mechanical oscillators in our lab are primarily used in two research projects. One is the measurement of the transverse force [1] acting on a moving vortex of a superconducting sample. An electromagnet is mounted so that its north and south pole are on opposite sides of a superconducting sample attached to a mechanical oscillator. Magnetic flux lines thus go through the sample. The electromagnet is driven at the resonance frequency of the mechanical oscillator. As the magnet moves, the vortices in the superconducting sample are either dragged with it or, if pinned, stretched by the motion. For pinned vortices, the oscillator can measure the pinning force directly. Vortices in motion will feel a viscous force parallel to the motion and a transverse force perpendicular to it. For vortex motion perpendicular to the oscillator motion, the transverse force will excite the oscillator. Thus, from the measurement of the excitation amplitude of the oscillator, we can detect the transverse force the vortices experience. A second project is an exciting and pioneering field----Nuclear Magnetic Resonance Force Microscopy (NMRFM). In 1992, Rugar et al. [2-3] initiated the basic experimental setup for NMRFM, which included the key component in this extremely precise measurement----the micro-mechanical oscillator. In this experiment, an extremely small force will be created by the interaction between the magnetic field gradient and the oscillating magnetization of the sample attached to the mechanical oscillator. The detection of this small force requires that the mechanical oscillator has very high force detection sensitivity, especially for the future goal of single nuclear spin detection. Micro-fabricated mechanical oscillators are the ideal candidates for such force detections. Since then, many groups [4-9] have focused on the design and the fabrication of force sensitive mechanical oscillators.

In this dissertation, I will show the basic physics of the mechanical oscillator in Chapter 2, including the typical vibration modes of mechanical oscillators, and I will describe the typical experiments for their characterizations. The design of an oscillator is our first step, and next we implement our design. Thanks to the advanced techniques developed in the modern semiconductor manufacturing industry, we are able to micro-fabricate oscillators with very small sizes to meet the experimental requirements. In Chapter 3, I show in detail how to micro-fabricate mechanical oscillators using a series of techniques applied to Micro-Electro-Mechanical Systems (MEMS). This is the most tedious part of our whole story. In Chapter 4, I discuss our 3-dimensional positioning control system based on the commercial Attocube design, which is a very critical component in our whole experiments. In Chapter 5, I give the characterization results of our fabricated oscillators. In the last chapter, I show how to apply a mechanical oscillator to do evaporated gold particle micromass measurements, and then I summarize our work and propose future research.

Chapter 2 Mechanical Oscillator

In this chapter we review the basic physics of mechanical oscillators and show how to characterize mechanical oscillators using the fiber optical interferometry.

2.1 Introduction to mechanical oscillators

A mechanical oscillator's motion can be modeled using the following equation of motion:

$$m\frac{d^2x}{dt^2}+r\frac{dx}{dt}+kx=F_0\cos(\omega t) \tag{2.1}$$

where m, r, k, F_0, and ω are the mass of the mechanical oscillator, the effective viscosity constant due to both internal losses and friction of the medium through which the oscillator moves, the spring constant of the mechanical oscillator, the amplitude of the external driving force, and the driving frequency, respectively. The general solution to this differential equation can be written as:

$$x=Aexp\left(-\frac{r}{2m}t\right)sin\left(\omega' t+\varphi_h\right)+Bcos\left(\omega t-\varphi\right) \tag{2.2}$$

Where A and B are the amplitudes of the transient solution and the steady state solution, respectively. The transient term is deprived on the initial position and the velocity of an oscillator, while the steady state term is deprived on the driving force. The transient solution is the solution to the homogeneous differential equation of motion, which has been combined with the particular solution and required to fit the physical boundary conditions of the problem. The form of this transient solution is that of the undriven damped oscillator and as such can be under-damped, over-damped, or critically damped. The frequency of the transient part is given by:

$$\omega' = \sqrt{\omega_0^2 - \frac{r^2}{4m^2}} \quad , \tag{2.3}$$

and the resonance frequency of a harmonic oscillator can be written as:

$$\omega_0 = \sqrt{\frac{k}{m}} \tag{2.4}$$

Since the transient solution will go away with time, we are only interested in steady solution. The steady solution has the following expression:

$$B = \frac{F_0 / m}{\left[\left[\omega_0^2 - \omega^2 \right]^2 + \frac{r^2}{m^2} \omega^2 \right]^{\frac{1}{2}}} \tag{2.5}$$

The phases of the steady solution is:

$$\varphi = tan^{-1}\left[\frac{r\omega}{k - m\omega^2} \right] \tag{2.6}$$

From the equation 2.6, we can see that when the external driving frequency is exactly equal to the resonance frequency of the harmonic oscillator, then there is a 90° phase shift between the driving force and the steady state response. And the frequency response of the amplitude of the harmonic oscillator to the external driving force

$$B = \frac{F_0 / m}{\left[\left[\omega_0^2 - \omega^2 \right]^2 + \frac{r^2}{m^2} \omega^2 \right]^{\frac{1}{2}}}$$

is a Lorentzian function. When we plot this function, we have the following figure:

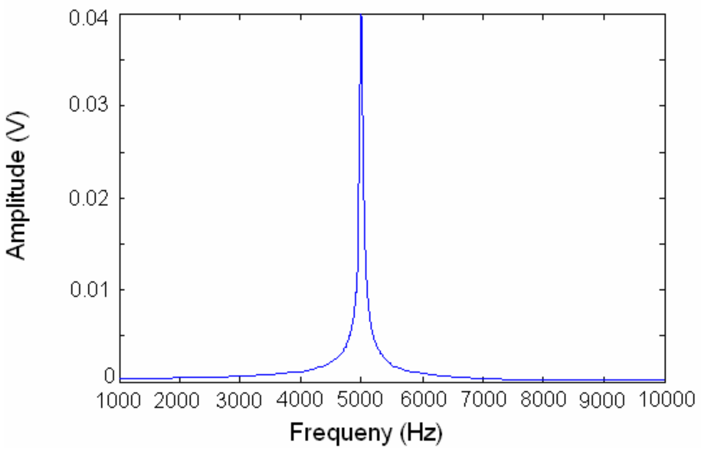

Fig. 2.1: The frequency response curve of the oscillator. In this figure, we plot a typical Lorentzian curve with the resonance frequency of 5 kHz and the amplitude of 0.04 V.

Once the external driving frequency is equal to the resonance frequency of the harmonic oscillator, the oscillation amplitude will go to the maximum value. Besides that, the degree of sharpness of the Lorentzian curve can be determined by one important parameter----the quality factor *Q,* which can be expressed as the ratio of the resonance frequency to the full frequency width at the $\frac{1}{\sqrt{2}}$ amplitude of the resonance peak. In Fig. 2.2, we demonstrate the definition of the quality factor.

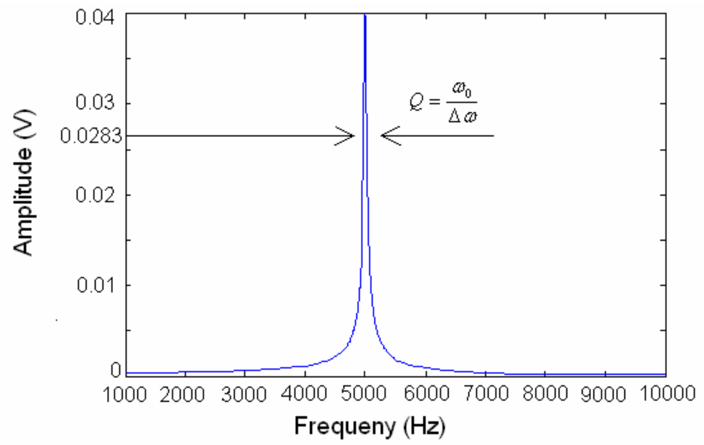

Fig. 2.2: One Q value definition.

The quality factor is a dimensionless parameter that also compares the time constant for decay of an oscillating physical system's amplitude to its oscillation period. Equivalently, it compares the frequency at which a system oscillates to the rate at which it dissipates its energy. The higher *Q* indicates the lower rate of energy dissipation relative to the oscillation frequency, so the oscillations die out more slowly. From this point of view, quality factor can also be defined as:

$$\mathrm{Q} = 2\pi \frac{Energy \quad Stored}{Energy \quad Lost \quad per \quad cycle} \tag{2.7}$$

The quality factor can be affected by several processes [8-12]. The inverse of the quality factor is a measure of energy lost, and energy losses from different processes add up to the total energy loss. So we can express the Q value as:

$$\frac{1}{\mathrm{Q}} = \frac{1}{\mathrm{Q}_{\mathrm{Air}}} + \frac{1}{\mathrm{Q}_{\mathrm{Base}}} + \frac{1}{\mathrm{Q}_{\mathrm{TED}}} + \frac{1}{\mathrm{Q}_{\mathrm{Volume}}} + \frac{1}{\mathrm{Q}_{\mathrm{Surface}}} \tag{2.8}$$

The five terms on the right hand side of Eq. 2.9 represent the energy dissipation through air friction, base connection, thermoelastic mechanism, bulk volume internal friction, and surface friction. For example, a pendulum suspended from a high-quality bearing, oscillating in the air, would have a high *Q*, while a pendulum immersed in oil would have a low one. The same thing happens to the mechanical oscillator here---the oscillator in the air will have much lower quality factor than the oscillator in a high vacuum. We are going to show how the vacuum affects the Q value later in this chapter. For the other factors, we can increase the Q value by designing specific geometric shapes and fixing the defects inside the silicon volume and on the silicon surface. The double torsional mechanical oscillator has a particular geometric design as follows:

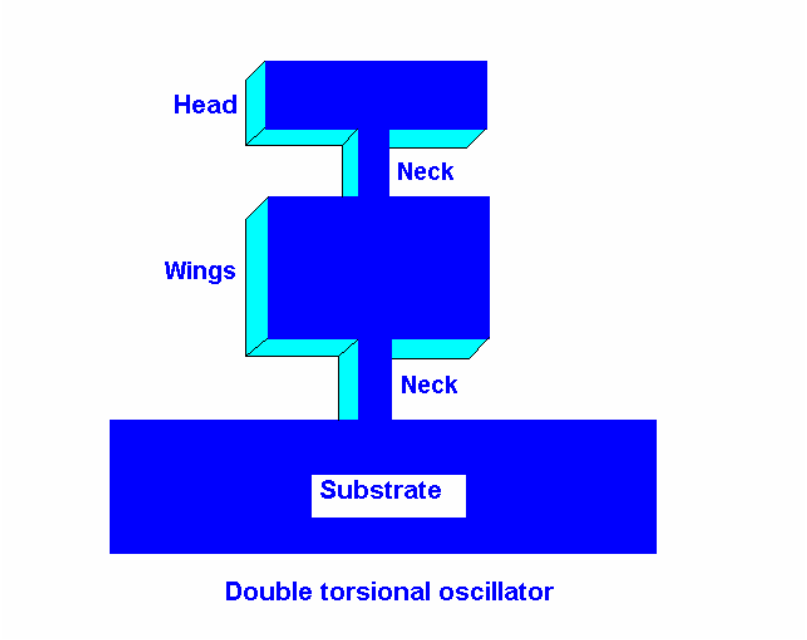

Fig. 2.3: The geometric shape of the double torsional mechanical oscillator.

To reduce energy losses through the base connection can be achieved by isolating the oscillator energy mostly in the head. In the antisymmetric mode, the head and wings rotate in opposite directions. Due to the conservation of angular momentum, the relationship between the angular momentums of the head and the wing of the oscillators can be equated [16]:

$$I_h \omega_h = I_w \omega_w \tag{2.9}$$

And the kinetic energy of the head and the wing of the oscillator is:

$$\begin{cases} \text{Head}: E_h = \frac{1}{2} I_h \omega_h^2 \\ \text{Wing}: E_w = \frac{1}{2} I_w \omega_w^2 \end{cases}, \tag{2.10}$$

where I_h, I_w are the moment of inertia of the head and wing, respectively. So we can rewrite the relationships as:

$$E_h = \frac{I_h^2 \omega_h^2}{2I_h}, \qquad E_w = \frac{I_w^2 \omega_w^2}{2I_w}. \tag{2.11}$$

Then we can easily get the following relationship based on Eq. 2.10:

$$E_h I_h = E_w I_w \tag{2.12}$$

From the above equation we can see that if we want $E_h >> E_w$, we have to make sure that: $I_h << I_w$. Since the moment of inertia is a function of the mass distribution of the oscillator about the rotation axis, a smaller width and a smaller height would produce the smaller moment of inertia. This is the reason why we prefer the double torsional geometric shape with a small head and a big wing.

Now let's estimate the frequencies of the double torsional oscillator. The motions of the head and the wing can be simplified as:

$$\begin{cases} m_h \frac{d^2 x_h}{dt^2} + k x_h + k(x_h - x_w) = F \exp(i\omega t) \\ m_w \frac{d^2 x_w}{dt^2} + k(x_w - x_h) = F \exp(i\omega t) \end{cases} \tag{2.13}$$

Where, m_h, m_w, x_h, x_w and k represent the mass of the head, mass of the wing, bending amplitude of the head and bending amplitude of the wing, respectively. Using linear algebra, we can get the characteristic equation from which we can get the analytical expression of the resonance frequencies of the oscillator. For torsional mode, replace m_h, m_w, x_h, x_w, and k by I_h, I_w, θ_h, θ_w and κ. Here I_h, I_w, θ_h, θ_w and κ are the moment of inertial of the head, moment of inertial of the wings, torsional angle of the head, torsinla angle of the wings, and the torsional spring constant, respectively .

These equations allow us to reasonable estimate of the resonance frequencies. If we want to get accurate resonance frequency predictions, we have to use a more precise numerical calculation. The ANSYS finite element method is the ideal software to do this job. It can provide a good reference for our further mechanical oscillator design and fabrication. Generally, we are interested in the following four vibration modes: 1) lower symmetric cantilever mode, 2) lower symmetric torsional mode, 3) upper antisymmetric cantilever mode, and 4) upper antisymmetric torsional mode.

I) Lower Cantilever Mode

In this vibration mode, the head and the wing are bending back and forth in the same way. This vibration behavior is called in phase. This mode usually has the lowest resonance frequency among these four modes. Also the quality factor is the lowest. We did the ANSYS finite element analysis to simulate the oscillator vibration. A demonstration is shown in Fig. 2.4-1.

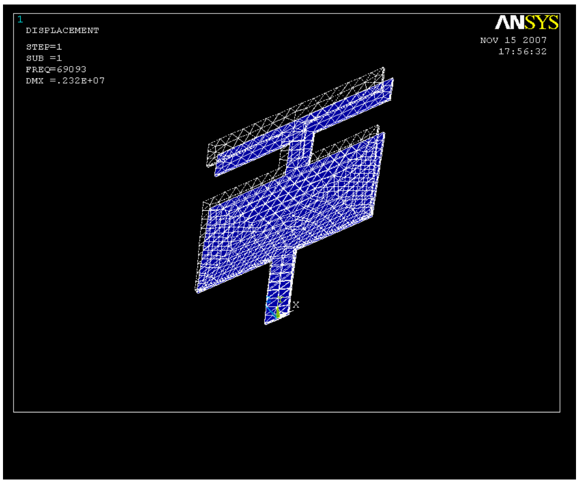

```
1
DISPLACEMENT
STEP=1
SUB =1
FREQ=69093
DMX =.232E+07
```

```
ANSYS
NOV 15 2007
17:56:32
```

Fig. 2.4-1: Lower Cantilever mode.

II) Lower Torsional Mode

In this vibration mode, instead of bending back and forth, the head and the wing are twisting about their symmetry axis----the oscillator’s neck. In this case, they are both rotating in the same rotation direction-----an in-phase rotation. This mode usually has a higher resonance frequency than the lower cantilever mode. The quality factor is often slightly higher also. A demonstration is shown in Fig. 2.4-2.

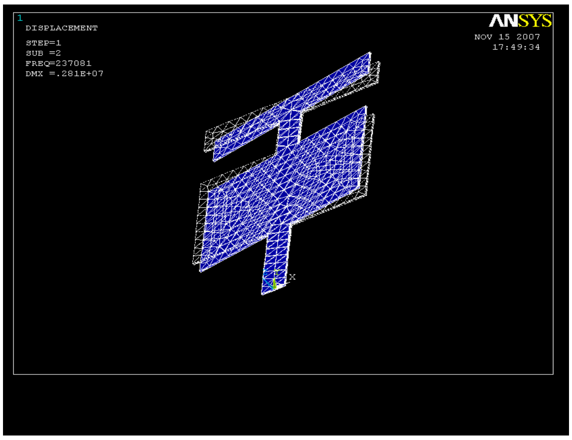

Fig. 2.4-2: Lower Torsional Mode.

III) Upper Cantilever Mode

In this mode, instead of bending back and forth in phase like the lower cantilever mode, the head and the wing are bending out of phase------they are bending in opposite directions all the time. This mode has an even higher resonance frequency and quality factor than the two lower modes. A demonstration is shown in Fig. 2.4-3.

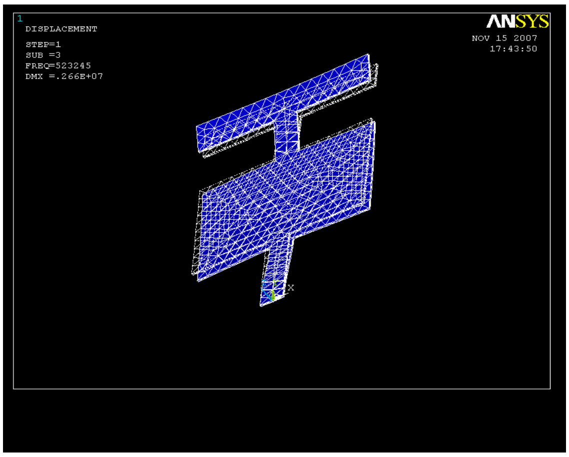

Fig. 2.4-3: Upper Cantilever mode.

IV) Upper Torsional Mode

In this mode, the head and the wing are twisting out of phase about the oscillator’s neck. A demonstration is shown in Fig. 2.4-4.

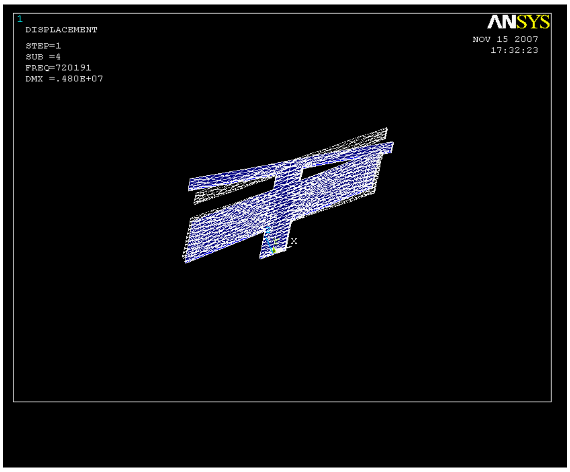

Fig. 2.4-4: Upper Torsional Mode.

This mode normally has the highest resonance frequency and quality factor among these four vibration modes. As discussed above, the higher quality factor results from the reduced losses through the base connection due to the fact that most energy is isolated in the head.

2.2 Oscillator characterization experiments

An oscillator's vibration can be very precisely measured by a fiber optical interferometer. Before going through every experiment, let's first explain the basic principle behind the fiber optical interferometer. In the fiber optical interferometer, a laser beam traveling through the fiber will be partially reflected internally at the interface between the fiber end and the vacuum before it is transmitted out of the fiber. The amount of the reflected beam significantly depends on the cleave quality of the fiber end. The theoretical calculation using Maxwell equation tells us that the highest reflected laser beam is 4% of the intensity of the incident beam, for the index of refraction of fiber is equal to 1.5. In our experience the best cleave can give us a reflected beam of only 3% of the incident intensity. The transmitted laser light will keep traveling until it hits the target----the mechanical oscillator, and then it will be reflected (the 2nd reflection) at the oscillator surface. With proper alignment, most of the second reflected beam will enter back into the fiber. This externally reflected laser light will interfere with the internally reflected beam since these two light waves have a path difference. Remember the second laser beam comes out from the fiber and hits the oscillator, and then is reflected back into the fiber, thus it actually travels more distance than the internally reflected one by twice the cavity length, which gives rise to the phase difference between these two beams and generates the interference pattern we observe. Obviously the interference pattern is a function of the cavity length, thus we can read out the cavity length change from the change of the intensity of the interference fringe. Since the interference fringe has a spacial period equal to half of the wavelength of the laser (we are going to demonstrate this later), a very precise measurement of the vibration of the oscillator can be achieved-----a sub-nanometer scale vibration can be detected.

2.2.1 Experiment setup

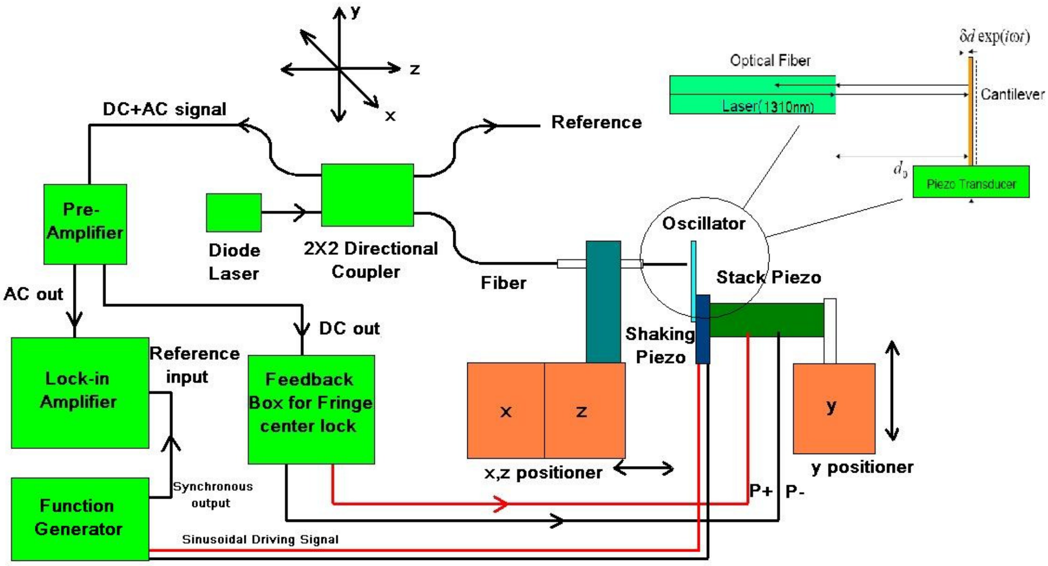

Fig. 2.5: Experiment setup for oscillator characterization.

The basic experiment setup is shown in the above figure. The upper right part is the fiber optic interferometer which measures the tiny motion of the oscillator. The fiber transmits the infrared laser light from a diode laser with wavelength of 1310 nm into a 2x2 directional coupler (Gloud, series number: 439530). The infrared laser is generated by a laser diode (PD-LD Inc, Series number: 276447) which is powered by a home-made adjustable DC current source. The infrared laser has a power of 10 mW and is coupled to the single mode 9/125 fiber ($9\,\mu\text{m}$ core diameter and $125\,\mu\text{m}$ clad diameter), and then is sent into a 2x2 directional coupler. The directional coupler has four optical fiber arms.

First of all, it receives the incident laser from the laser diode through one input and then split it into two components, one of which (10%) is a detection beam-----it goes through a fiber and hits the oscillator. The rest 90% goes through the third way to the vacuum as a reference. The two reflected beams will interfere with each other and travel through the fourth way----the output to the external photodiode. We use an InGaAs (PD-LD Inc, series number: 277666) photodiode to convert the light signal from the fiber output to a current signal; after that, the small current signal is converted further to a voltage signal by a current-voltage converter with a certain conversion factor determined by the gain resistor. This voltage signal consists of both AC and DC. As we mentioned before, the DC component is due to the cavity length between the fiber end and the oscillator surface, while the AC component is due to the vibration of the oscillator, which will change the cavity length a little bit with time, and thus produce the time varying signal. The thermal noise in the chamber or the external sinusoidal signal we apply will give rise to the AC signal in the interference fringe. We feed the AC signal to the input of a Stanford Research Systems SR830 or SR844 lock-in amplifier, and feed the DC signal to the fringe center lock feedback circuit, respectively. We are going to talk about fringe center lock feedback circuit later in this chapter. Whether we use the SR830 or the SR844 lock-in amplifier depends on the oscillator's resonance frequencies. For the oscillator with the resonance frequencies below 100 kHz, we can choose both the SR830 and the SR844 (however the SR844 lock-in has a minimum detectable frequency of 25 kHz), while for the oscillators with the high resonance frequencies, above 100 kHz, the SR844 lock-in amplifier is the only choice. The lock-in amplifier from the Stanford Research System (SRS) is a useful instrument to measure the very small voltage signal. The basic principle behind this instrument is that it implements small signal detection by multiplying the detected signal and a reference signal and then using a low-pass filter to filter most mixed to pass only the frequency difference signal which contains the signal we wish to measure. It can use either an internal reference oscillator signal or an external periodic signal to provide the reference signal. Multiple time constant options corresponding to different measurement bandwidths make frequency measurement very flexible and precise.

2.2.1-1. Fiber optical interferometer

Now let's examine the interference pattern in detail. Assume the intensity of the incident laser is I_0. The interference picture can be demonstrated as below:

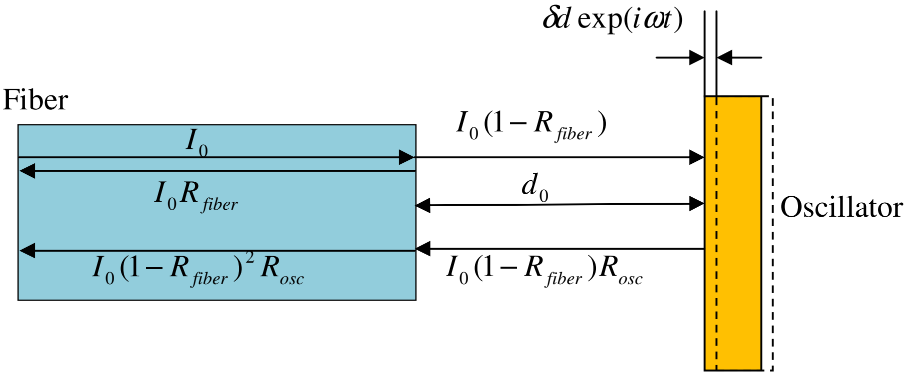

Fig. 2.6: The demonstration of the fiber optical interferometer.

Where R_{fiber} and R_{osc} are the reflection coefficients of the cleaved fiber end and the oscillator surface, respectively. From the figure above, the internal reflected beam can be written as I_0R_{fiber}, the transmitted laser beam back into the fiber from the oscillator surface reflection is $I_0(1-R_{fiber})^2R_{osc}$. Here, we make two assumptions: 1) all laser lights get back in the fiber; 2) R_{fiber} is the same from both sides of the fiber end. We will see that these two assumptions do not affect the relationship between the interference signal and the cavity length. Since the second laser beam is bounced between the fiber end and the oscillator surface, it travels more by twice the cavity length. Thus, the phase difference between these two beams is given by [8]:

$$\varphi = \pi + \frac{4\pi}{\lambda} d_0 + \frac{4\pi}{\lambda} \delta d \exp(i\omega t) = \varphi_0 + \frac{4\pi}{\lambda} \delta d \exp(i\omega t), \tag{2.15}$$

where $\varphi_0 = \pi + \frac{4\pi}{\lambda} d_0$. This phase difference will result in the interference intensity:

$$\begin{aligned} I &= I_0 R_{fiber} + I_0 (1 - R_{fiber})^2 R_{osc} + 2\sqrt{I_0 R_{fiber}} \sqrt{I_0 (1 - R_{fiber})^2 R_{osc}} \cos\varphi \\ &= I_0 [R_{fiber} + (1 - R_{fiber})^2 R_{osc} + 2(1 - R_{fiber}) \sqrt{R_{fiber} R_{osc}} \cos(\varphi_0 + \frac{4\pi}{\lambda} \delta d \exp(i\omega t))] \\ &= I_0 [R_{fiber} + (1 - R_{fiber})^2 R_{osc}] + 2 I_0 (1 - R_{fiber}) \sqrt{R_{fiber} R_{osc}} \cos(\varphi_0 + \frac{4\pi}{\lambda} \delta d \exp(i\omega t)) \\ &= I_0 [R_{fiber} + (1 - R_{fiber})^2 R_{osc}] + 2 I_0 (1 - R_{fiber}) \sqrt{R_{fiber} R_{osc}} \\ &\quad \times [\cos\varphi_0 \cos(\frac{4\pi}{\lambda} \delta d \exp(i\omega t)) - \sin\varphi_0 \sin(\frac{4\pi}{\lambda} \delta d \exp(i\omega t))] \end{aligned} \tag{2.16}$$

Since the vibration amplitude of the oscillator is typically much smaller than the wavelength of our infrared laser (1310 nm), we have: $\delta d << \lambda$, thus $\frac{4\pi}{\lambda} \delta d << 1$, so we can approximate the above equation as:

$$\begin{aligned} I = I_0 [R_{fiber} + (1 - R_{fiber})^2 R_{osc}] + 2 I_0 (1 - R_{fiber}) \sqrt{R_{fiber} R_{osc}} \\ \times [\cos\varphi_0 - \frac{4\pi}{\lambda} \delta d \exp(i\omega t) \sin\varphi_0] \end{aligned}$$

$$
\begin{aligned}
&= I_0[R_{fiber} + (1-R_{fiber})^2 R_{osc} + 2(1-R_{fiber})\sqrt{R_{fiber}R_{osc}}\cos\varphi_0] \\
&\quad - 2I_0(1-R_{fiber})\sqrt{R_{fiber}R_{osc}}\,\frac{4\pi}{\lambda}\delta d\sin\varphi_0\exp(i\omega t) \\
&= I_{DC} + I_{AC}\exp(i\omega t)
\end{aligned}
\tag{2.17}
$$

where

$$
\begin{cases}
I_{DC} = I_0[R_{fiber} + (1-R_{fiber})^2 R_{osc} + 2(1-R_{fiber})\sqrt{R_{fiber}R_{osc}}\cos\left(\pi + \frac{4\pi}{\lambda}d_0\right)] \\
I_{AC} = -2I_0(1-R_{fiber})\sqrt{R_{fiber}R_{osc}}\,\frac{4\pi}{\lambda}\delta d\sin\varphi_0
\end{cases}
\tag{2.18}
$$

From Eq. 2.18, we can see that: the DC interference signal I_{DC} is a sinusoidal function of the cavity length d_0 with a DC offset of $I_0[R_{fiber} + (1-R_{fiber})^2 R_{osc}]$ and a period of $\frac{\lambda}{2}$, while the AC signal has an amplitude of I_{AC}, which is linear with δd, the vibration amplitude of an oscillator.

2.2.1-2 Interference Fringe Lock Box

If we plot the interference versus cavity length d_0, we have the following figure:

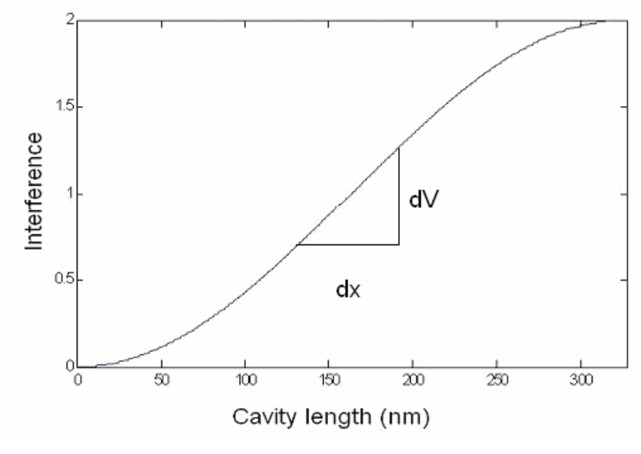

Fig. 2.7: The interference fringe versus the cavity length.

When we change the spacing between the fiber and the oscillator, we can observe the interference fringes. In order to vary the spacing, we changed the DC voltage applied on the stack piezo with oscillator attached. Here we home built a fringe center locking feedback box. This feedback box is powered by ± 15 volts DC power supplies. With an adjustable resistor built in, this feedback box can output the DC voltage varying from +15 volts to -15 volts to the stack piezo. As a result, the piezo will extend or shrink depending on the voltage applied; thus, the oscillator attached in the front will be pushed or pulled accordingly. By doing this, we can readily change the cavity length between the oscillator and the optical fiber. Before we do the measurement, we need to lock onto the center position of the fringe. The reason for this is because around the center of the fringe the interference intensity is almost linear with the cavity length. By differentiating the first of Eq 2.18, we can see that the slope at the center of the fringe is:

$$\frac{dV}{dx} = \frac{4\pi}{\lambda}\left(V_{con} - V_{des}\right) \quad , \tag{2.19}$$

where V_{con}, V_{des} are the constructive (maximum) and destructive (minimum) points on the interference fringe. Rewriting this equation, we have:

$$dx = \frac{dV}{\frac{4\pi}{\lambda}\left(V_{con} - V_{des}\right)} \quad . \tag{2.20}$$

So a tiny change on the cavity length dx can be read out in terms of the interference fringe change dV. When we find the center position of the fringe, we turn on the fringe locking feedback box. Any shift from the center fringe can be sent back into this box as a feedback signal. After receiving the feedback signal, the inside inverting operational amplifier will output a voltage signal with an opposite sign to the stack piezo so that the original shift from the center fringe can be canceled. Thus we can stay on the center fringe very stably. For a schematic drawing and a description of the usage of the fringe locking feedback, please check Appendix A where you can find more details.

2.2.1-3 3-D attocube positioner

One of the greatest concerns for a fiber optical interferometer is alignment. Successful interference measurements depend on how well you have achieved the alignment of the optical fiber and the mechanical oscillator. The optical fiber has an outer cladding diameter of 125 μm with a core whose diameter is around 9 μm. The dimension of our mechanical oscillator is about 50μm~120μm. Usually a 10 μm spacing between the fiber and the oscillator can give us very notable interference signal. So accurate interference measurements require very precise alignment of the fiber and the oscillator. Recently, we have assembled a system based on the attocube positioning control system (Fig 2.8).

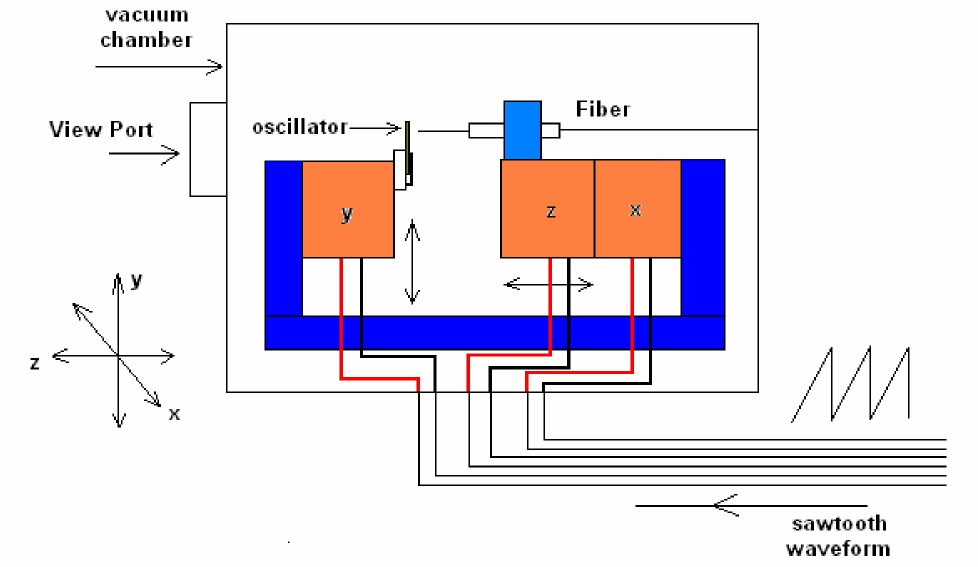

Fig. 2.8: Schematic drawing of the 3-D attocube positioning control system.

We have applied this positioning system to our fiber interferometer experiments, and successfully met the rigorous alignment requirements. With the aid of the stack piezo electrical actuator circuits driven by our home-made sawtooth function generator, we have achieved positioning control for the fiber and the oscillator with a nanometer resolution. We will discuss the details of the attocube-like alignment control system in Chapter 4.

2.2.1-4 Photodiode

The interference signal has to be converted into an electrical signal so that it can be detected by the lock-in amplifier. In our setup we used a simple op-amp photodiode circuit ([14], [16]) to perform this job. The schematic circuit is shown in Fig 2.9.

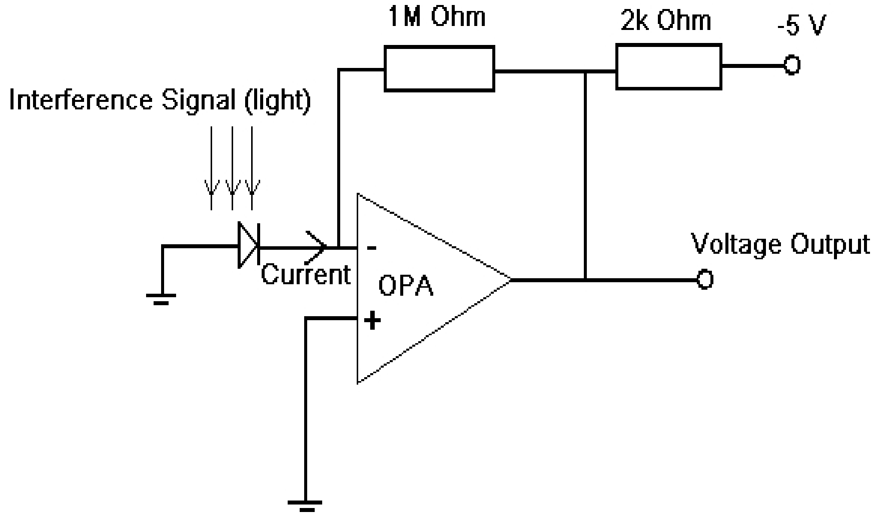

Fig. 2.9: Photodiode with current to voltage converter.

The interference signal from the 2×2 directional coupler is converted into a current signal by our InGaAs photodiode (PD-LD Inc, series number: 277666). This current is converted again, into a voltage signal, by a current-to-voltage converter, which is implemented by an operational amplifier OPA 395. The gain resistor in the feedback loop can amplify the small interference signal to a notable level. For example, the 1MΩ resistor converts a 1PA current to a 1 μV voltage. The circuit includes a DC bias (the –5 V supply and 2 kΩ resistor). The purpose of this reverse bias is to avoid the too big output voltage which is beyond the output range of OPA 395.

2.2.1-5 Function generator

For the driven scan and decay experiments we are going to discuss later, we used the Hewlett Packet HP3325B or the Standford Research Systems DS345 function generator to feed a sinusoidal driving voltage to our shaking piezo to externally drive the mechanical oscillator. The synchronous output can provide the reference signal to the lock-in amplifier to tell the lock-in to "take a look at" a specific frequency signal. Both the function generator and the lock in amplifier are controlled by Labview programs via the GPIB or RS232 interfaces. The GPIB is a parallel port, while the RS232 is series port. So the communication through GPIB is much faster than RS232. But for GPIB usage, you need a GPIB card in your computer. RS232 interface is much easier to build up by yourself. You can home make a DB9 to DB25 cable. Most measurement instruments have the build-in RS232 interfaces on their rear panels. Their DB25 to DB9 connections could be different depending on the Data Terminal Equipment (DTE) or the Data Communications Equipment (DCE) setting (check the Appendix for the details). Before you make the connection cable, please check the instruction manual about RS232 connection for each instrument. Plug the DB25 end to the RS232 connection on the measurement instrument, and then plug the other DB9 end to the COM port with 9-pin male connection on your computer. After correctly setting up the communication modes (GPIB or RS232) for the measurement instruments, we successfully establish the communication between the computer and the instruments. Automation test and measurements are ready. For the interface setup and the Labview program, please check the content in Appendix A.

2.2.1-6 Lock-in amplifier

As we introduced previously, the lock-in amplifier can detect the interference signal from the photodiode with I-V converter. For the use of the lock-in, you have to correctly set the time constants for the different built-in filters. For the filter with 6dB/octave, the equivalent noise bandwidth is related to the time constant by: $\Delta\nu = \frac{1}{4T}$, where $\Delta\nu$ and T are the bandwidth and the time constant of the lock-in, respectively (Check the instruction manual). The bigger time constant you choose, the longer time the lock-in needs to respond to an external change. The lock-in measures the root mean square (RMS) values over the time constant period within the bandwidth $\Delta\nu$. We will discuss RMS noise signal later. When we do a frequency scan, the time interval between frequencies should be 3~4 times the time constant so that the lock-in has enough time to respond to the new frequency.

2.2.2 Experiments

Once all of the instruments are ready, we can start the characterizations of our mechanical oscillators. The most important parameters we are going to measure are resonance frequencies, quality factors, and spring constants of various mechanical oscillator modes. Next we show the typical measurement methods used to extract these parameters.

2.2.2-1 Driven Scan

For resonance frequency measurement, a driven scan is a very basic and effective method. From the equation of motion of the mechanical oscillator, we can see that when we apply an external force to drive the oscillator at different frequencies, the oscillator will vibrate with different amplitudes. When the driving force has the same frequency as the resonance frequency of the oscillator, the oscillator will be vibrating with maximum amplitude. Using the fiber optical interferometer, the vibration amplitude can be easily detected in terms of the interference signal. As we said in section 2.1, when we sweep the frequency, the vibration amplitude has a Lorentzian lineshape. In the experiment, we externally drive the shaking piezo plate, and then the shaking piezo translates the vibration force to the oscillator. The AC signal from the interferometer is fed into the input of the lock-in amplifier and detected. The measured voltage signal from the lock-in output can be instantaneously shown by the Labview program. For details about the graphic user interface and the design of the driven scan Labview program, please see Appendix B. Once we finish one driven scan measurement, we typically use an Igor or Origin program to do the curve fitting of the raw data to extract the resonance frequencies and quality factors of the oscillator. These programs are shown in Appendix B. Fig 2.10

shows the typical Lorentzian response of the oscillator to the driving force. Fig 2.11 shows the corresponding Lorentzian curve fitting.

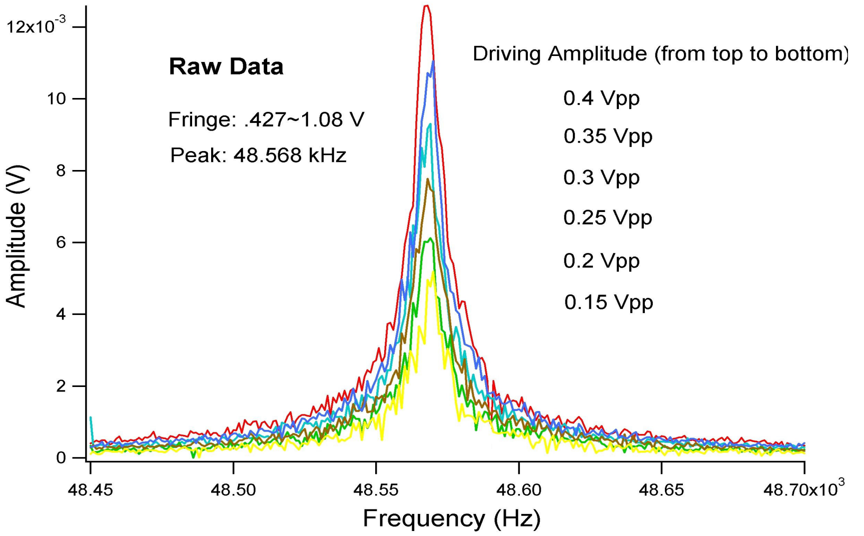

Fig. 2.10: The driven scan of the oscillator.

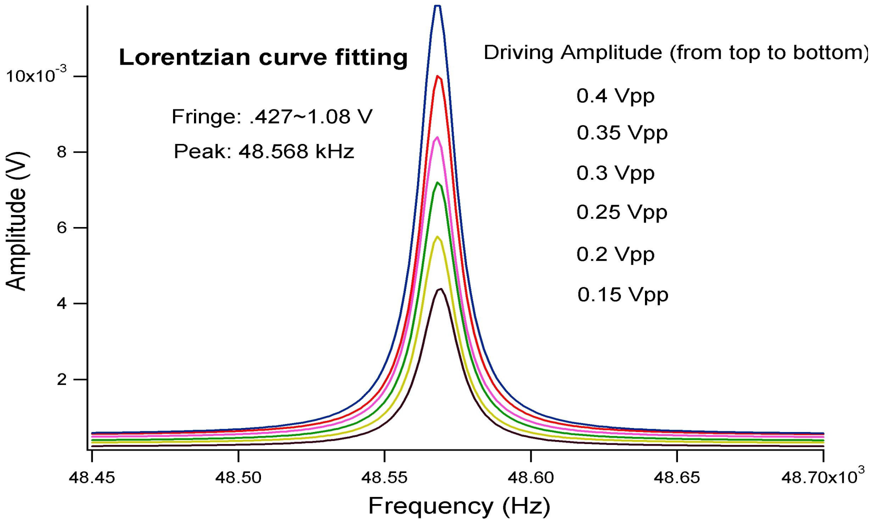

Fig. 2.11: Lorentzain curve fitting of the driven scan.

One effective method to check whether a frequency response is real or not is to change the magnitude of the driving force. As shown in Figs. 2.10 and 2.11, we got those five curves with different driving amplitudes from the function generator. When we increased the driving amplitude, the vibration amplitude of the oscillator increased as well. The resonance frequency doesn’t change. Please be careful about the driving force. Do not use a driving amplitude from the function generator that is too large, otherwise the fragile oscillator could be broken. Another reason for that is we need to keep the driving amplitude low to stay in the linear part of the fringe.

When we introduced the quality factor in this chapter, we said the vacuum level will affect the quality factors very directly. In the following figure, we demonstrate how the quality factor of the oscillator depends on the vacuum level.

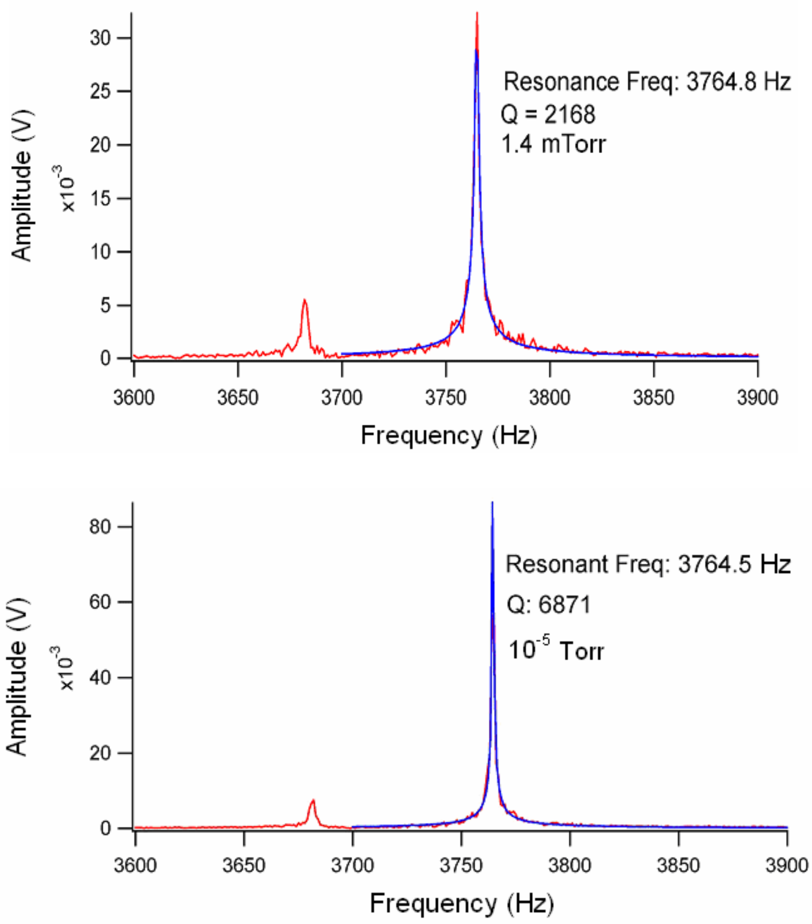

Fig. 2.12: Quality factor goes higher as we enhance the vacuum level.

We measured the Q values with the same driving amplitude in the two vacuum levels. At the low vacuum, we measured the Q value. And then we turned on the diffusion pump and achieved a higher vacuum. We measured the Q value of the same resonance again, and got a Q about 3 times as big as the one we measured at the low vacuum. From the curve fitting, we calculate the amplitudes of these two peaks. Also, we find the amplitude increases by factor of 3 at high vacuum. This is easy to explain: when the air pressure inside the chamber decreases, the air friction will also decrease. So the energy of the oscillator will be less dissipated to the surrounding environment, and thus the quality factor achieves a higher value. Because the oscillator experiences less viscosity, it can vibrate with a bigger amplitude under the same driving force.

Another purpose of the driven scan measurements is that we can figure out the vibration mode at each specific resonance frequency. To determine the vibration mode of the oscillator, we run the frequency sweep and then refer to the simulation results from the finite element analysis to determine which one is which. Beside this, there is another very reliable method to do this job. That method is to check the phase behavior of the X and Y outputs from the lock-in amplifier at the different positions on the same oscillator. In the following three figures from the top to the bottom, we showed the X and Y outputs when we detected the different position on the oscillator (illustrated by the dot). First, we took the measurement on the right side of the wing, and then we moved up to the right side of the head to check the phase behavior, and finally we went to the left side to end our measurements. As we can see, the phase behaviors at two sides of the oscillator are different. That is because the vibration is shifted by 180 degrees on one side with respect to the other. This is due to a torsional vibration. And then we also checked the phase behavior on the left side of the head, we got the same phase relation between the X and Y as the left wing. This demonstrated that the head and wing are twisting in phase.

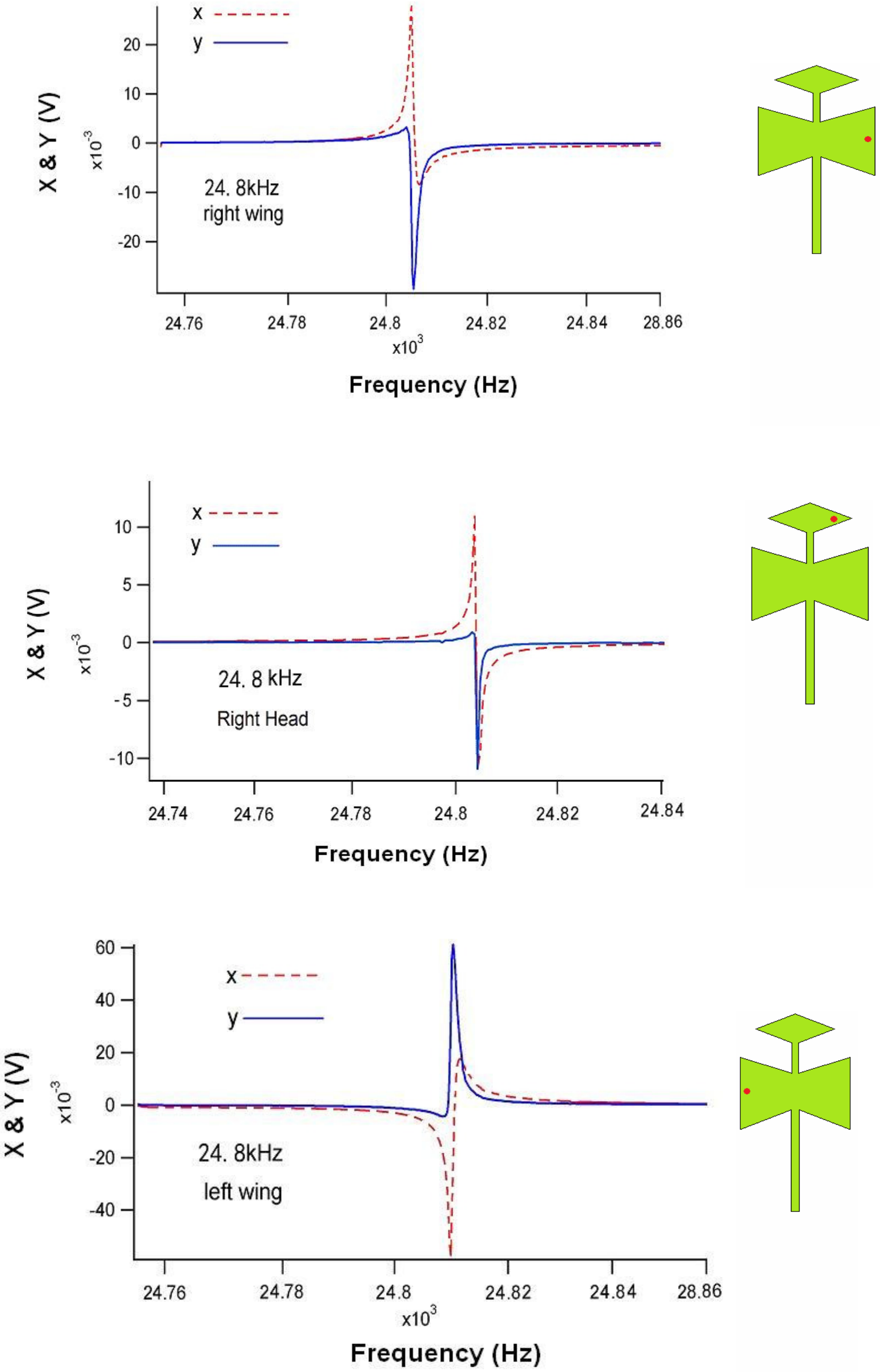

Fig. 2.13: The phase behavior of the X and Y output from the lock-in.

So the resonance at 24.805 kHz corresponds to the lower torsioanl mode, which is in good agreement with the ANSYS simulation results.

2.2.2-2 Noise Scan of the Oscillator

Doing a noise scan without an external driving signal, we can still get the Lorentzian curve as shown in Fig 2.14. From the noise scan, besides measuring the resonance frequency and quality factor as we do in the driven scan, we can detect another important parameter of the oscillator: the spring constant k [14].

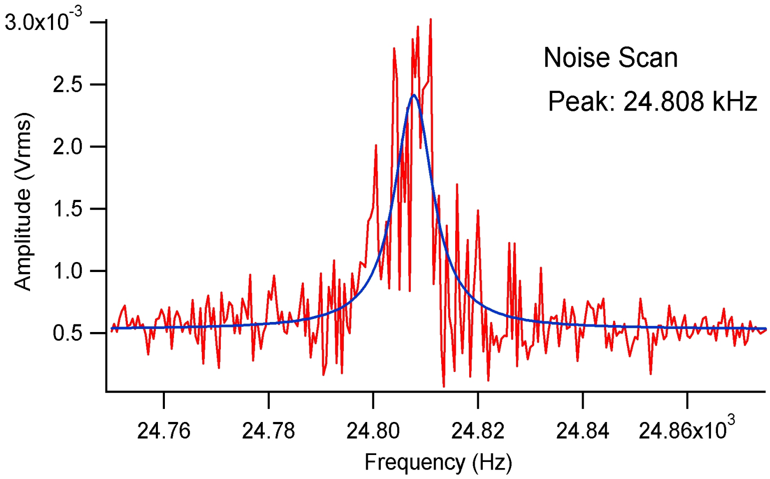

Fig. 2.14: Noise scan of the oscillator.

The spring constant measurement is based on the energy equipartition theorem:

$$\frac{1}{2}k\left\langle x^2\right\rangle = \frac{1}{2}k_B T \tag{2.21}$$

where k, k_B, and T are the spring constant of the oscillator, Boltzmann constant (1.38×10^{-23} $\mathrm{J\cdot K^{-1}}$) and the temperature, respectively. Once we have a spectrum of the oscillator from the noise scan, we can integrate the spectrum curve to figure out the area under the curve. The area is actually the average value of $\left\langle x^2 \right\rangle$. From the equation above, we can immediately calculate the spring constant. The $\left\langle x^2 \right\rangle$ can be written as:

$$\left\langle x^2 \right\rangle = \int_0^\infty |G(f)|^2 S_F df \tag{2.22}$$

, where $|G(f)|^2 = \dfrac{f_{res}^4 / k^4}{\left(f_{res}^2 - f^2\right)^2 + \dfrac{f_{res}^2 f^2}{Q^2}}$ and $S_F = \dfrac{4kk_B T}{2\pi f Q}$ are the transfer function and the noise spectral density of the oscillator. For real measurements, the digitization of the time series R output from the lock-in was carried out by a Nicolet Pro 32 transient digitizer, and the RMS value was calculated, and then it was squared followed by bandwidth division. Eventually the integral of the fitting curve can give the determination of spring constant. From the noise spectrum of the oscillator, we can also determine the minimum detectable force of the oscillator:

$$F_{\min} = \sqrt{\frac{4kk_B T \Delta f}{2\pi f_{res} Q}} \tag{2.23}$$

Actually this is the thermal noise due to the Brownian motion. So at certain temperature (T) and vacuum level (Q), the force signal we are going to detect must be larger than this thermal noise level, otherwise the signal cannot be distinguished from the noise background without signal averaging.

2.2.2-3 Fast Fourier transform

Beside the noise scan, the Fourier transform also enables us to determine the resonance frequencies and the spring constants of the oscillator.

The biggest sampling rate of the SR830 or SR844 lock-in amplifier is 512 Hz. When we take the time series data from the lock-in, we store them in the computer, and then we apply the Fast Fourier Transform (FFT) to transfer the time series data into the frequency domain. All this work is implemented by the Labview program. For the details of FFT program, please check Appendix B. Since the sampling rate is 512 Hz, the bandwidth in the frequency domain also should be 512 Hz. So we need to choose the correct time constant for the lock-in. Due to the Nyquist theorem, the sampling rate must be at least twice as big as the highest frequency component in the real signal to be sampled. So a 1 ms time constant, which corresponds to 250Hz equivalent noise bandwidth, is the biggest time constant we can choose. When the program is running, the time series data from the photodiode are collected in terms of the X and Y output by the lock-in and stored in the internal buffer of the lock-in with the capacity of 16384 data points. Filling this buffer will take 32 seconds if we choose 512 Hz sampling rate. Once the data acquisition is finished, the labview program will dump the raw data from the lock-in buffer and transfer them to the computer where the Labview program will do the FFT.

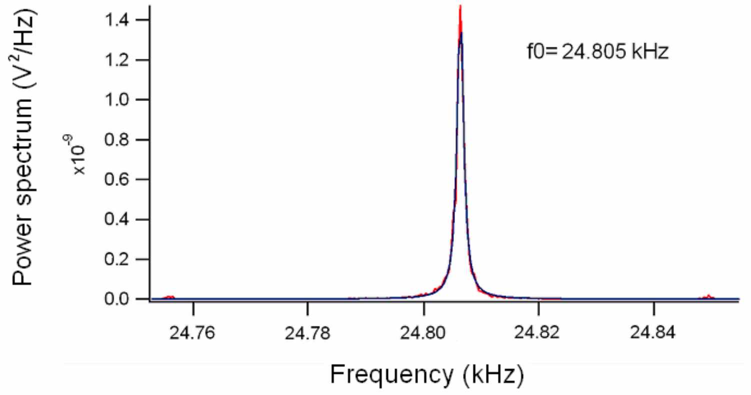

Fig. 2.15: Fast Fourier transform of the noise signal.

Assume we store N data points in the buffer, and the sampling rate is 512 Hz; thus, the frequency resolution is given by:

$$\Delta f = \frac{1}{N\Delta t} \tag{2.24}$$

where $\Delta t = \frac{1}{512\text{Hz}}$ is the time interval between time series data. The complex FFT will combine the X and Y outputs from the lock-in like z=x+iy, then the function FFT($|z|^2$) will generate the power spectrum of the time series data as shown in Fig 2.15. Using the slope at the fringe center, we can readily convert this voltage square to the distance square. And then we calculate the area under this Lorentzain curve. After that we can get the average value of $\langle x^2 \rangle$ as shown in Eq. 2.22. At this point, we can figure out the spring constant of the oscillator at the specific position (remember the spring constant is position dependent). The ANSYS software can also help us to estimate the spring constant, which provides a very good reference value to compare. Our FFT measurements turn out to be in good agreement with the simulation value. In Appendix B, the FFT Labview program is listed.

2.2.2-4 Decay curve from ring down experiment

Here we would like to introduce another reliable and effective method to measure the quality factor of the oscillator----extracting the Q value from a ring down experiment. In this experiment, first of all, we drive the oscillator at its resonance frequency with a certain driving amplitude. Then at some time, we suddenly stop the external driving force, and let the oscillator go by itself. Due to the damping force such as the air friction force, the vibration amplitude of the oscillator will be attenuated. This is an exponential decay and can be mathematically expressed as:

$$V(t) = V_0 \exp\left(-\frac{t}{\tau}\right) \tag{2.25}$$

where τ is the time constant. It is related to the Q value by: $Q = \tau\omega_{res}/2$. We ran the Labview program to take the decay data and store them in the internal buffer of the lock-in amplifier, and then we dumped the raw data and stored these time series data in the computer. Doing data curve fitting, we can easily extract the time constant of the decay curve. Thus Q value can be calculated by the equation: $Q = \tau\omega_{res}/2$. The following figure shows one typical decay curve we acquired.

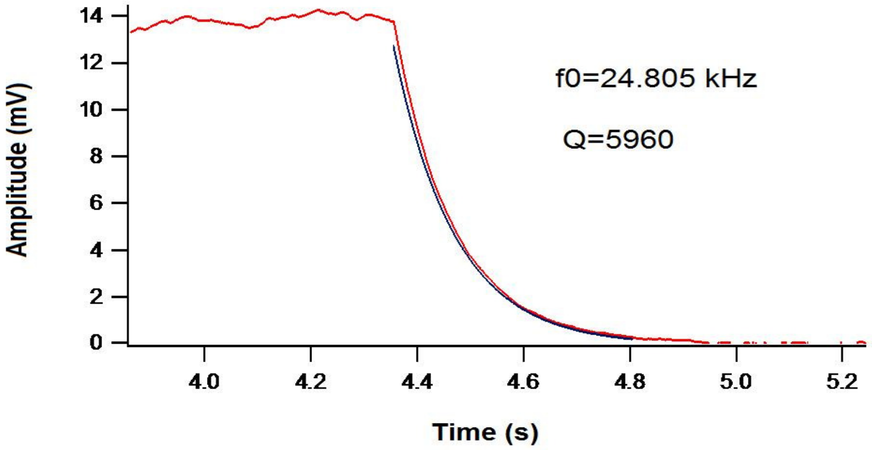

Fig. 2.16: Ring down decay curve from the ring down experiment.

At the beginning, we can see there is a flat plateau. After that, the voltage deceases exponentially due to damping. Doing the curve fitting on this exponential decay portion, we extracted a Q value of 5960, which is close to the Q value 6130 from the driven scan.

Chapter 3

Fabrication of Mechanical Micro-Oscillators

In this chapter, we are going to introduce a series of MEMS techniques for fabricating the mechanical micro-oscillators from normal silicon wafers and Silicon-on-Insulator (SOI) wafers and compare the oscillators from electron-beam lithography patterns with the ones made from conventional optical photolithography. All of these fabrication processes have been done mainly in two places. One is Microelectronics Research Center (MRC building 160) cleanroom in Pickle Research Center. The Microelectronics Research Center Facility (MRC) at The University of Texas at Austin (UT) is an open research laboratory funded by the National Science Foundation (NSF) through the National Nano-Technology Infrastructure Network (NNIN), which provides not only opportunities to perform research in novel materials of interest to the IC industry, but the training and experience about VLSI fabrication for graduating students. Another is the Center for Nano & Molecular Science & Technology (CNM) at UT campus. You can get the access to some necessary process facilities you need after training class offered by these two centers.

3.1 Introduction

Previously, the mechanical oscillators were fabricated from boron implanted silicon wafer [16], [17], [18]. The oscillator patterns were transferred by an optical photolithography. The fabrication process flow chart is outlined in Fig. 3.1. A 7500 $\overset{o}{A}$

of silicon dioxide layer was grown on a single crystal silicon (100) wafers. The first step in the processing is to make the oscillator pattern mask on the silicon wafer. A mask with the desired pattern is first drawn by some software. The pattern is deigned in such way that each 4-inch (100) wafer will result in 40 individual chips, each containing approximately 150 oscillators. Then the pattern will be transferred to a quartz glass mask with chromium on one side by optical photolithography. Once the mask is ready, it is then used to expose the silicon wafer with a positive photoresist (AZ5209) on it. The mask is aligned so that the base of the oscillators is parallel to the wafer flat. This is to allow for the best etching planes. The exposed wafers are then developed and the silicon dioxide layer on the exposed areas will be etched away using a reactive ion etch (RIE) with an oxygen and freon plasma.

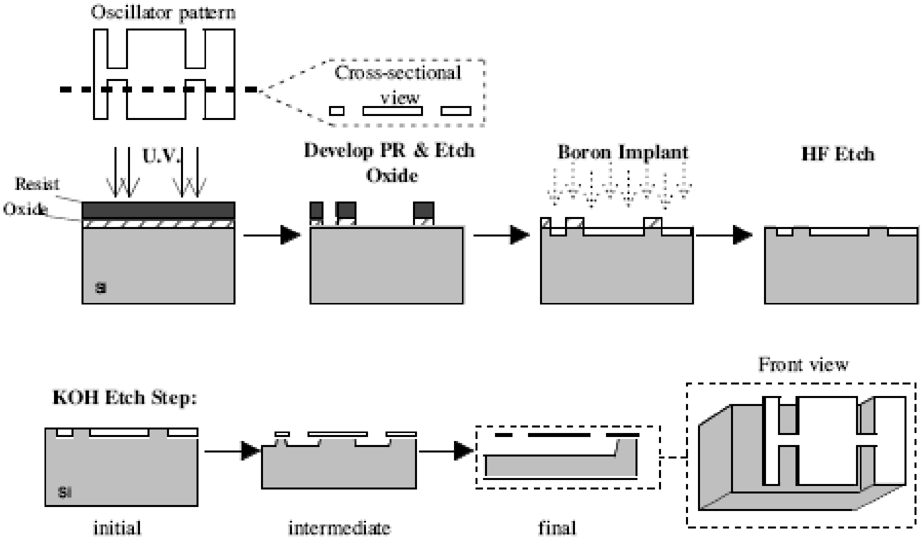

Fig. 3.1: Fabrication process of mechanical oscillators (M. D. Chabot and J. T. Markert, Proceedings of SPIE: Materials in Device Characterization in Micromachining II **3875**, 104 (1999)).

Once the oxide has been etched, the exposed areas of the wafer correspond to the location of the oscillators. Then Boron is implanted into these exposed areas at the energy of 134 keV and a dose on the order of 1×10^{16} ions/cm^2. The energy was chosen because it yields a peak implant of 400 nm. The initial 7500 $\overset{o}{A}$ thick silicon dioxide layer can guarantee to stop more than 99.99% of the boron for this energy. The Boron dose has been varied from 1.4×10^{16} ions/ cm^2 to 4.2×10^{16} ions/ cm^2 4.2. After implanting, an annealing at $1000\,^{o}C$ is performed to repair implant damage. This step broadens the steep Gaussian profile and therefore is a main factor in the final thickness of the oscillators. However, this broadening needs to be kept small so that the boron concentration in the area of the oscillators is kept large enough ($>7\times10^{19}$ ions. cm^{-2}) to stop the further potassium hydroxide (KOH) wet-etching. The higher dose with a short anneal time (1/2 – 3 hr) has been proven to produce the best oscillators, with thicknesses in the 100 – 400 nm target range. After the implant, the 4-inch wafer is sliced so that 40 individual chips are obtained. A buffered HF etch is done to remove the remaining silicon dioxide from each chip. The 1 cm^2 chip is now ready for the potassium hydroxide (KOH) etching. The most critical processing step is this final wet-etching. It is really time consuming, but you have to monitor the etching process all the time. This KOH wet etching is an anisotropic. This etching behavior will be discussed in detail later in this chapter. The heavily boron-doped silicon region serves as an etch-stop, since the etch rate of p++ silicon in KOH is much lower than that of undoped silicon. Varying the concentrations in the etch solution had a small effect on the quality of the oscillators after the etching, and it was determined that the optimal mixture consists of 125 g KOH, 300 ml distilled water, and 200 ml of ethanol. The temperature dependence was also investigated, and this was found to have a much greater effect. It was determined that decreasing the temperature provided much better differential etching. These optimal etch parameters result in several days of slow etching. For non-differential etching of pure silicon, it is common to etch at 80°C, giving an etch rate of approximately 1 μm/min. After a long period etching, the oscillators were completely etched away during this process. The SEM picture below shows the oscillators after etching

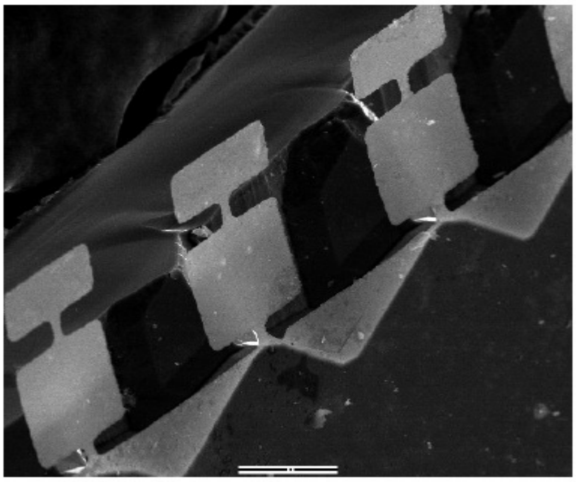

Fig. 3.2: Oscillators formed after KOH etching. (Chabot, 2001)

People in our group improved this boron-implanted wafer etching and already implemented a double-sided processing technique for the fabrication of our double-torsional oscillators [19, 20]. The main aim is to protect as much as possible the boron-implanted single-crystal regions that will become the oscillator structures; the addition of back-etch processing preserves the structures until the last, brief etch step. The process outline is shown in Fig. 3.3.

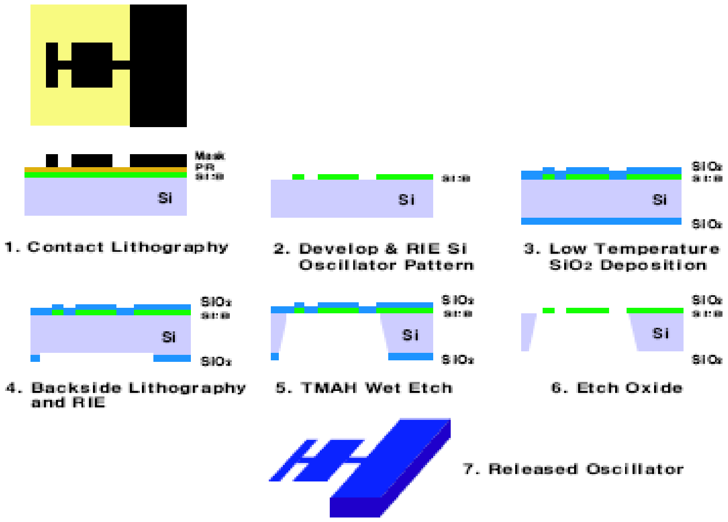

Fig. 3.3: Double-sided fabrication process of micro-oscillators (Lee 2006).

The fabrication still starts with a silicon (100) wafer, which is already implanted with boron on one side. After rapid thermal annealing (RTA) in order to rebuild the single-crystal structure, the oscillator pattern is transferred to a photoresist (PR) layer using optical lithography. The photoresist left after developing serves as a masking layer for the coming HBr reactive ion etch (RIE). The RIE serves to etch the oscillator patterns into the wafer by etching away the boron implanted silicon layer that has no front-side pattern. Then a thin (150 nm) layer of low temperature oxide (LTO) is deposited to both sides of the wafer. The backside is then patterned to provide etch windows for the oscillators. An infrared aligner is used to coordinate the backside mask with respect to the front side pattern. Silicon etchant will electively etch through the wafer from the back side only at these windows, so that the rest of the wafer can provide structural support during the etching. TMAH (tetramethyl ammonium hydroxide) solution is another ideal wet etching candidate as well as KOH (potassium hydroxide). When KOH is used,

Si_3N_4 was deposited instead of LTO. After the backside lithography, and when the back etch is almost complete, another reactive ion etch run is carried out to etch through the masking LTO (or Si_3N_4) layer. Then the oscillator wafer was put back in the etch solution for the complete release. The oscillators are rinsed thoroughly with distilled water before being dried. People have used volatile liquids such as acetone, isopropanol alcohol, or methanol in order to decrease the level of stiction due to the surface tension of the liquid and freeze-dried samples.

3.2 Improvement on fabrication process of micro-oscillators from Silicon-On-Insulator (SOI) wafers by using electron-beam lithography (EBL)

The much better material choice is Silicon-On-Insulator (SOI) wafer, since the top 300nm top silicon device layer can directly provide future mechanical micro-oscillators, so we do not have to get mechanical oscillators from Boron-implant layer on silicon wafer. Another advantage SOI wafer fabrication takes over boron implant wafer is that SOI can provide single crystal silicon which can make sure the oscillator would have much less defects introduced by ion doping than boron implant wafer so that better quality factor could be achieved, especially at low temperature. 8 inches SOI wafers are used in our case. The process flow is shown below:

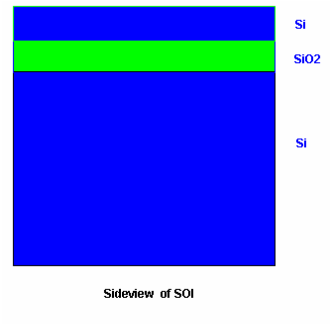

1. Prepare SOI Wafer

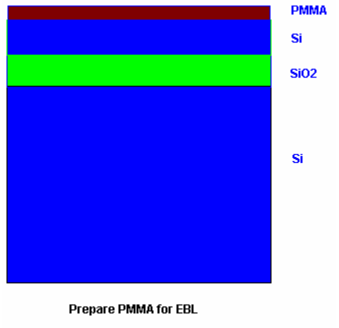

2. Spread PMMA for EBL

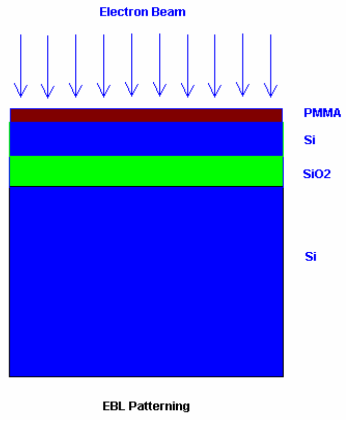

3. EBL Patterning

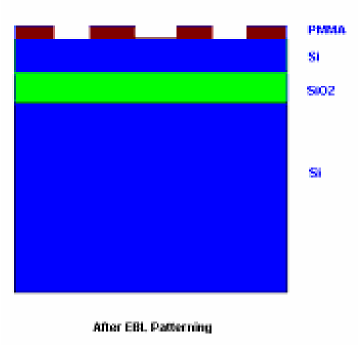

4. Patterns after EBL

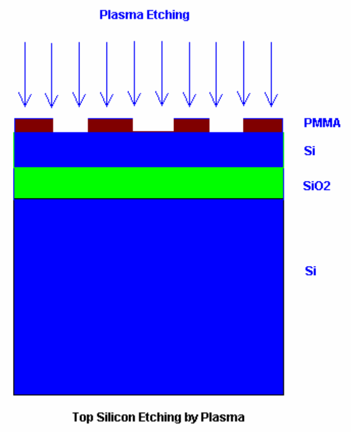

5. Silicon Etching by Plasma

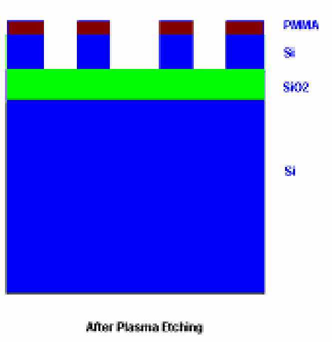

6. Patterns after Plasma Etching

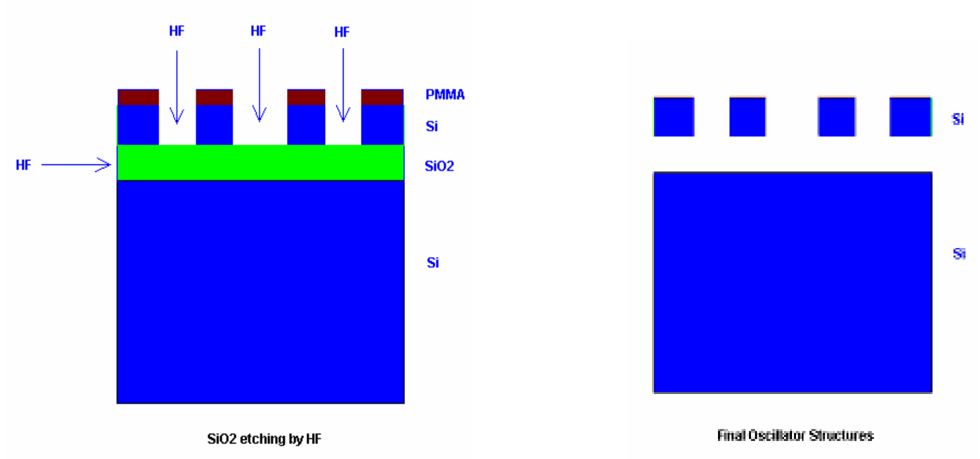

7. Etch the underneath SiO2 by HF 8. Final free standing Micro-Oscillators

Fig. 3.4: Process outline of micro-oscillators from SOI wafer.

Unfortunately, micro-oscillators fabricated from this process method can not be successfully characterized by laser interferometer. In other words, we can not tell the vibration of oscillator no matter how we drive it. Most likely, the tiny gap between the top oscillator structure and bottom silicon buffer layer significantly constrains the motion of the oscillator along the normal of wafer surface. For this reason, recently, we have improved the fabrication process of mechanical micro-oscillators. The revised process outline is shown in Fig 3.5:

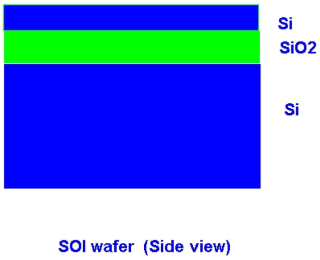

1. Prepare SOI wafer

2.Grow Silicon dioxide protective layers on both sides

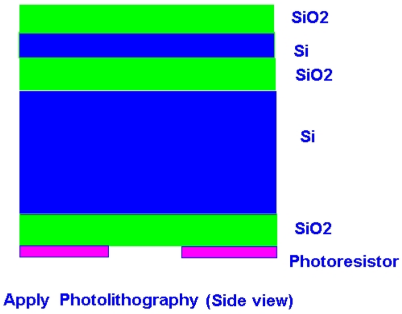

3. Pattern back side by photolithography

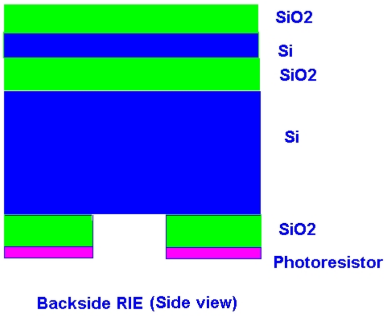

4. Reactive Ion Etch on back side

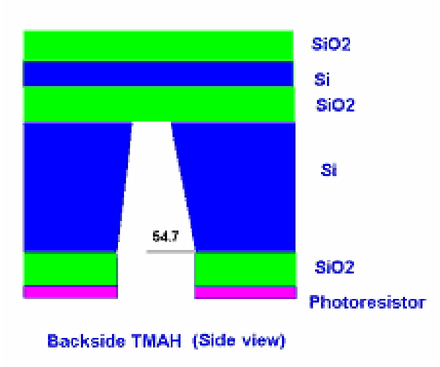

5. TMAH wet etching from back windows

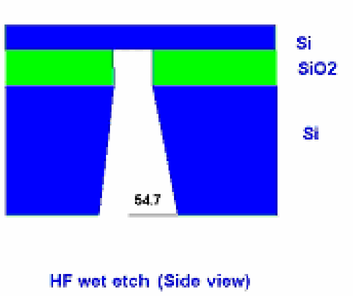

6. Silicon dioxide residual cleaning by HF

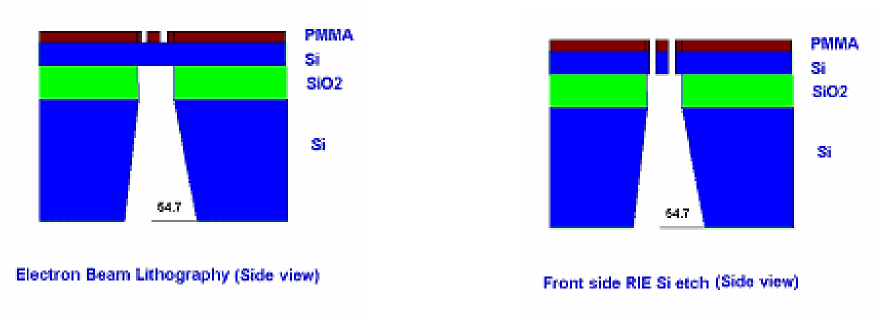

7. Pattern the front side on the front thin films 8. Front side silicon dry etching by RIE

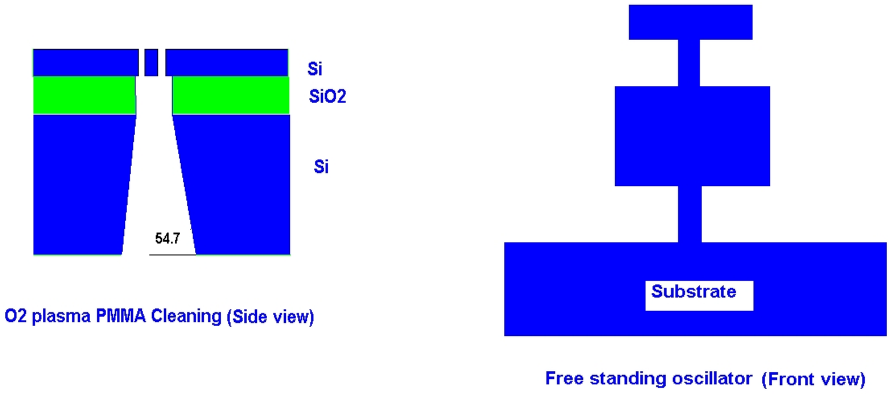

9. Oxygen plasma photoresist asher 10. Final mechanical micro-oscillator structures

Fig. 3.5: Improvement on double-side etch on SOI wafer.

Let's go through the whole fabrication process in detail in the following paragraphs. We prefer to cut the whole big wafer into small rectangular pieces (e.g. 4cm by 6cm).

3.2.1 Grow silicon dioxide protective mask layer by LPCVD LTO

Starting with SOI wafers, first we will grow the silicon dioxide (SiO_2) protective layers on both sides of SOI wafers for further chemical wet etching. To do this, we use

MRL LPCVD Low Temperature Oxide (400~500 °C) Furnace. Here you might have a question: why don't we use high temperature oxidization? The answer to that is Yes, you can. But you have to think about what will happen—for high temperature silicon oxidization, you will consume amount of top silicon material to grow silicon dioxide layer, and then in the further fabrication process, this amount of silicon will be sacrificed. Unless you want to get thinner silicon device layer, you can try it in this way---deliberately consume some of silicon to grow silicon dioxide, finally etch them away by HF. In our case, we do not want lose any silicon device material. So we choose LPCVD, in which silane (SiH_4) and oxygen can provide the reaction sources instead of consuming your precious device material [21, 22]. Here, let's quickly review the CVD and LPCVD techniques. CVD stands for Chemical vapor deposition, which is a chemical process used to produce high-purity, high-performance solid materials. The process is often used in the semiconductor industry to produce thin films. In a typical CVD process, the wafer (substrate) is exposed to one or more volatile precursors, which react and/or decompose on the substrate surface to produce the desired deposit. Frequently, volatile byproducts are also produced, which are removed by gas flow through the reaction chamber. Low-pressure CVD (LPCVD) processes at subatmospheric pressures. Reduced pressures tend to reduce unwanted gas-phase reactions and improve film uniformity across the wafer. Before doing this diffusion process, you need to apply the Piranha Clean (Hydrogen Peroxide + 98% Sulfuric Acid Mix) on the SOI wafers in order to remove some undesired organic materials attached to wafer surface otherwise some contamination could be introduced into LPCVD furnace during deposition process. When doing Piranha Clean, you MUST wear yellow Trionic® gloves, garment, and facial mask, since 98%

Sulfuric Acid will severely attack human skin. Be very careful about that! (Note: You are supposed to wear gloves in the Cleanroom all the time. Gloves available at the interior entrance to the cleanroom are to minimize particles in the cleanroom, but they do not give you protection against chemicals. A combination of the above-mentioned gloves under a yellow Trionic$^{®}$ chemical glove will provide the necessary protection. Trionic$^{®}$ gloves are available through out the cleanroom and in the new garment area. Pay attention, take the undopped gloves only, do not take the wrong one to avoid cross contamination) Check the operation instruction before you do it and strictly follow the clean instructions, do not skip any step. Once you finish Piranha Clean, dry the SOI wafer piece, and then it is time to put SOI wafer pieces in the correct carrier boat covered by clean wipes. Generally, in order to get better uniform silicon dioxide film over the whole SOI wafer, you are suggested to put more bare silicon wafer parallel to the piece you are going to process.

Fig. 3.6: LPCVD Low Temp Oxide – MRL (Pickle Research Center at UT).

The above picture (Fig. 3.6) shows some furnaces for deposition (e.g. Si_3N_4, SiO_2 deposition) and annealing process in MRC cleanroom located in Pickle. In this picture, the bottom one is the LPCVD for silicon dioxide deposit at low temperature (300~500 °C). Choose this furnace, and do not get the wrong one. Get access to MRL Low Temperature Oxide LPCVD by computer terminal, and load LTO530 recipe from menu and run the LTO program. Every program for MRL LTO LPCVD has been built in, so you do not need to change anything, just follow each step. At certain step, program will notice you to load sample. Hold the program, load SOI wafer pieces by transferring the carrier boat into the furnace, close the door, and pump the furnace. After that, the program will automatically execute further pumping, purge, temperature preparation, gas preparation and diffusion. The source gases include silane (SiH_4) and oxygen. Silane deposits between 300 and 500 °C. The corresponding reaction is:

$$SiH_4 + O_2 \rightarrow SiO_2 + 2O_2$$

As a result, silicon dioxide (SiO_2) layer will be grown on the both side of SOI wafer, while hydrogen gets away. At this point, one question you have to figure out is that how long this silicon dioxide deposit for SOI wafers should take, or in other words, how thick silicon dioxide protective layer is going to be grown on SOI wafers. Remember the silicon dioxide is used to protect the top device silicon layer from being etched by further chemical etching. Since the SOI wafer is 50%-90% thicker than previous boron implant wafer, the double-sided etching on SOI wafer will take much longer time as well. So in order to make the silicon device layer intact after etching, this silicon dioxide layer should be thick enough. You can check the deposit log to get reference about the deposit rate. However, the deposit rate is changing from time to time, so you could not only rely on the log records. After each LPCVD deposition, you should do thin film characterization by using the J.A. Woollam M2000 Ellipsometer, which can measure films with thickness ranging from 193 nm to 1000 nm. Ellipsometry is able to measure the refractive index and the thickness of semi-transparent thin films. The principle behind this metrology instrument is the fact that the reflection at a dielectric interface depends on the polarization of the light while the transmission of light through a transparent layer changes the phase of the incoming wave depending on the refractive index of the material. Applications include the accurate thickness measurement of thin films, the identification of materials and thin layers and the characterization of surfaces. The following figure roughly illustrates how an ellipsometer works.

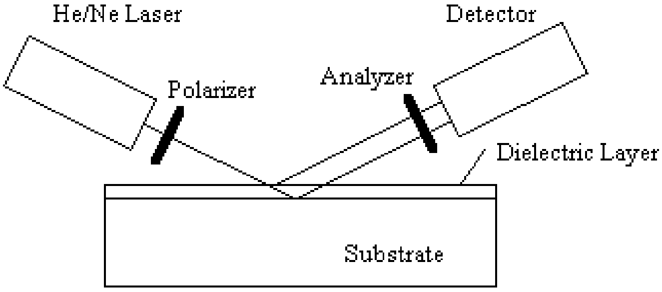

Fig. 3.7: Schematic drawing of an ellipsometer.

3.2.2 Back side window patterning by photolithography

From our experience, 2.5-3 hours diffusion should produce a silicon dioxide layer thick enough (around 1um thick) for our purpose. Once the silicon dioxide layer is ready, we use photolithography to pattern the array of small windows on the back side of an SOI wafer for future wet chemical etching. You can use appropriate software (e.g. Raith50) to edit mask designs meeting your requirement and save them to Graphic Data System file

(GDS II). Purchase the quartz masks from the National Nanotechnology Infrastructure Network (NNIN) related organizations (e.g Cornell Nanoscale Facility, Stanford Nanofabriaction Facility, and Microelectronics Research Center at UT austin etc) by submitting the GDS II file you have finished. When the mask is ready, you can do the photolithography to pattern the back side of wafer. I now describe that process.

Fig. 3.8: K. Suss mask aligner (Pickle Research Center at UT).

The figure above shows the photolithography instrument we are using to align the patterns on the back side of the wafer. The K. Suss mask aligner has the following features:

- Contact 1:1 lithography
- Exposure light wavelength 360 nm with an intensity of 7.5 mW/cm^2

- Mask holder sizes available, 4"×4", 5"×5", 7"×7".
- Wafer size is 6", 4", 3" and pieces.
- Maximum wafer thickness 4.3 mm
- Best resolution = 1 μm.

The photoresist we use is a positive resists: AZ 5209E. Since we will immediately apply reactive ion etching (RIE) (see the next section) on the back side of wafer after photolithography patterning, and the RIE etching rate for silicon dioxide is about 32 nm/min. However the actual etch rate would be smaller than this value, and the silicon dioxide layer we grow is normally much thicker than 1 μm just to guarantee it can do good protection in future chemical wet etch, as a result, the time for etching the thick silicon dioxide layer will be about 1 hour or even longer. Also you have to keep in mind that RIE attacks the photoresist at approximately the same rate as it does to silicon dioxide. Thus, you can not assume that a thin layer of photoresist would protect the area it covers throughout the RIE process. So the photoresist we spread has to be thick enough, otherwise some silicon dioxide area that you do not want to etch will be etched before the RIE etching gets finished. Fortunately a 300 RPM spin rate can give us an almost 1 um thick photoresist. By loading a photoresist-coated wafer piece sample, doing the alignment, making the exposure on the photoresist by the light beam from a Ultra Violet (UV) lamp for 30 seconds, and then doing the development, eventually we can get an array of small windows, each of which has the size of 4 mm by 6 mm. For convenience, recently we have fabricated silicon hard mask with open window array (shown in below).

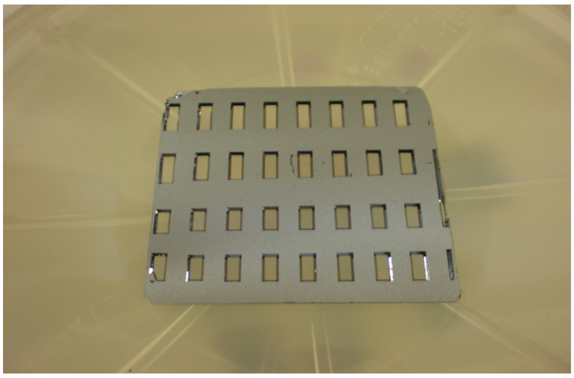

Fig. 3.9: Silicon hard mask for RIE.

With this hard mask, we do not need to apply photolithography, and do not have to be concerned about over-etching the photoresist during the RIE any more.

3.2.3 Completing the back side window array by Reactive Ion Etcher

The Reactive Ion Etch (RIE) is an etching technology used in microfabrication. It uses a chemically reactive plasma to remove material deposited on wafers or to remove some of the eafer itself. The plasma is generated under low pressure (vacuum) by an electromagnetic field. High-energy ions from the plasma attack the wafer surface and react with it. A typical (parallel plate) RIE system consists of a cylindrical vacuum chamber, with a wafer platter situated in the bottom portion of the chamber. The wafer platter, which is usually grounded, is electrically isolated from the rest of the chamber. Gas enters through small inlets in the top of the chamber, and exits to the vacuum pump system through the bottom. The types and amount of gas used vary depending upon the etch process. Gas pressure is typically maintained in a range between a few millitorr and a few hundred millitorr by adjusting gas flow rates. In this type of system, the plasma is generated with an RF powered magnetic field. Because of the large voltage difference, positive ions tend to drift toward the wafer platter, where they collide with the samples to be etched. The ions react chemically with the materials on the surface of the samples, but can also knock off (sputter) some material by transferring some of their kinetic energy. Due to the mostly vertical delivery of reactive ions, reactive ion etching can produce very anisotropic etch profiles, which contrast with the typically isotropic profiles of wet chemical etching. So by applying RIE, we can get very vertical trenches on the wafer. Etch conditions in an RIE system depend strongly on the many process parameters, such as pressure, gas flows, and RF power. You can change these parameters very flexibly.

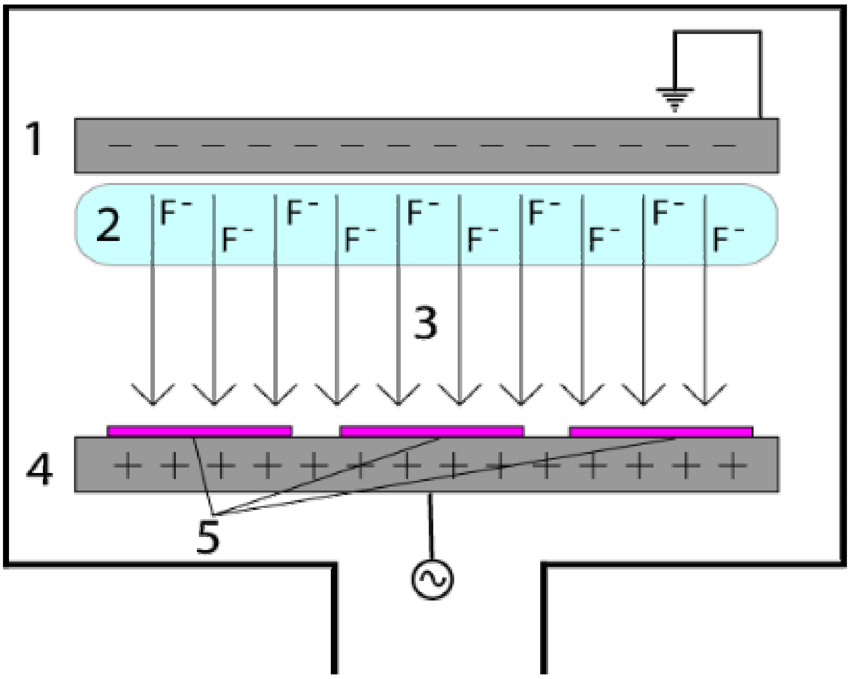

Fig. 3.10: A diagram of a common RIE setup. An RIE consists of two electrodes (1 and 4) that create an electric field (3) meant to accelerate ions (2) toward the surface of the samples (5).

Fig. 3.11: Reactive Ion Etcher (RIE) (Pickle Research Center at UT).

The features list as follows:

- Compatible Materials: Si (to etch with Cr mask, use the ORANGE RIE batchtop)
- Incompatible Materials: III-V / Hi K / Metal
- Features: up to 8" wafers
- Right chamber: CHF_3 (54 sccm), O_2 (20 sccm), H_2 (20 sccm), Ar (50 sccm)
- Left chamber: Cl_2 (20 sccm), HBr (100 sccm), O_2 (20 sccm), CF_4 (50 sccm), He (100 sccm)
- Turbo pump (10^{-5} Torr)
- Recipe: SiO_2: CHF_3 = 40 sccm, O_2 = 3 sccm, DC = 400 V (RF = 182 W), P = 40 mTorr

  Etch rate 32 nm/min

  Silicon: HBr = 25 sccm, Cl_2 = 4 sccm, DC = 250 V (RF = 128 W), Pressure = 40 mTorr, Etch rate 37 nm/min

The picture above shows the RIE facility we use in the cleanroom. As you can see this RIE system has two chambers. Each of them has different gas sources for different material etching. In our case, the target material is the silicon dioxide in the exposed window areas on the back side of wafer. The recipe we are choosing is CHF_3 = 40 sccm, O_2 = 3 sccm, DC = 400 V (RF = 182 W), P = 40 mTorr, the corresponding etch rate is given by 32 nm/min. Load this recipe, and run the program as we do for LPCVD. Program will automatically execute each step including filling reaction gases and turning on RF. Once the RF is on, you can see the soft glow from the view pot. Keep monitoring the plasma reaction all the time until it's done. In case the alarm is ringing, you need to hold the program or even stop it at all. Do not do the RIE by 2 or 3 hours continuously, which most likely will over-etch the silicon dioxide. You can try RIE in steps , say every 1 hour stop RIE and check the etch result.

3.2.4 Silicon back side etch through the window array by KOH and TMAH

Once we successfully get the patterned windows on the back side of an SOI wafer, we can do the most time consuming and most important process----wet chemical etching, to etch almost through the SOI wafer from the back until the etching is stopped by the buried silicon dioxide layer in the SOI wafer. In order to get a very uniform etching, and to keep the silicon dioxide protective layer on the front side as much as possible, the wet chemical etching process must be handled very carefully. Normally, as we did with the boron implant wafer, we still choose either KOH (potassium hydroxide) or TMAH (tetramethyl ammonium hydroxide). For the wet etchant, the hydroxide etches the silicon according to the reaction:

$$Si + 2\ OH^- + 2\ H_2O \rightarrow SiO_2(OH)_2^{2-} + 2H_{2(g)}$$

Of these two chemicals, TMAH has a slower etching rate for silicon dioxide than KOH, so it has better etching selectivity than KOH. Besides this, TMAH is an organic solution, so it doesn’t introduce metal ions to the wafer substrate during etching. This particular property makes TMAH much more suitable for IC fabrication in the semiconductor industry, and is also suitable for our case----we prefer less metal ion impurities in silicon. Unfortunately, TMAH costs much more than KOH. Note that silicon etching in both KOH and TMAH is anisotropic.

The following pictures show the basic orientation planes in our SOI wafers, and provide a feeling about how the etching goes with respect to the wafer surface.

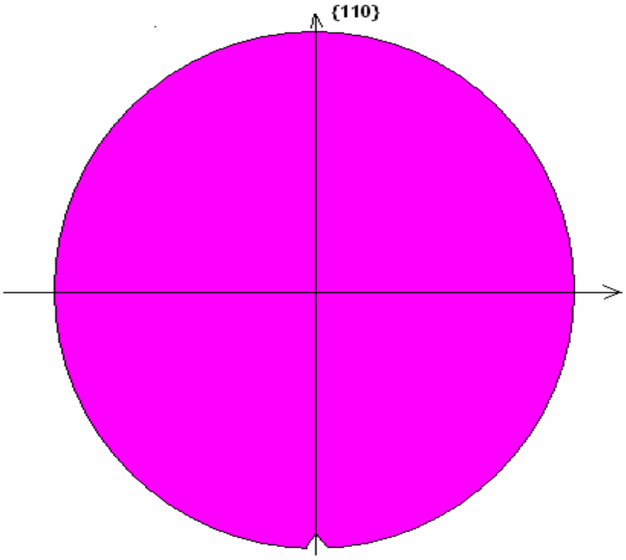

Fig. 3.12: {110} planes in an SOI wafer.

An SOI wafer is manufactured from a series processes such as deposit ion, bonding, chemical mechanical polishing, etc. Its cost is very high, so it is a very precious material. When you have an SOI wafer in hand, you can quickly tell the orientation of the {110} planes in it. There is one small notch on the edge. By using an appropriate wafer cutting tool to gently press this notch, the SOI wafer will be halved along the {110} direction. Before you cut the real SOI wafer, do some wafer cutting practice on some normal trash silicon wafers. Keep it in mind all the time---an SOI wafer is very, very expensive! Do NOT waste it! {111}-type planes have a high bond density, it turns out that the etching rate along {111} direction is much slower than other directions. The following geometric picture shows how the {111} planes orient in a cubic unit. By using a simple geometry, we can very easily extract the angle between the {111} planes and {100} planes to be $\arctan(\sqrt{2})$, which is equal to 54.7 °.

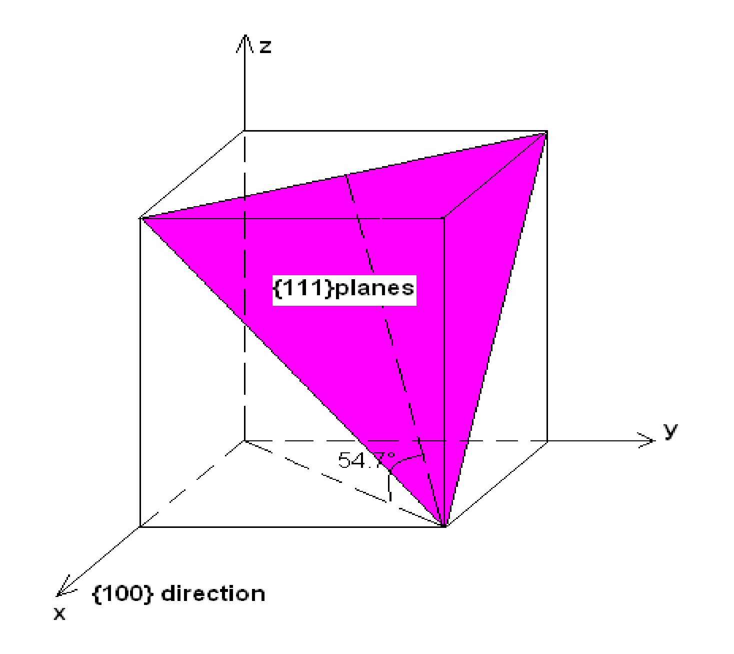

Fig. 3.13: {111} planes orientation with respect with {100} planes.

The etch-rate ratio for {110}, {100} and {111} planes of silicon in KOH is about 160:100:1 at 20 °C, decreasing to 50:30:1 at 100 °C [21, 22]. Also, this etch rate ratio perpendicular to different planes is a function of KOH concentration, where the higher the concentration, the smaller the ratio. So KOH etchant will attack silicon preferentially on the {100} planes, producing a characteristic anisotropic V-etch, with sidewalls that from a 54.7 degree angle with the surface.

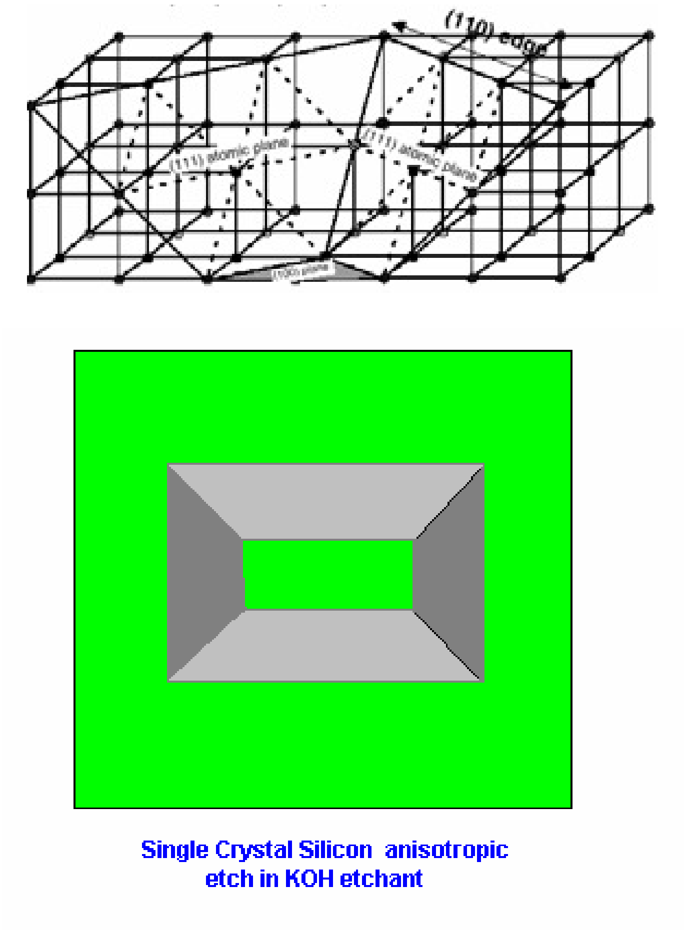

Fig. 3.14: Anisotropy etching behavior in KOH.

In order to get the higher etch-rate ratio, or in other words, to enhance the etching selectivity, we normally prefer low temperature (e.g. 60°C) and low chemical concentration (12~15% KOH solution). We typically prepare the solution in a 250 ml beaker, put the SOI wafer chips in one Teflon container, and then immerse the whole thing in the chemical solution. We then place the beaker on a hotplate, turn on the hotplate, and monitor the temperature with the thermomter immersed in the etchant. We do the same thing for the TMAH etchant.

As we mentioned, the etching rates for both of these chemicals strongly depend on temperature and chemical concentration [23-30]. The graphs [23] of the KOH and TAMH etching rates for different chemical concentrations and different temperatures are shown in Fig. 3.15.1~3.15.4, and they are very good references for further wet etching processes.

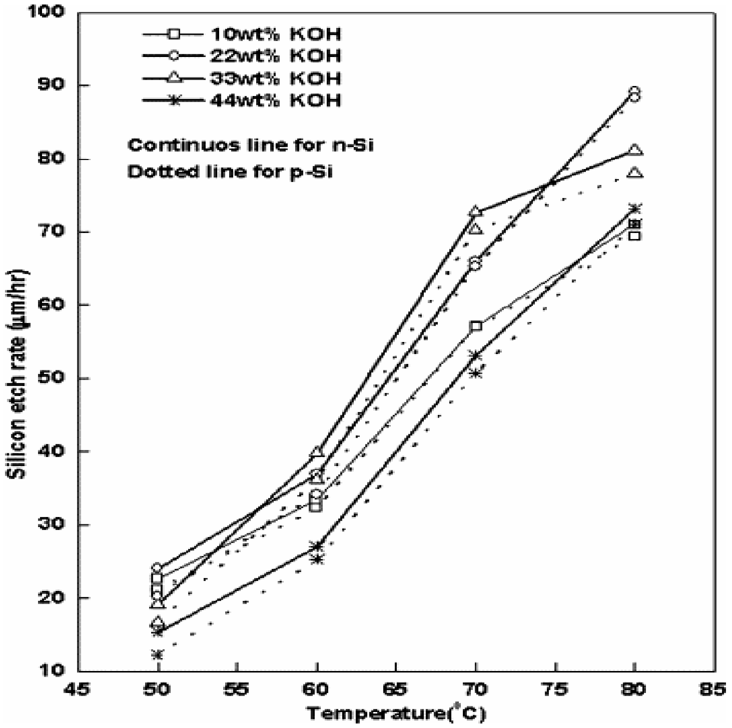

Fig. 3.15.1: Variation of the silicon etch rate with KOH concentration.

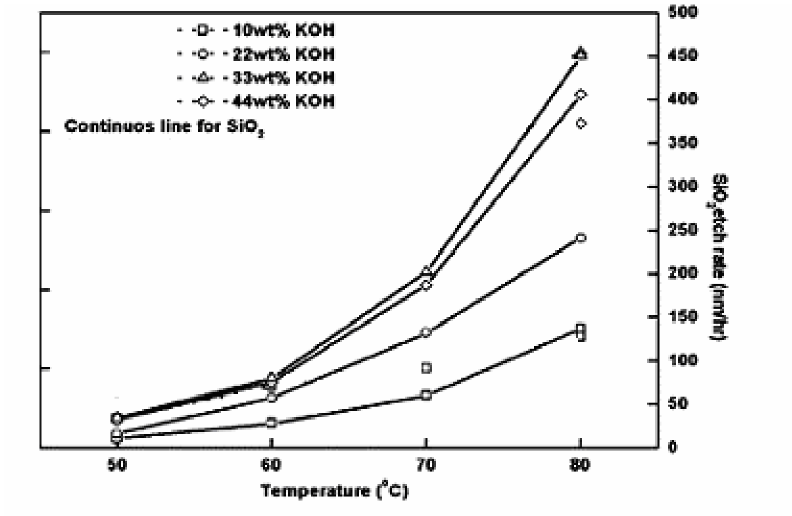

Fig. 3.15.2: Variation of the silicon dioxide etch rates with KOH concentration.

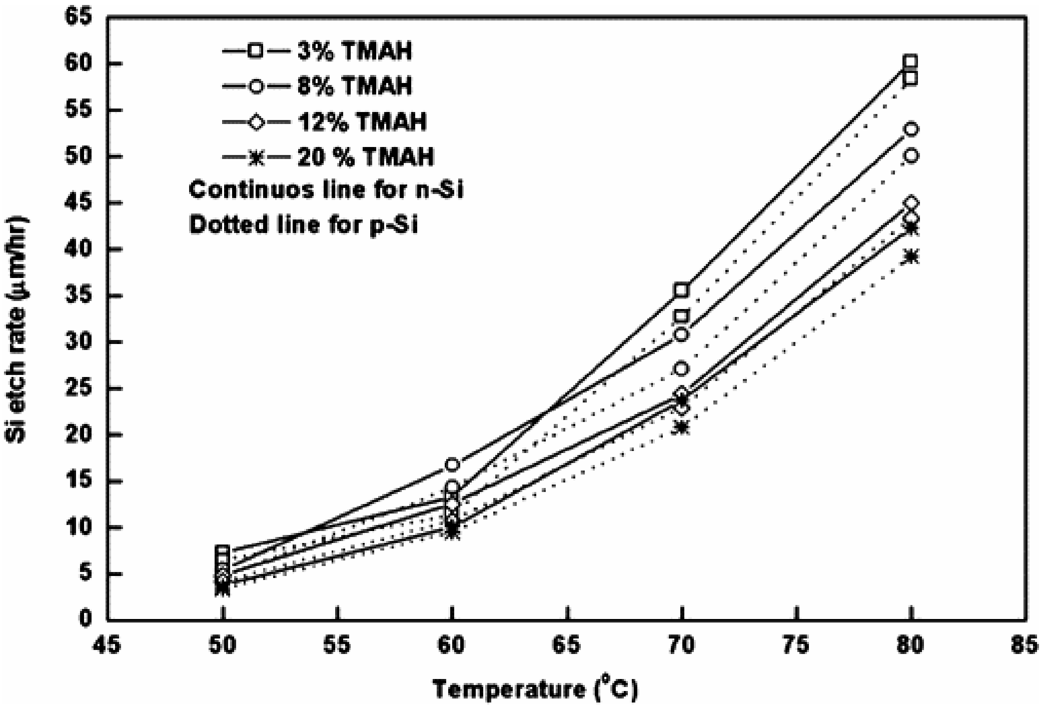

Fig 3.15.3: Variation of the silicon etching rates with TMAH concentration.

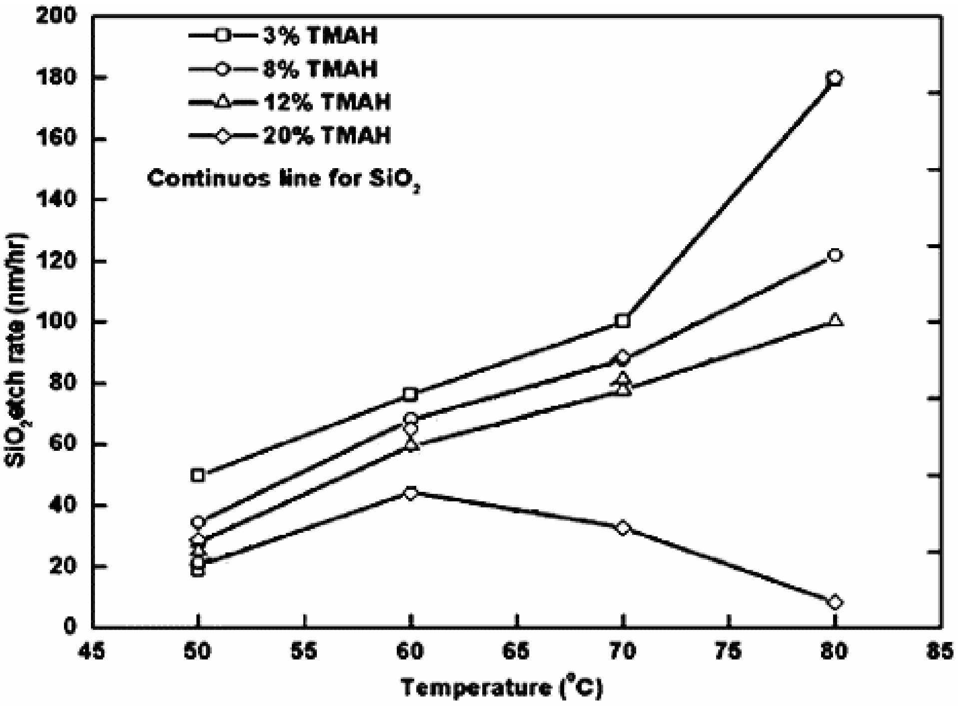

Fig 3.15.4: Variation of the silicon dioxide and aluminum etch rates with TMAH concentration.

To prepare the KOH solution, take into account that the KOH chemical pellets already contain 15% (weight percentage) water. Also you have to make the etchant solution as quickly as you can since the KOH pellets will absorb water vapor very quickly when they are exposed in the air. Failure to do this will result in an incorrect concentration. For the temperature setting, immerse a thermometer inside the solution, and check the reading from thomometer while you are dialing the heater until you get the temperature you want. For 60 °C, dialing our heater to number 3 or little bit above 3 can give you the right temperature. For better uniform temperature over the whole solution, you can place a small magnet stirrer on the bottom of the beaker, and turn on the spin.

The etching will take about 20~30 hours. You have to keep your eyes on this tedious wet chemical etching all the time. Never leave the etchant on the hotplate unattended, and DO NOT etch overnight without monitoring. Make sure not to over-etch the SOI wafer. Check the etch process every 30 minutes until you can see the greenish transparent film appear. At this point, the etching is almost done, so then take the SOI chips out of KOH or TMAH solution very very gently----the film is easy to break. Transfer these chips into volatile liquids such as acetone, isopropanol alcohol, or methanol in order to decrease the level of stiction due to the surface tension of the liquid.

3.2.5 Silicon dioxide etch by HF

Now we have to prepare the hydrofluoric acid (HF) etch for removing the remaining silicon dioxide from SOI wafer to get the pure single crystal silicon thin film. For concentrated HF, the reaction is [21]:

$$\mathrm{SiO_2 + 6HF \rightarrow H_2SiF_{6(aq)} + 2H_2O}$$

For buffered HF, the corresponding reaction is [21]:

$$\mathrm{SiO_2 + 4HF + 2NH_4F \rightarrow (NH_4)_2SiF_6 + 2H_2O}$$

We prefer buffered HF in our process. Pay attention, since hydrofluoric acid is the most dangerous chemical during our fabrication process. HF can attack human tissue, bone, and neural system very seriously. It’s absolutely fatal to the human body. Remember EVEN a SMALL HF exposure can be dangerous or life threatening. Possible first signs of an exposure:

a.) Redness of the skin

b.) Itching or slight burning of the skin

c.) Pain under the finger nails if exposed

d.) White to clear blistering of the exposed skin

For HF and other dangerous chemical handling, please refer Material Safety Data Sheets (MSDS) and the contents in the Appendix. NEVER EVER handle HF without training, NEVER EVER handle HF alone. When you are doing HF etching, you MUST wear garment, facial mask, and rubber gloves all the time. Especially for gloves, we suggest that you wear 2 latex gloves before taking HF rubber gloves in case the gloves are broken somewhere. During the process, take off the outer rubber gloves whenever you have to touch anything (e.g. faucet, beaker, timer, tweezers, etc.) except the HF container since we do not want to spread the HF contamination to other places. Once the hydrofluoric acid gets ready, we transfer the SOI chips with thin films from a volatile liquid to an HF-filled Teflon container with HF filled. Do this process very, very gently and smoothly. Turn on the timer, and monitor the etching time. 30~40minutes HF etching can completely remove the silicon dioxide residue from the SOI wafer. When we finish the HF etching, we take the SOI chips out of the HF solution and put them back into a volatile liquid. Since now it is only single crystal silicon thin film, it is very easy to break, thus you have to make sure the SOI chips are immersed in the liquid all the time during transferring. Use distilled water to clean the SOI chips several time. At the same time, trash the used HF solution into the HF waste bottle, and then use taped water to clean the Teflon container for several hours.

3.2.6 Using electron beam lithography to pattern the final oscillator structures on the thin silicon films

Now it is time to perform electron beam lithography (EBL) to pattern the micro-oscillator structures onto these thin films. E-beam lithography is the most important process facility we use for micro-oscillator fabrication, so before we go through it, let's review the background of e-beam lithography. EBL is a specialized technique for creating the extremely fine patterns required by the modern electronics industry for integrated circuits. This is possible due to the very small spot size of the electrons, whereas the resolution in optical lithography is limited by the wavelength of light used for exposure. The electron beam has wavelength so small that diffraction no longer defines the lithographic resolution. Beam widths were on the order of nanometers as of the year 2005. This primary advantage enables e-beam lithography to make features in the sub-micrometre regime. This form of lithography has found wide usage in mask-making (for masks used in photolithography), low-volume production of semiconductor components, and research & development. However e-beam lithography is not suitable for high-volume manufacturing because of its limited throughput. The electron beam must be scanned across the surface to be patterned, which means that pattern generation is serial. This makes for very slow pattern generation compared with a parallel technique like photolithography (the current standard) in which the entire surface is patterned at once (1 ×optical steppers only, 4 or 5× steppers take proportionally longer). As an example, to pattern a single wafer it would take an electron beam system approximately ten hours; compared to the few minutes it would take with photolithography. When doing the patterning, the electron beam is scanned across a sample surface covered with a resist film sensitive to electrons, thus depositing energy in the desired pattern on the resist film. Electron beam resists are the recording and transfer media for e-beam lithography. The usual resists are polymers dissolved in a liquid solvent. Liquid resist is dropped onto the substrate, which is then spun at 1000 to 6000 rpm (revolutions per minute) to form a coating. After baking out the casting solvent, electron exposure modifies the resist. Polymethyl methacrylate (PMMA) is the standard positive e-beam resist, Electron beam exposure breaks the polymer into fragments [33] (as shown in Fig. 3.15) that we dissolve in a 1:1 MIBK:IPA developer (MIBK is Methyl Isobutyl Ketone and IPA is Isopropyl Alcohol).

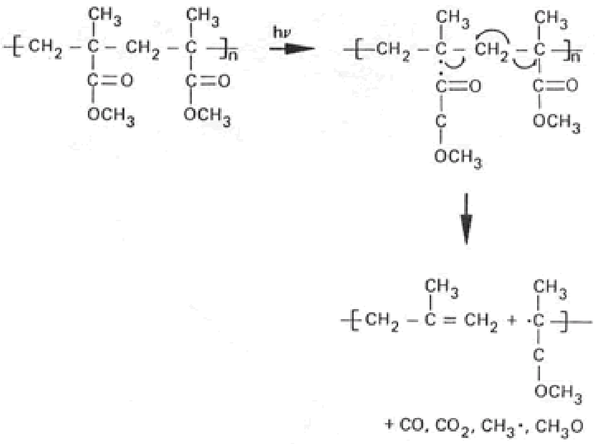

Fig. 3.16: Electron beam exposure breaking the polymer into fragments.

For different types of PMMA, you can refer to the following relation [32] between the PMMA thickness and spin rate to determine how thick the PMMA coating you are going to spread.

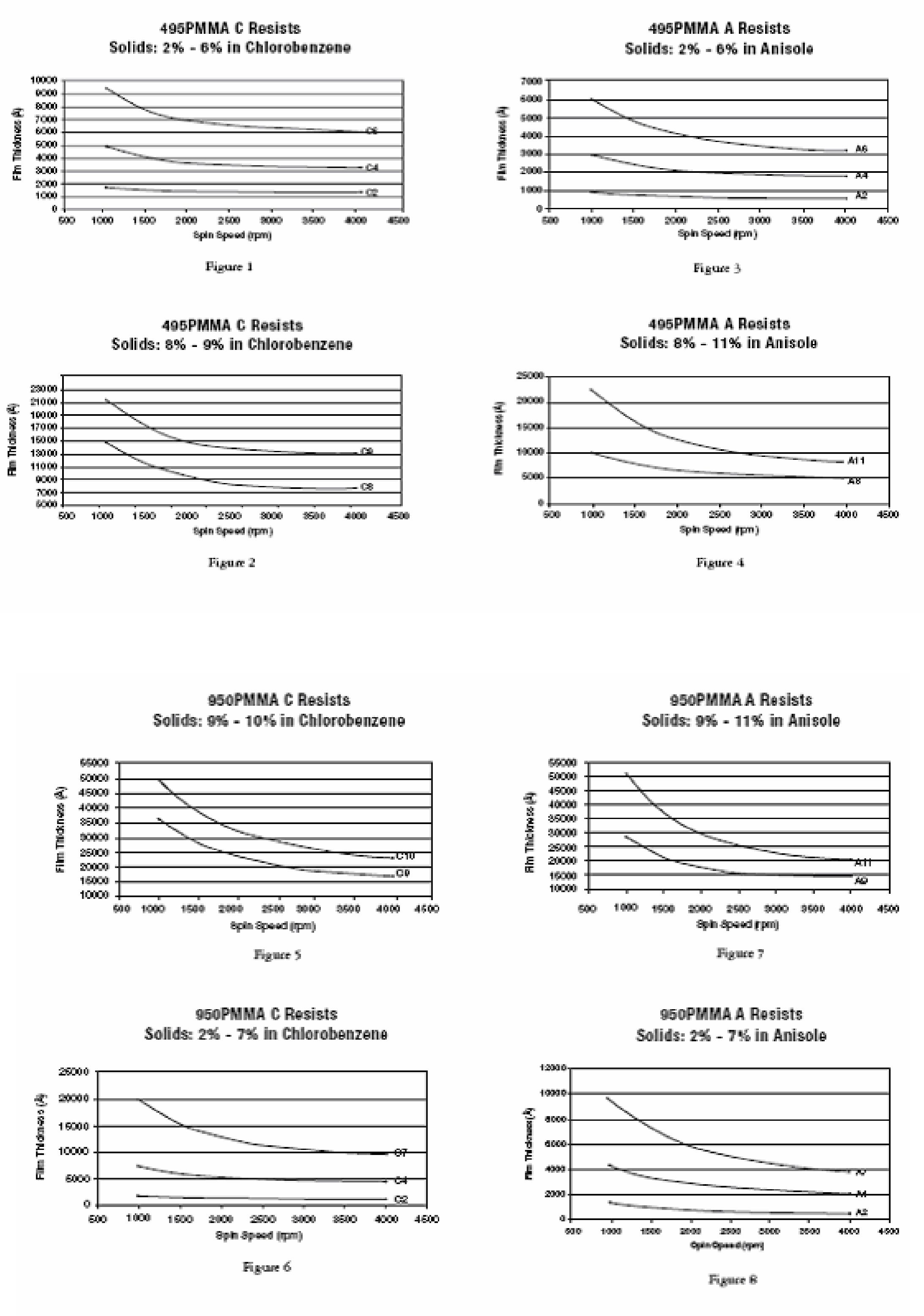

Fig. 3.17: PMMA thickness versus spin rate.

In our case, we spread the 4% PMMA with spin rate of 4000 rpm for 1 minute. Once the PMMA film gets ready, we use the Raith50 e-beam lithography system in the CNM cleanroom to transfer our oscillator pattens onto the silicon films covered by PMMA. The Raith50 is a universal lithography system which consists of a scan generator electronic hardware and PC-based operating software. It uses finely focused beam of electrons to define structures with dimensions of 20 nm. It is equipped with a laser interferometer stage which facilitates precise multilevel lithography with automatic mark recognition and patterns to be stitched together. The system has control in three major areas of Scanning Electron Microscopes (SEM): Beam Blanker control, Scan & Signal control, and Stage control. Editing and pattern design is made simple with a GDSII internal editor. Open this editor, put the coordinates for the any pattern you like to write. Once you finish that, save the file to GDSII format. This allows users to build a hierarchy of patterns on different levels and designs with any dose level. Then pattern data can be generated with the simple CAD program, or can be imported from a DXF (Auto CAD) file.

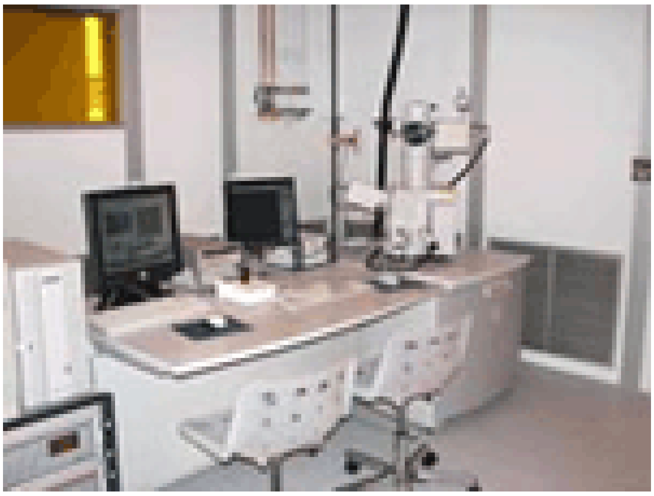

Fig. 3.18: Electron beam lithography (CNM, UT)

Electron-beam lithography operation is not very complicated. Follow the instruction manual step by step. At first vent the e-beam lithography chamber (this chamber is under vacuum all the time except sample loading/unloading), load the chip onto the stage, and use the metal clip on the stage to firmly hold the sample. Close the chamber, pump it to 4×10^{-4} Torr, and then turn on the high voltage. When system gets stable, open the Raith50 software which is specifically designed for e-beam lithography pattern edit. The following picture shows the basic interface of the Raith50.

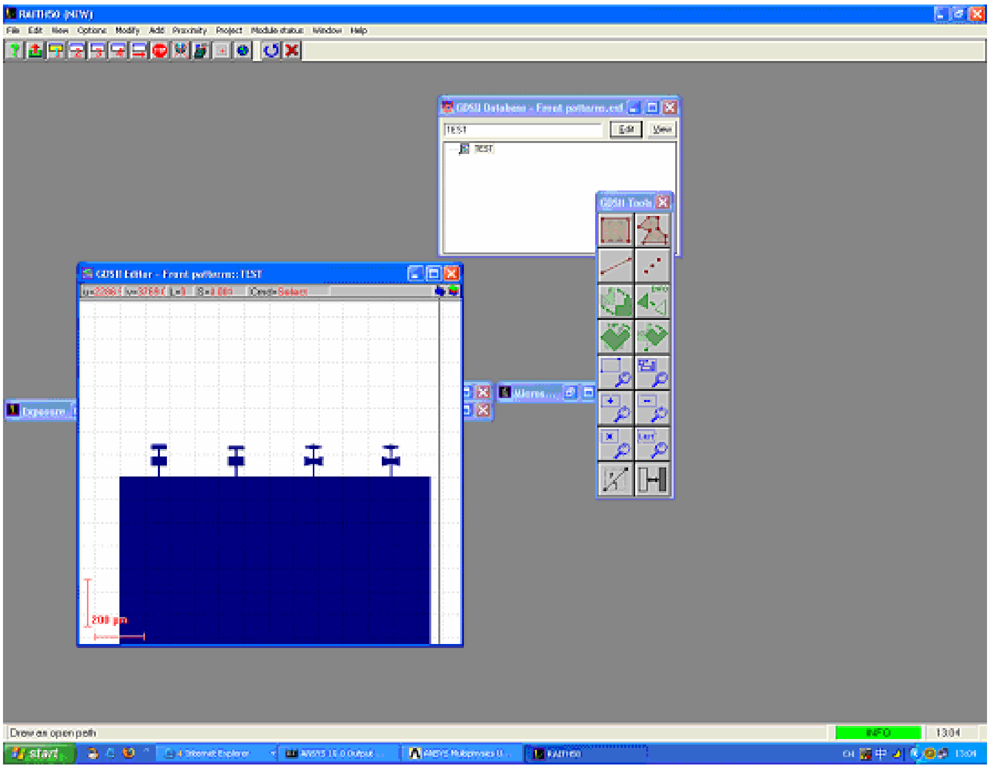

Fig. 3.19: Interface of Raith50 for e-beam lithography pattern edit.

Use the joystick on the control box to move the stage until you can see the profile of the sample chip. Do the alignment first, and then focus the sample until the magnification goes to 12,000. Set the position list of the patterns we are going to write, drag the GDSII files we already have into this position list, initialize the writing coordinate system (including origin define, angle tilting correction), and choose the correct current and electron dose for the exposure. Once everything is ready, start the SCAN command, and the Raith50 system will automatically move the stage so that the electron beam can hit the correct position on the sample, and then will do the lateral scan over one pattern after another.

For e-beam lithography performance details, please check the attached Appendix. Before you use every process tool and chemicals, get the appropriate training first. When this process is done, turn off the electron beam, vent the chamber, unload the SOI chip, and do the development by using 1:1 methyl isobutyl ketone (MIBK): isopropyl alcohol (IPA) developer. The positive PMMA resists develop away at exposed regions. At this point, we get the precise oscillator patterns for further fabrication.

3.2.7 Final RIE with PMMA Asher to get the free standing mechanical oscillator

Now we are approaching the final step of the whole fabrication process. Based on the e-beam lithography pattens, we immediately apply the silicon plasma etching. We still have to use the Reactive Ion Etcher, as we mentioned before. But this time we need to switch to the left chamber----silicon etch only [21, 22]. Load the recipe below:

Silicon: $HBr = 25$ sccm, $Cl_2 = 4$ sccm,

DC = 250 V (RF = 128 W),

Pressure = 40 mTorr

Etch rate = 37 nm/min

Remember, after the development, the undesired silicon areas have been exposed, while the rest of surface is still covered by PMMA. So the plasma can “cut” these undesired areas off from the silicon thin films, as a result, the micro-oscillators can be free standing from the silicon substrate. Actually, there is one more step we still need to do----clean the PMMA residue by using photoresist asher. This final process step will use the oxygen plasma at 150°C to get rid of the remaining PMMA attached on the double torsional mechanical oscillator-----It’s a very simple step, but it’s very important----failure to do it will result in serious deform caused by PMMA residue, so do not forget that! Okay, now the real micro-oscillators are coming out from the SOI chip. Following are some SEM pictures we have taken for the successfully made double torsional micro-oscillators:

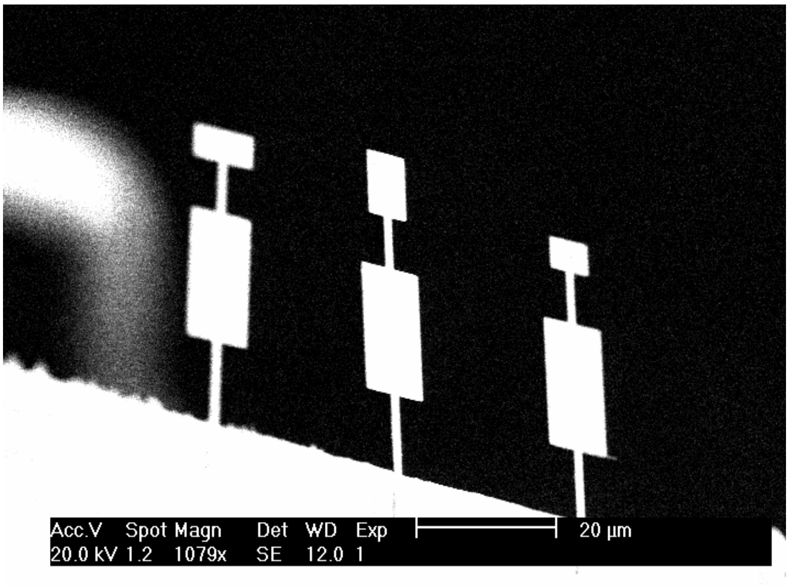

Fig. 3.20: An Scanning Electron Micrograph of 50 µm scale double torsional Oscillators.

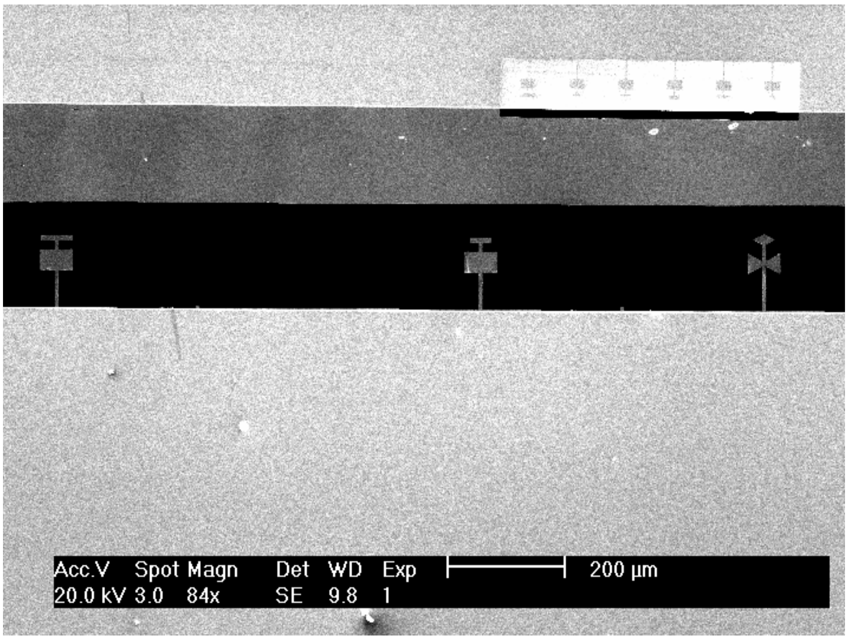

Fig. 3.21: An SEM graph of 150 µm scale double torsional oscillators.

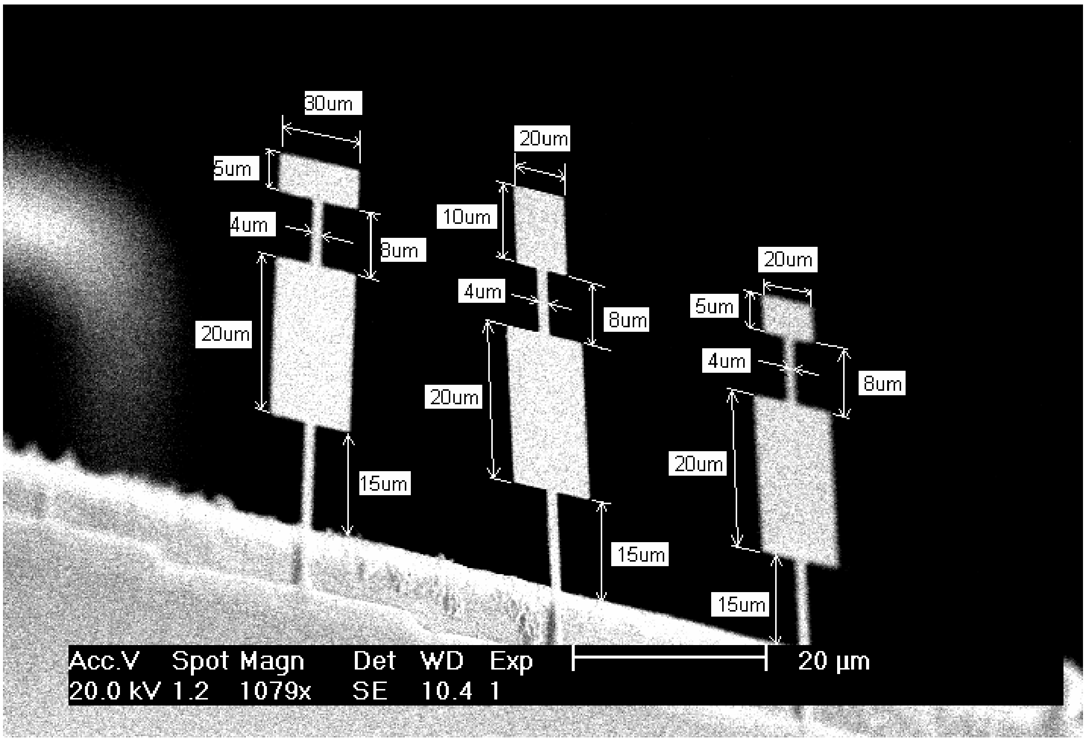

Fig. 3.22: An SEM graph of 50 µm scale double torsional oscillators with scale bars.

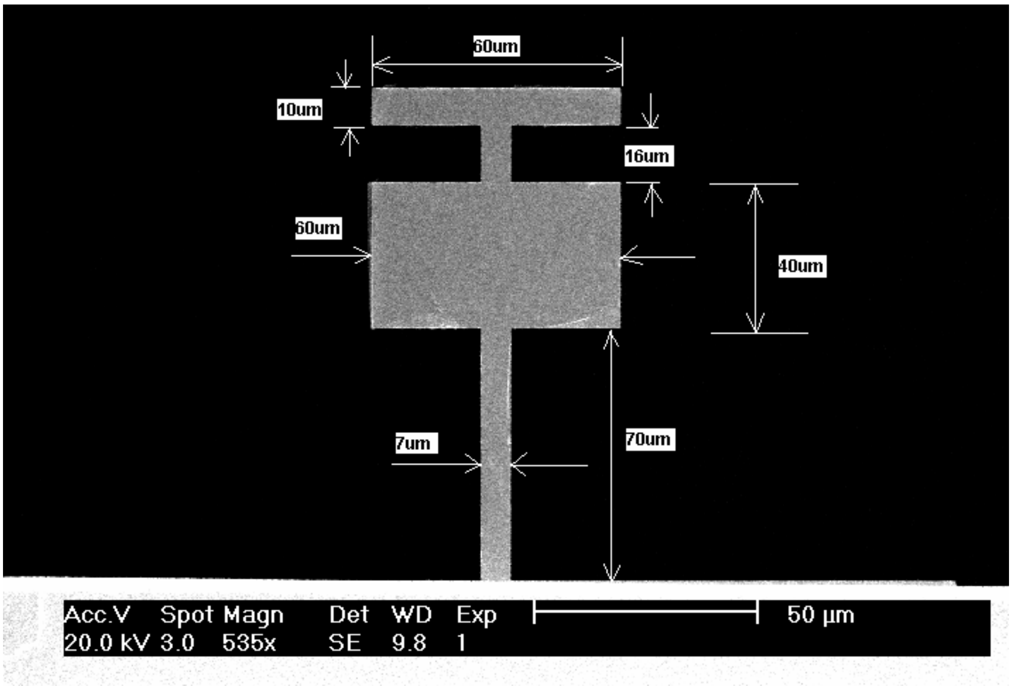

Fig. 3.23: An SEM graph of 150 µm scale double torsional oscillators with scale bars.

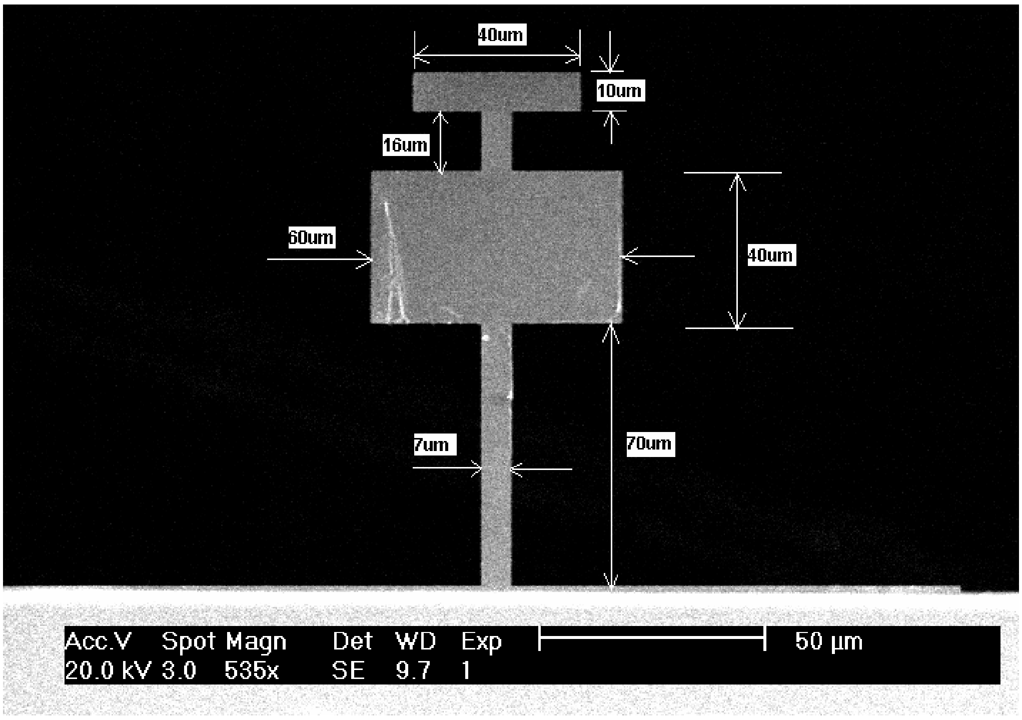

Fig. 3.24: An SEM graph of 150 µm scale double torsional oscillators with scale bars.

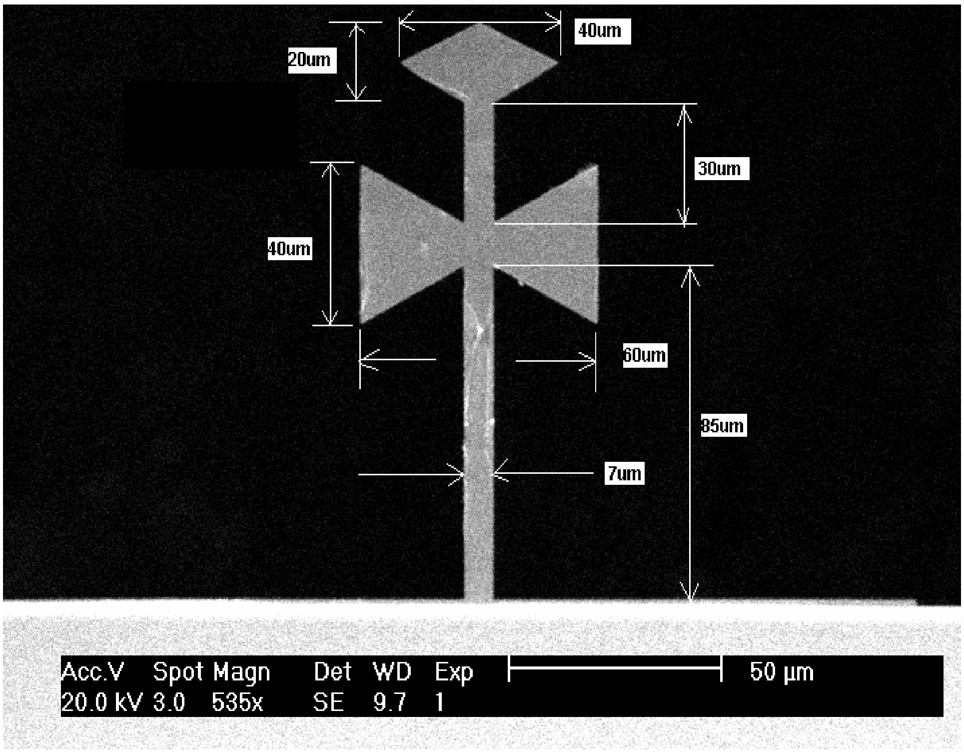

Fig. 3.25: An SEM picture of 150 µm scale double torsional oscillators with scale bars.

Compared with the SEM pictures for mechanical oscillators coming from the conventional optical lithography, the double torsional oscillators we fabricated by using electron-beam lithography really show better geometric symmetry and smaller physical sizes. These smaller geometric sizes can make these mechanical oscillators have much higher resonance frequencies and higher force sensitivities, which are suitable for future extremely small force detection experiments.

Chapter 4 Design and calibration of a 3-D nanopositioning system

As we mentioned in Chapter 2, a good laser interference signal depends on how well you align the fiber to the mechanical oscillator. Also, other experiments here, such as nuclear magnetic resonance force microscopy (NMRFM), require accurate and versatile capability for both the laser-oscillator and the oscillator-sample positioning. In this chapter, we are going to discuss several positioning control methods for alignment. We will especially focus on the piezoelectric motor design for alignment.

4.1 Introduction of 3-D positioning control systems alignment

Previously, our NMRFM probes used a pure mechanical positioning system to achieve laser interferometer alignment (shown in Fig. 4.1) [14, 16]. There are three coarse positioning stages that allow for alignment of the fiber to the oscillator. The fiber translator allows for the z-approach of the fiber stage towards the oscillator stage. The oscillator translator controls the y-motion of the oscillator stage. The stage the oscillator is mounted on also allows for x-motion. A gear system externally controls the alignment inside the probe.

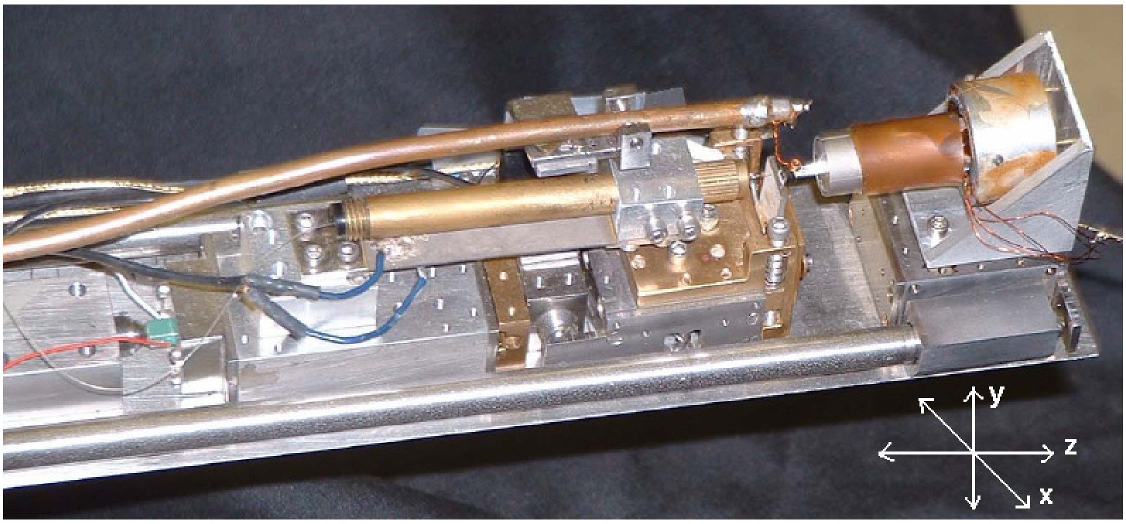

Fig. 4.1: Mechanical setup for NMRFM alignment positioning (Miller, 2003).

However, translation using gears is not very consistent due to the lack of uniformity of the gear teeth. This method a sliding stage which also introduces lateral wobble of tens of microns. Those factors make the alignment of the fiber with our small oscillators difficult. This mechanical inaccuracy can be significantly reduced by using a piezoelectric motor.

4.2 Attocube 3-D positioning system with the aid of a piezoelectric motor

Before introducing the piezoelectric motor, let's review what piezoelectricity is and how it works. Piezoelectricity is the ability of some materials (notably crystals and certain ceramics) to generate an electric potential in response to applied mechanical stress. This takes the form of a separation of electric charge across the crystal lattice. The growth of piezoelectric crystals and manufacture of piezoelectric devices is a well developed industry, yielding very uniform and consistent distortion for a given applied voltage. This phenomena is exploited in a controllable piezoelectric motor designed to move objects by utilizing friction forces developed between piezoelectric actuators and the object being moved.

Fig. 4.2: Commercial 3-D piezoelectric motor of the "Attocube" design [49].

By different arrangements of the piezoelectric actuators [43-50], the movement of the object can be linear, or rotational about a fixed axis. This, combined with the minute scale of the distortions, gives the piezoelectric motor the ability to take very fine steps — manufacturers claim precision to the nanometer scale. The high response rate and fast distortion of the crystals also allows the steps to be made at very high frequencies — upwards of 5 MHz. This gives a maximum linear speed of approximately 800 mm per second, or nearly 2.9 km/h. Piezoelectric devices are especially useful in applications requiring manipulation of small objects in environments where mechanical access is neither possible nor desired. Depending on their construction, these devices can also be used in harsh environmental conditions such as in ultra-high vacuums, at low temperatures, and in strong magnetic fields. There are particularly useful applications in Scanning Probe Microscopy (SPM) techniques, such as Scanning Tunneling Microscopy (STM), Magnetic Force Microscopy (MFM) or Atomic Force Microscopy (AFM), where the piezoelectric positioning system may be used to move the sample stage or the microscope probe tip. Commertial nanopositioning systems from Attocube use positiong stages made of titanium material (grade 2). Titanium is non magnetic material, so a positioning stage made of titanium can work in an environment with strong magnetic field, such as NMRFM experiments. Titanium also has a low thermal expansion coefficient. This property enables a titanium positioner to work at extremely low temperature. NMRFM experiments are often carried out at liquid helium temperature. So positioning stage made from titanium is a better than the stage made from oxygen free copper we used before. Oxygen free copper is also non-magnetic. But its thermal expansion coefficient is bigger than titanium. Especially at low temperature, copper stages sometime do not move properly. Recently, people [51] in our lab assembled titanium nanopositiong stages with graphite sliding rods, and succefully applied them to the He-3 probe for use in NMRFM. It is extremely beneficial to the fiber-oscillator-sample alignment in NMRFM. In this chapter, we still discuss the positiong stages made from oxygen free copper. Since the characterization measurements of our oscillators are done primarily in a small stainless steel vacuum chamber at room temperature without external magnetic field, copper stage is good enough for experiment requirements.

4.2.1 Stack piezo specifications

The following table shows the detailed specifications of piezo electric substance, such as the voltage range we could apply, the displacement under certain voltages, the resonance frequency, the operating temperature, the force load and the geometric dimensions.

	AE0203D04F	AE0203D08F	AE0505D08F	AE0505D16F and PZS001	AE0505D18
Maximum Drive Voltage	150 Volts	150 Volts	150 Volts	150 Volts	100 Volts
Displacement at Maximum Drive Voltage	4.6 ± 1.5 µm	9.1 ± 1.5 µm	9.1 ± 1.5 µm	17.4 ± 2.0 µm	15.0 ± 1.5 µm
Recommended Drive Voltage	100 Volts	100 Volts	100 Volts	100 Volts	Not Specified
Displacement at Recommended Drive Voltage	3.0 ± 1.5 µm	6.1 ± 1.5 µm	6.1 ± 1.5 µm	11.6 ± 2.0 µm	Not Specified
Resonant Frequency	261 kHz	138 kHz	138 kHz	69 kHz	138 kHz
Operating Temperature Range	-25 to +85 °C	-25 to +85 °C	-25 to +85 °C	-25 to +85 °C	-20 to +85 °C
Capacitance @ 1 kHz, 1V	0.09 µF ± 20%	0.18 µF ± 20%	0.75 µF ± 20%	1.40 µF ± 20%	1.60 µF ± 20%
Clamping Force	45 lb (200 N)	45 lb (200 N)	191 lb (850 N)	191 lb (850 N)	192 lb (853 N)
Maximum Preload	22.5 lb (100 N)	22.5 lb (100 N)	95.5lb (425 N)	95.5 lb (425 N)	22.5lb (100 N)
End Face Area	3.5 mm x 4.5 mm	3.5 mm x 4.5 mm	6.5 mm x 6.5 mm	6.5mm x 6.5mm	6.5 mm x 6.5 mm
Length	5mm	10mm	10mm	20mm	18mm

Table 4.1: Piezoelectric Specifications (Thorlabs.com)

In our positioning system, we used the AE0203D08F and AE0203D04F stack piezos to drive copper stages. Since the AE0203D04F has a smaller displacement 3.0 ± 1.5 µm at

100 V recommended volatge, we use it to do the fine approach of a fiber and an oscillator. The AE0203D08F piezo is used to control the lateral movement of a fiber and an oscillator. Fig. 4.3 on next page will show the detailed assembling.

4.2.2 Piezoelectric motor setup and movement principle

Below is the mechanical setup of our piezoelectric stages:

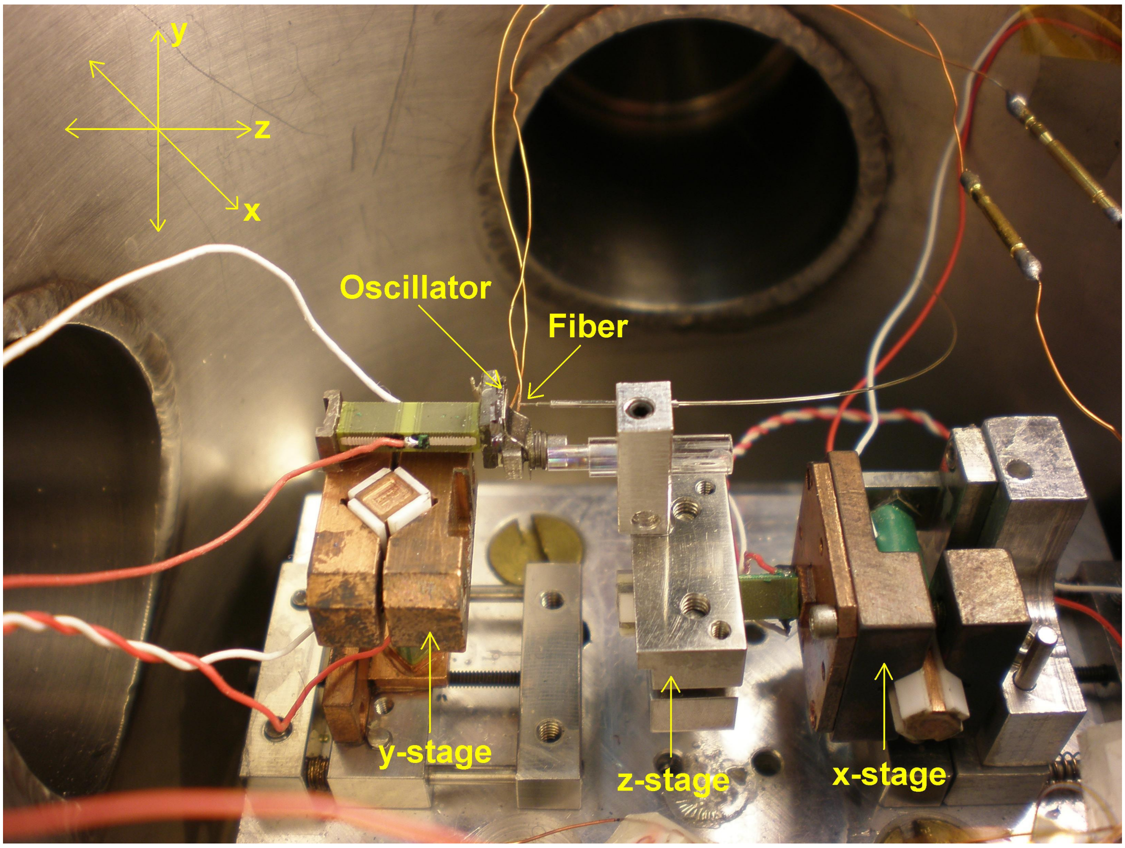

Fig. 4.3: 3-D piezoelectric positioner with fiber and oscillator mounted.

As you can see from this picture, from the left to the right, there is a y-stage, a z-stage and an x-stage, respectively. The y-stage controls the oscillator alignment along the y direction (see the axes in the upper left of the figure) with respect to the fiber. The z-stage directly controls the fiber distance, and allows it to approach or back away from the oscillator as necessary. The z-stage is also mounted on the x-stage which can move the z-stage along x direction. We let the fiber go through a thin stainless steel tube (500 μm inside diameter), which is glued onto the z-stage. So we control the fiber along both the x and z directions. Figure 4.4 and 4.5 below show the core part----the walker. It is composed of two copper clamping pieces (top and bottom), a copper sliding rod with four alumina sliding shoes (alumina provides a very smooth sliding surface) glued on it using epoxy, tightening screws, and springs inside the shoulder for flexible friction force adjustment. The copper stage can be sliding on the alumina rods over 7 or 8 millimeters without notable lateral wobble. (When a stage for fiber control is moving, the free end of a fiber is moving very parallel with the window on our oscillator chip)

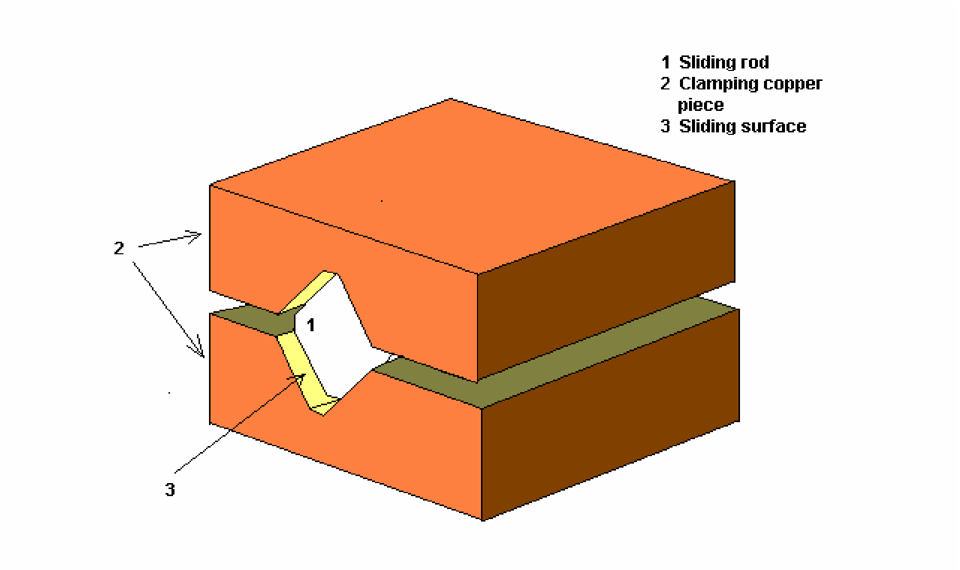

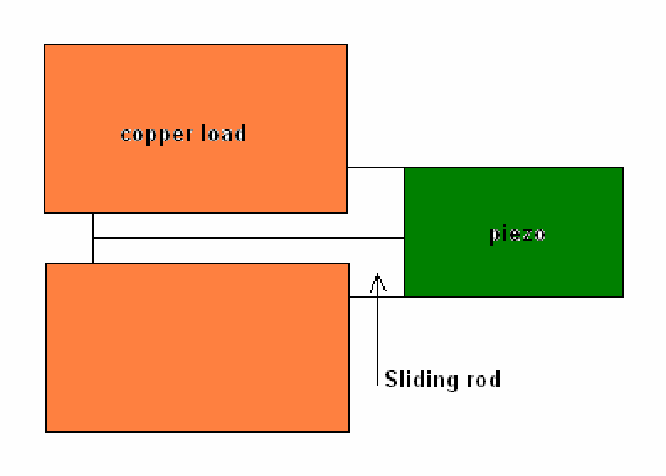

Fig. 4.4: Overview of a piezoelectric inertial walker.

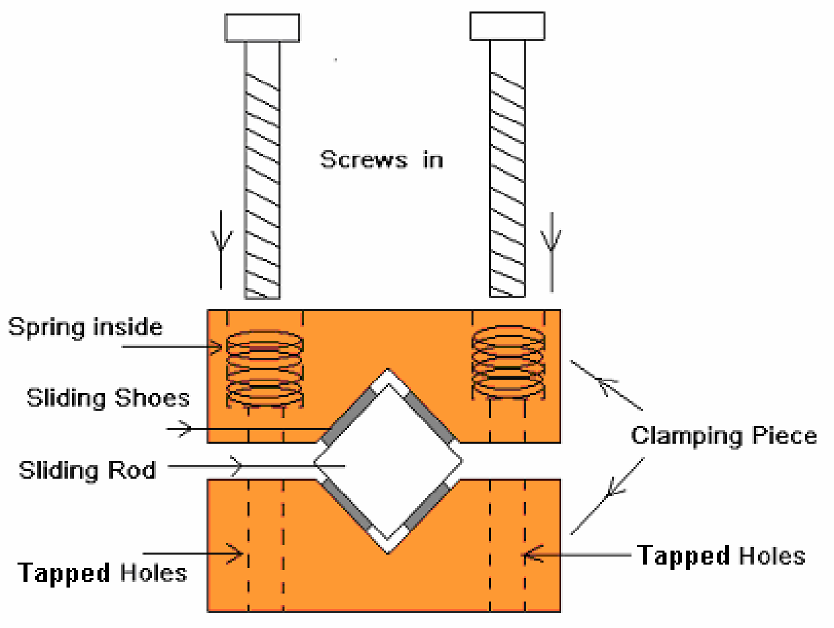

Fig. 4.5: Front view of piezoelectric inertial walker.

As shown in the figure, the top copper clamping piece has two clearance holes with shoulders for screws to fit in, while the bottom clamping piece has two tapped holes into which the screws can be fixed. The screws go through the top clamping piece via the clearance holes and the screw caps compress the springs inside. In turn, the spring compression can vary the top clamping pieces freedom for up-and-down movement. As a result, this freedom provides good flexibility for adjusting the friction force between the clamping pieces and sliding shoes. It can even permit the fitting of sliding rods with different cross-sectional areas.

Figure 4.6 demonstrates how the piezoelectric walker is driven by the sawtooth voltage waveform applied to the piezo elements.

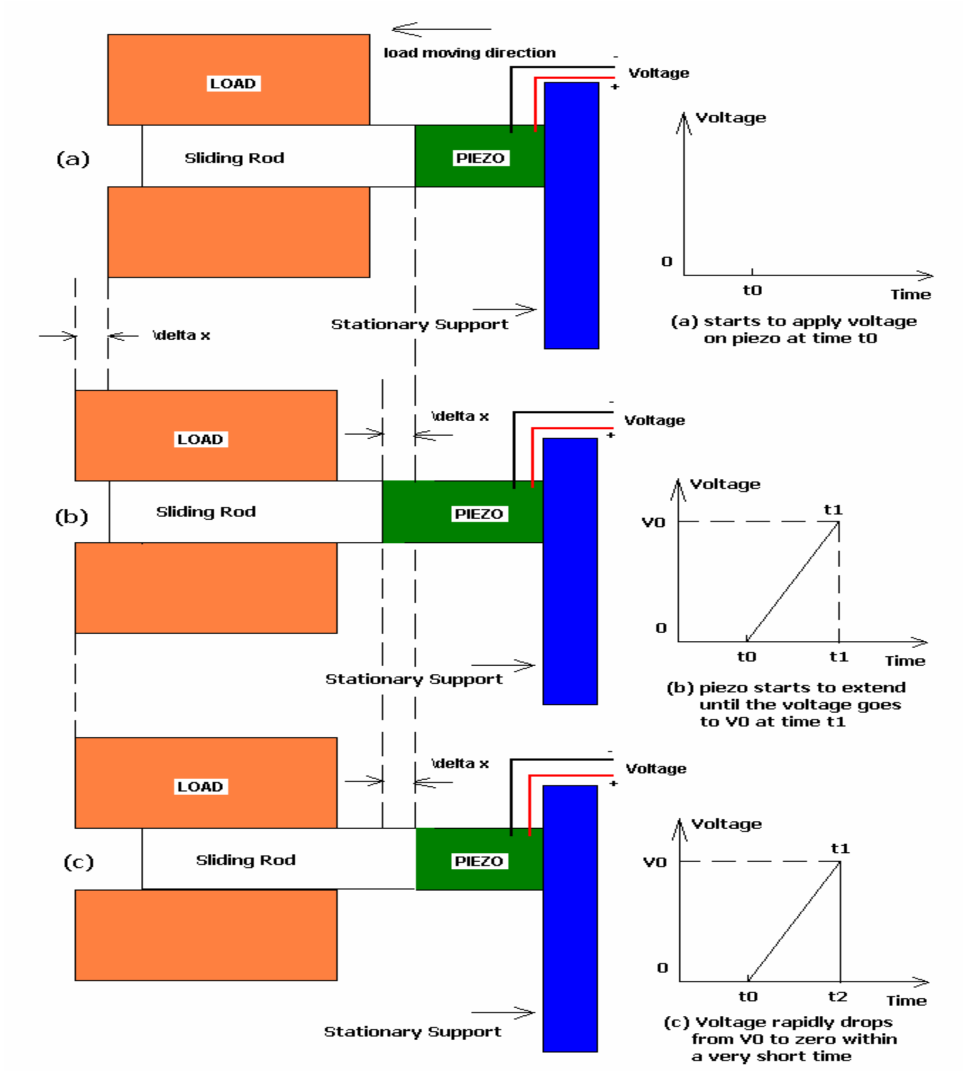

(a) starts to apply voltage on piezo at time t0

(b) piezo starts to extend until the voltage goes to V0 at time t1

(c) Voltage rapidly drops from V0 to zero within a very short time

Fig. 4.6: Application of a sawtooth voltage to the piezo to provides forward movement.

The operation principle behind this 3-D piezoelectric positioning system is as following: First, as shown in Fig. 4.4(a), a relatively slow voltage ramp is applied to the piezo element beginning at time t0 so that this piezo will slowly extend by a certain amount, typically about a micron. Since the sliding rod is glued to one end of the piezo (the other end of the piezo is firmly attached to a stationary support), when the piezo extends, the sliding rod will also be pushed forward. Due to the frictional force between the sliding rod and the clamping load pieces, the copper load will be pushed forward by the piezo also. The slow ramp-up to voltage is then followed by a rapid decrease of voltage from V0 to zero at time t1 (Fig. 4.4(b)). This sharp voltage decrease will make the piezo contract very quickly, so the sliding rod will be pulled back as well and retracted back to its original position while the copper piece, due to its inertia, will still keep its position instead of moving together with the sliding rod. As a result, the copper load piece moves with respective to sliding rod. In other words, by applying one single sawtooth voltage to the piezo, we can achieve the forward movement of the copper load with respect to the sliding rod.

One thing to note here is that these piezos, AE0203D04F and AE0203D08F, have two electrode leads, one is a white wire and the other is a red wire. The white wire should go to ground all the time, only the red wire can receive the external signal. Do not switch the electrode polarity, otherwise too negative of a voltage will most likely damage the piezo itself and reduce its life. Another concern is whenever you want to leave the piezo off duty, please make sure to connect the positive electrode lead (red) to ground. By doing this, you can let the accumulated charges on the piezo dissipate. This is particularly important if changing temperature, when thermal contraction can lead to large piezo voltage. Too much accumulated charge will affect the cycle behavior of the piezo.

We can achieve backward direction movement by changing the sawtooth waveform as in Fig. 4.7 (a-c).

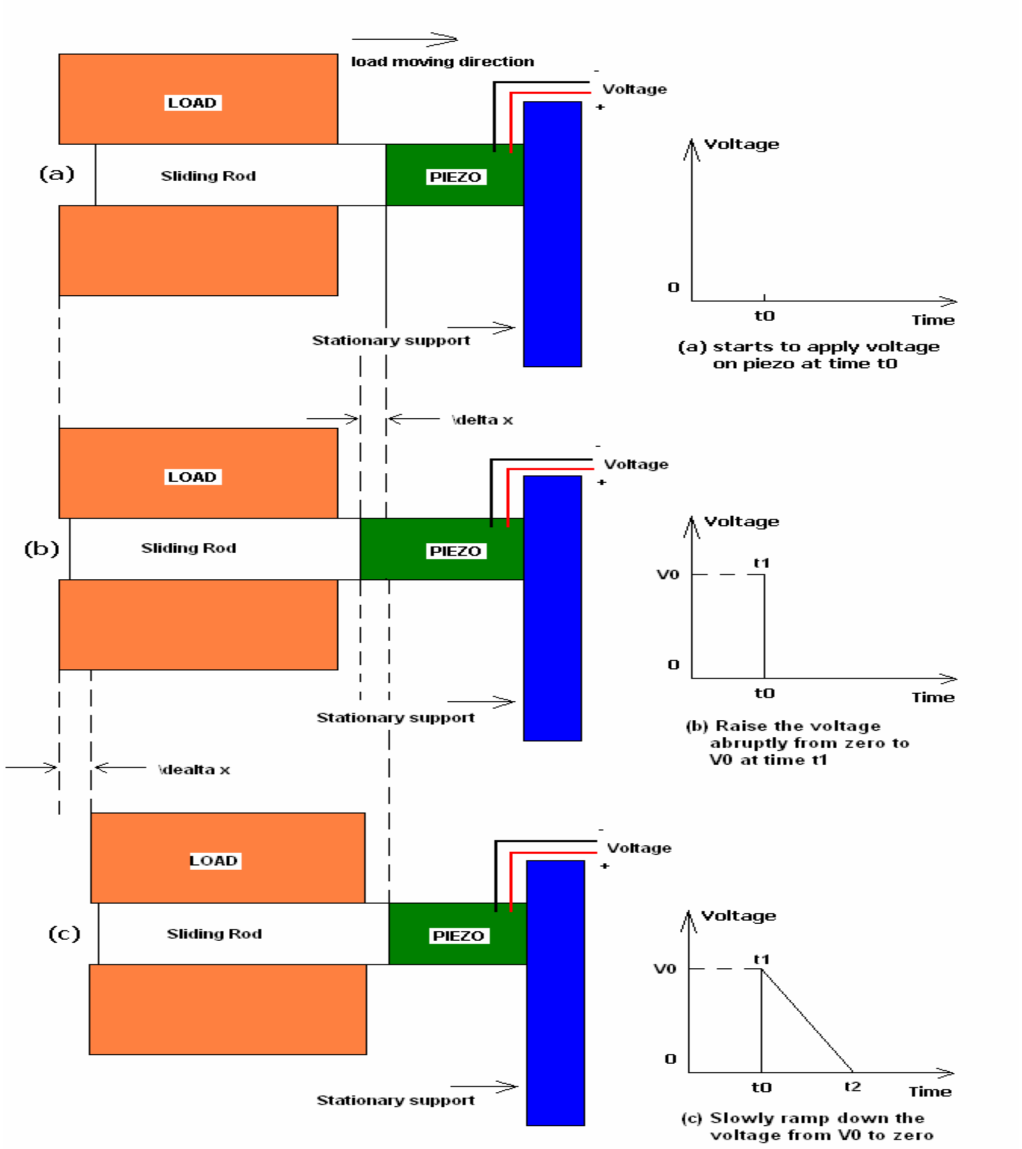

Fig. 4.7: Apply a sawtooth waveform on the piezo to drive the load to move backward.

In this case, at the very beginning, the piezo feels a sharp voltage increase from zero to V0, so it will extend very quickly, while the copper piece, due to its inertia, will still keep its initial position instead of moving together with the sliding rod. And then when the voltage drops relatively slowly back from V0 to zero, the piezo will contract, pull the sliding rod back, and the copper load will go back with sliding rod due to the frictional force between the copper load and sliding surface. Compared with its original position, the copper load moves closer to the piezo. So by reversing the slope polarity of the sawtooth, we can very easily change the direction of motion of the copper load as we want. If we want to move this copper load continuously, we continuously apply the sawtooth waveform to the piezo. Motion over several millimeter or more is possible.

4.2.3 Sawtooth function generation

When the 3-D piezoelectric motor stages are ready, the next thing we need to do is to prepare a sawtooth waveform generator. There are three options we can choose for the sawtooth waveform. The first choice is to use a commercial function generator such as Stanford Research System DS 345, Hewllet Pack HP 3325B, etc. However, the sawtooth output from the commercial one is always continuous, thus we can not take a single sawtooth when we want do the precise alignment. Beside that, the output has only peak to peak amplitude of 20 volts which is not high enough to effectively drive the piezo, especially at low temperature. The second option is to use a Labview programmed DAQ (NI-PCI 6711 from National Instruments) data acquisition card to generate any waveform one may want. The third option is to build a sawtooth waveform generator by programming mico-controller. We will discuss the last two options in section 4.2.3-1 and 4.2.3-2, respectively.

4.2.3-1 Sawtooth waveform generated from Data Acquisition Card (DAQ)

For this option, we wrote a very flexible sawtooth waveform generation program using the Labview software, and used the Labview program to “talk” to the DAQ card and let it generate the appropriate sawtooth waveforms we need for any case. Before using the DAQ, you have to correctly install it onto the PCI bus slot in your computer motherboard and install the driver program. For details about DAQ communication and the associated Labview program we are using, please see Appendix B. Once we have the sawtooth waveform from the DAQ, we have to amplify the signal to some certain level before we feed it into the piezo elements. Just keep in mind that piezo element should be modeled as a capacitance. For the piezoelectric walker, the critical point is the sharp voltage change (either increase or decrease). So in order to apply a very sharp voltage ramp on it without distortion, we need to make sure that the current going through the piezo is large enough. The reason for this is very simple, the current through a capacitor can be written as the voltage change rate:

$$I = C\frac{dV}{dt}$$

This formula tells us that if the current is big enough, then the slope of the voltage change is also very big so as to make the piezo extend or contract quickly enough to leave the copper load still.

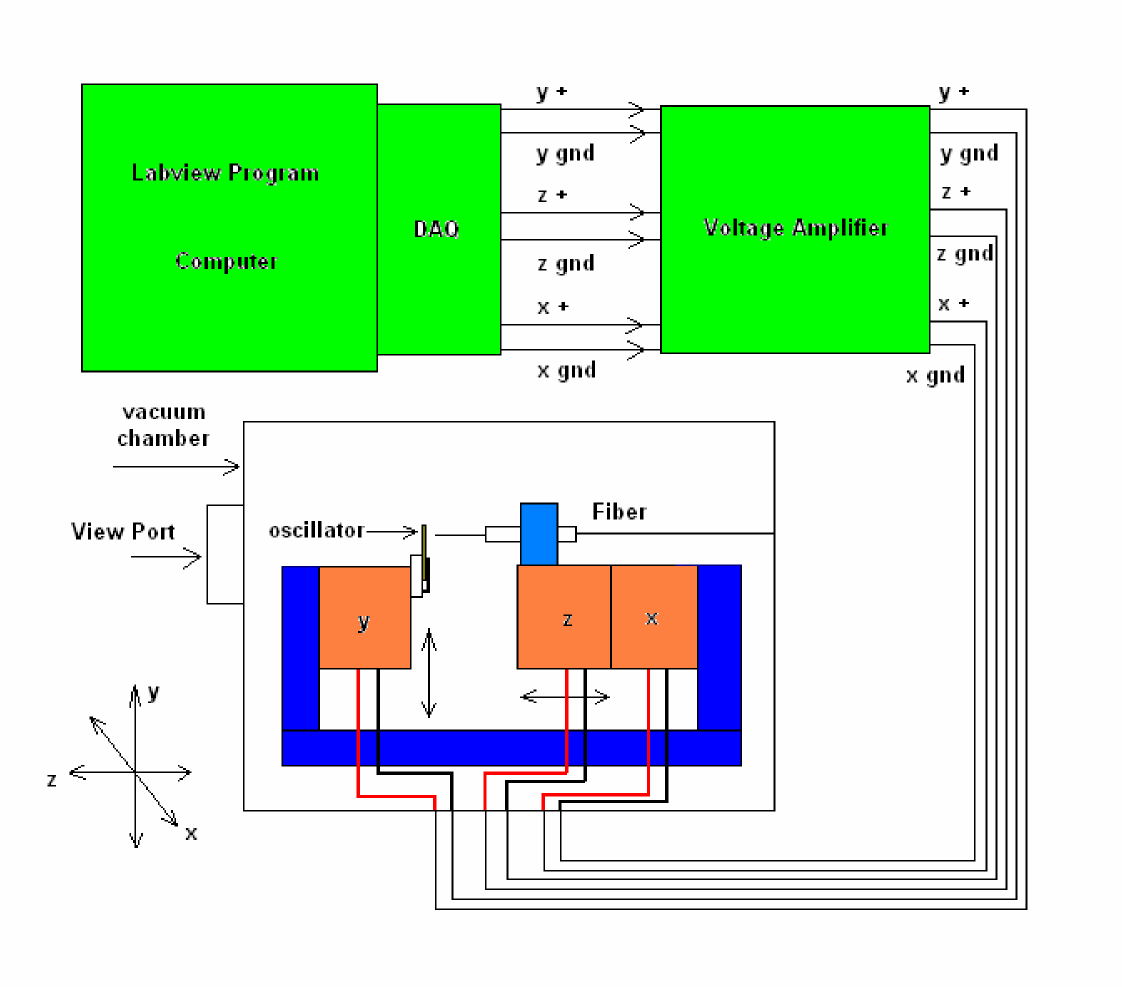

Fig. 4.8: Schematic of connection of sawtooth voltage to piezos

4.2.3-2 Sawtooth waveform generated from microcontroller

Recently, we home built another sawtooth waveform generator by programming a microcontroller PIC16F84A. Microchip manufactures a series of microcontrollers called PIC. There are many different flavours available. A microcontroller is a "simplified version" of a computer. It has a CPU, some basic memory, and Analogue-To-Digital converters built in. Once you have learned how to program one type of PIC, learning the rest is easy. The microcontroller we are using is the 8-bit microcontroller PIC16F84A from microchip.com. The following picture shows the basic layout of the PIC16F84A. It has 18 pins. Port A (RA0~RA4) and port B (RB0~RB7) control the input and output, an external crystal oscillator drives the microcontroller through a clock input, the Vss is the external power source input, and the V_{DD} is the ground reference. The PIC16F84A microcontroller is a low power consumption device and very easy to program. There are only 35 instructions to learn. You can very flexibly use these instructions to control the input and the output of each pin (see Appendix B).

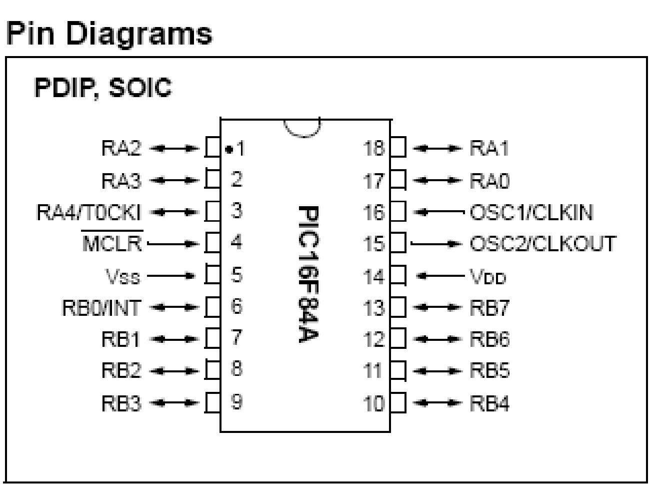

Fig. 4.9: Microchip PIC16F84A.

There are several ways of programming the PIC ----- using BASIC, C, or Assembly Language. We download a programming software MPLAB7.6 special for microchip from the website http://www.electronics-lab.com/. For this specific microcontroller the PIC16F84A, you can check the usage of each instruction and apply these instructions to your personal program. The following flow chart demonstrates how we make both the ramp up and the ramp down sawtooth waveforms from two simple PIC16F84A microchips.

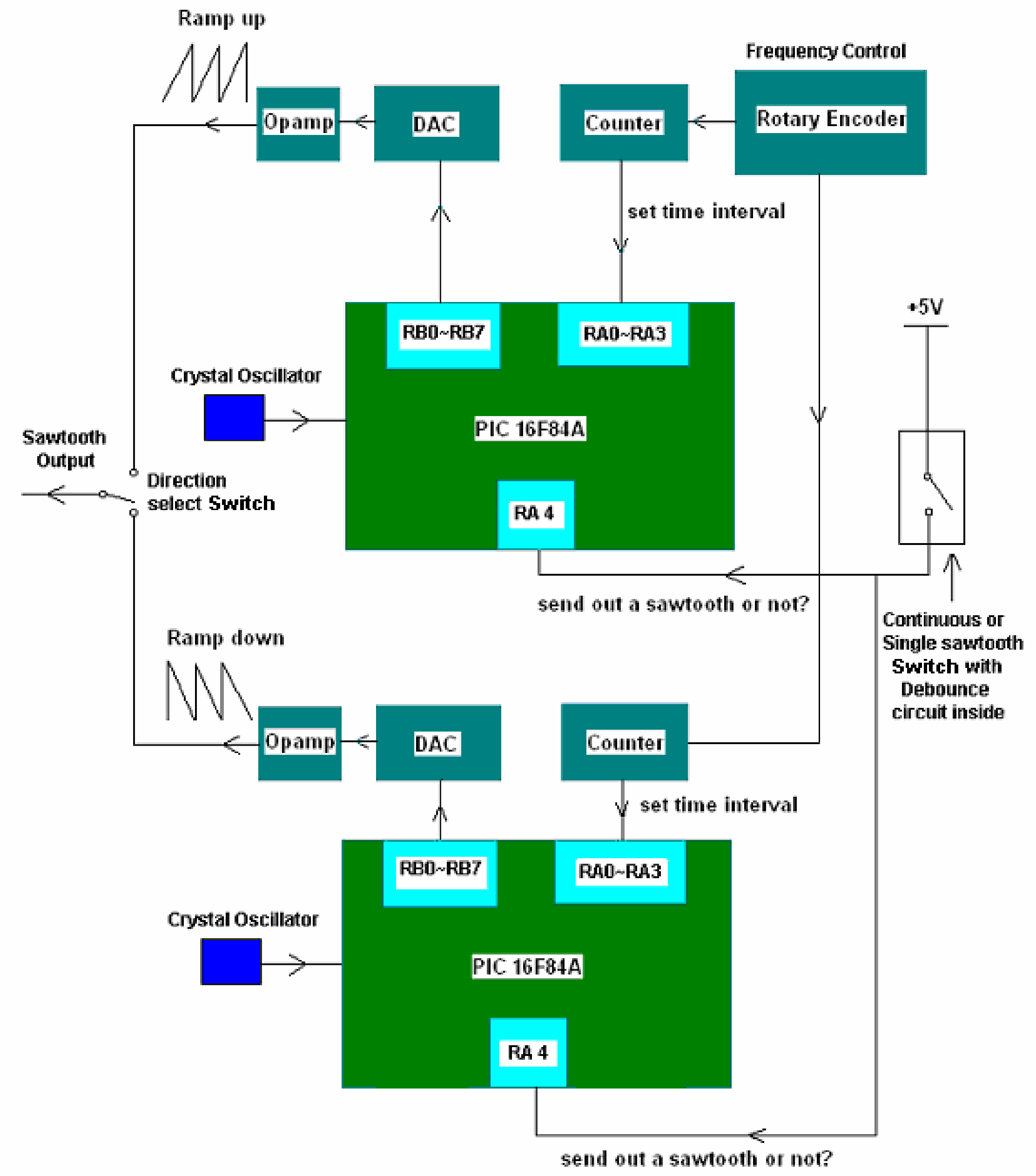

Fig. 4.10: Schematic drawing of sawtooth waveform from Microcontroller.

First we have to use the crystal oscillator to drive the microcontroller to let it run. We define the eight output/input pins (from RB0 to RB7) as sawtooth outputs. To control the sawtooth output, we have used the +5 V signal from an external circuit to trigger the RA-4 pin on the microchip to start the sawtooth function output. The microcontroller checks the voltage state of the RA 4 pin at all times. Once the +5 V high level state on the RA 4 has been detected, the microcontroller will automatically let the RB0~RB7 send out a sawtooth waveform in digital form (8 bit binary signal ranging from 0 to 255), and then the Digital-to-Analog converter (DAC) will convert this binary signal to the real analog sawtooth signal with an amplitude resolution of +5/256 V. After one sawtooth is generated, the microcontroller will keep checking the voltage state of pin RA4. If the voltage on pin RA4 is detected to be low, the microcontroller will continue to check its voltage level until the voltage goes to + 5 V, and then it will let the RB0~RB7 send out another sawtooth waveform. So if the voltage on pin RA4 is always high, the sawtooth waveform will be generated continuously by the microcontroller. We use a switch to choose two states----a continuous sawtooth and a single sawtooth. The continuous sawtooth is easily implemented----by keeping the voltage high on pin RA-4. So one switch state can connect to a + 5V DC power supply, another switch state will go to a + 5 V pulse output. One thing we have to be concerned about is that this +5 V pulse should have a width less than the period of a single sawtooth, otherwise we would get multiple sawtooth signals with only one pulse. Since the switch should be quick enough to make sure the contact duration time is shorter than one single sawtooth period, we have to use a debounce circuit to implement that.

What is a debounce circuit? And what is it used for? Here we would like to show you how it works and its application. Imagine you have made a logic circuit that counts up to ten. You press a button and the output increments not by one but maybe by five. On the next press, it steps by seven. What's going on? The answer lies in the inferior mechanical contacts of a switch. You press the button and the contacts will open and close many times before finally staying in position. This is known as contact bounce. it will bring a problem our sawtooth function generator. The contacts open and close before finally staying closed. A digital circuit will respond to each of the on off transitions. All that a switch debouncer circuit has to do is to filter out these transitions. There are several ways in which this can be achieved. The simplest method is to use a filter circuit containing a resistor and capacitor. The time constant must be at least 20ms to avoid contact bounce. The general idea is shown below:

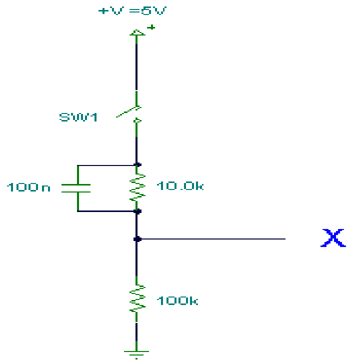

Fig. 4.11: A simple filter circuit for debounce purpose.

If we want to get the single sawtooth waveform for more precise positioning control, a single clean pulse is desired. With the aid of a simple Schmitt trigger such as the CMOS 4093 or 7414N, a clean output pulse can be achieved. The Schmitt trigger ensures that a clean output pulse will be produced. At this point, no matter how long you hold on the switch button, there is only one short pulse coming out and going to the RA4 pin, triggering the microcontroller and letting it generate only a single sawtooth output.

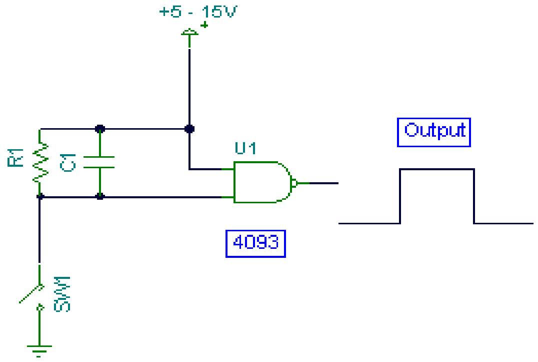

Fig. 4.12: Get much clearer pulse by using the schmitt trigger.

For the amplitude control of the sawtooth, we further amplify this sawtooth signal after the DAC to a higher amplitude by using a specific High-Current-Voltage OpAmp with different feedback resistor settings. Also, we can control the frequency of the sawtooth waveform. In order to do that, we use the rotary encoder to tell the counter the counting number we set, and the counter will convert this counting number to a 4 digit binary number ranging from 0000 to 1001 (corresponding to a decimal number between 0 and 9) and send it to the RA0~RA3 to set the time interval between every two step signals from the Port B eight output pins. As a result, we can achieve 10 frequency selections. We have used two microcontrollers. One is for a ramp up sawtooth output, and another is for a ramp down output. Once the program is ready, you can use a micro-chip programmer to burn the Assembly code to the microchip. You can purchase a commercial programmer for the specific microchip you already have. You can also build the microchip programmer yourself since it is very easy to make. There are many programmer circuit diagrams available online for reference. You can do a search and build your favourite. The following picture is one microchip code programmer we made.

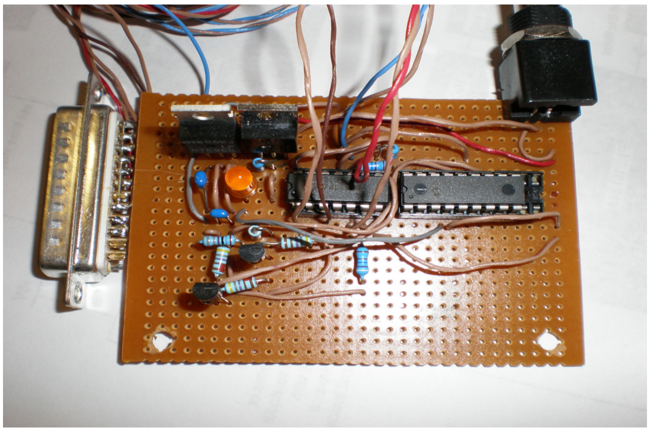

Fig. 4.13: Microcontroller Assembly Code Programmer.

You can refer to the associated schematic circuit drawing in Appendix B. In this Appendix, I will also show you how to program the microcontroller. This home-made function generator is much cheaper than the NI-DAQ card we bought.

4.2.4 Calibration of piezoelectric walker step size

Before we use this piezoelectric motor for interferometer alignment, especially for z-direction approaching, we have to calibrate the step size of the piezoelectric motor. From the stack piezo specification table we listed before, we can calculate the step size of the piezoelectric motor under one sawtooth waveform with a certain voltage amplitude. The AE0203D08F piezo at room temperature has a displacement of 6.1 ± 1.5 μm when applied voltage is 100 V. The relation between the displacement of the piezo and the voltage applied is linear. The smallest amplitude of the sawtooth waveform is +5 V. This voltage will displace the stack piezo by around 0.3 μm. We measure the real displacement of the stack piezo by using an interferometer signal. As we said before, the DC interference signal will change as the fiber is approaching the oscillator.

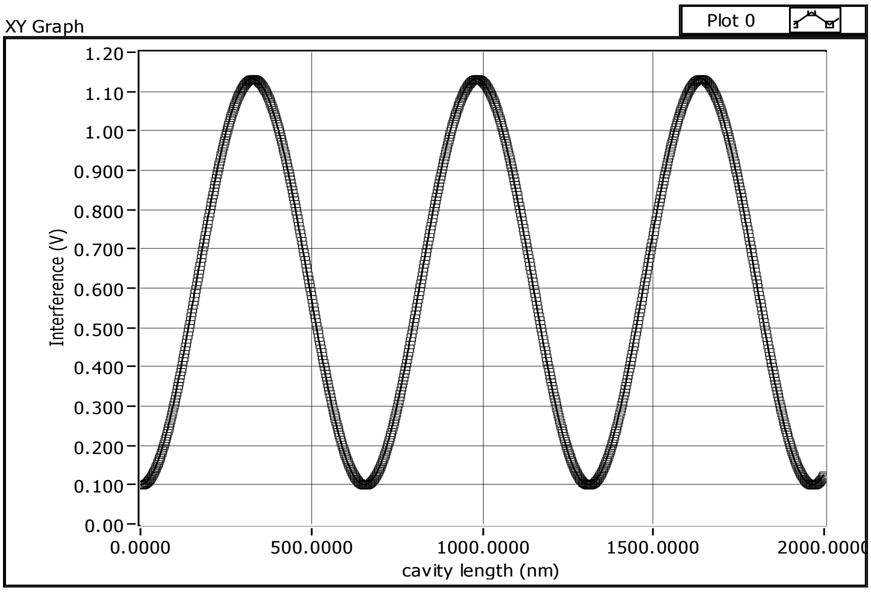

Fig. 4.14: DC interference signal (V) versus cavity length (nm).

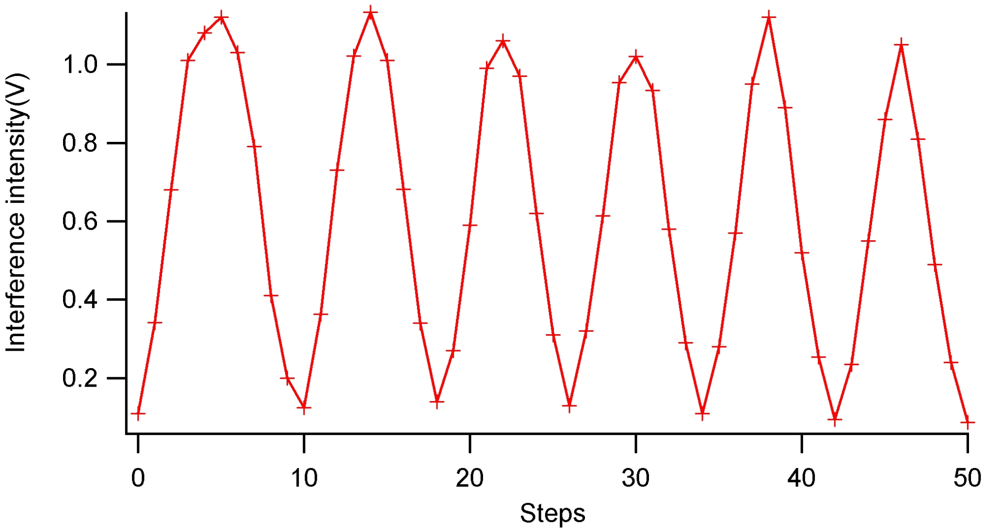

Fig. 4.15: DC interference signal (V) versus the steps of the 3-D positioned.

The wavelength of the infrared laser used is 1310 nm. Fig. 4.16 shows the DC interference signal as a function of the number of steps of our 3-D positioner (Fig. 4.15 shows the theoretical calculation). From the sinusoidal behavior of the DC signal, we can extract how much the fiber moves after each step. For clarity, we list our measurement results of the second interference period picture in Fig. 4.16 in the following table.

Interference Fringe (V)	Step (Forward)	Interference Fringe (V)	Step (Backward)
1.133	5	1.133	5
1.021	4	1.010	6
0.730	3	0.682	7
0.363	2	0.340	8
0.124	1	0.140	9

Table 4.2: Interference pattern versus moving step.

We plot the interference signal versus step for both the forward and backward movement Fig 4.17. In this plot, the red branch represents the forward step. In this case, the fiber gets closer and closer to the oscillator which can be monitored from this inference pattern. The blue branch represents the backward movement. As the fiber gets farther and farther away from the oscillator, the interference signal is changing as well. We put these two branches together for a comparison.

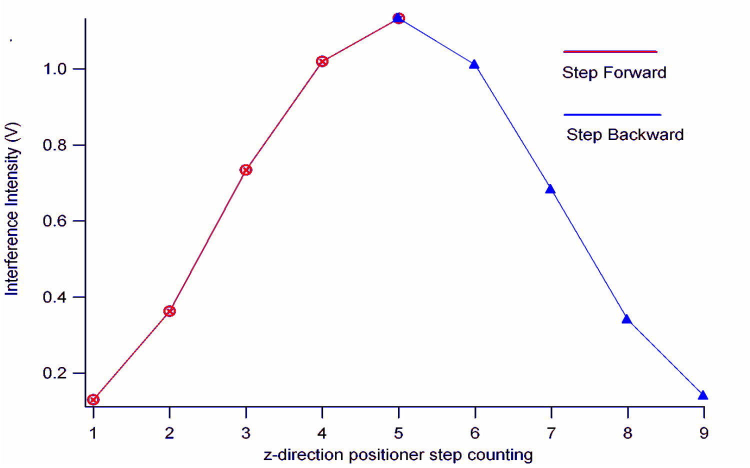

Fig4.16: DC Interference signal at each step.

From the plot above and by referring to the interference fringe as a function of cavity length, we can extract the average step size for both forward movement and backward movement

- Forward Average Step Size: 72.5 nm per sawtooth with amplitude of 10V
- Backward Average Step Size: 72.5 nm per sawtooth with amplitude of 10V

We can quickly get the average value of step size which is equal to 72 nm. And we can compare this average value with the calculated value 0.15 µm we got from the piezo specifications. They are very different from each other. The difference is because the value 0.15 µm is based on the assumption that when the piezo extends or contracts very quickly the copper clamping piece is exactly still, it won't move with the piezo even a little bit. That is just an ideal case, it won't happen in practice. Actually, the copper will be dragged by the sliding surface more or less due to the static friction force between them even when the piezo experiences the sharp ramp up or ramp down in voltage. At this point we have finished both mechanical and electrical setup for our piezoelectric motors for 3-D precise positioning control and we have done the calibrations for this 3-D positioner. Now it is ready for laser interferometer alignment.

4.2.5 Interferometer alignment by a 3-D piezoelectric positioner

Now we can apply this home-made sawtooth function generator box to our fiber-oscillator alignment in the same way as we did by using the DAQ outputs. The following figure shows us how this function generator box works:

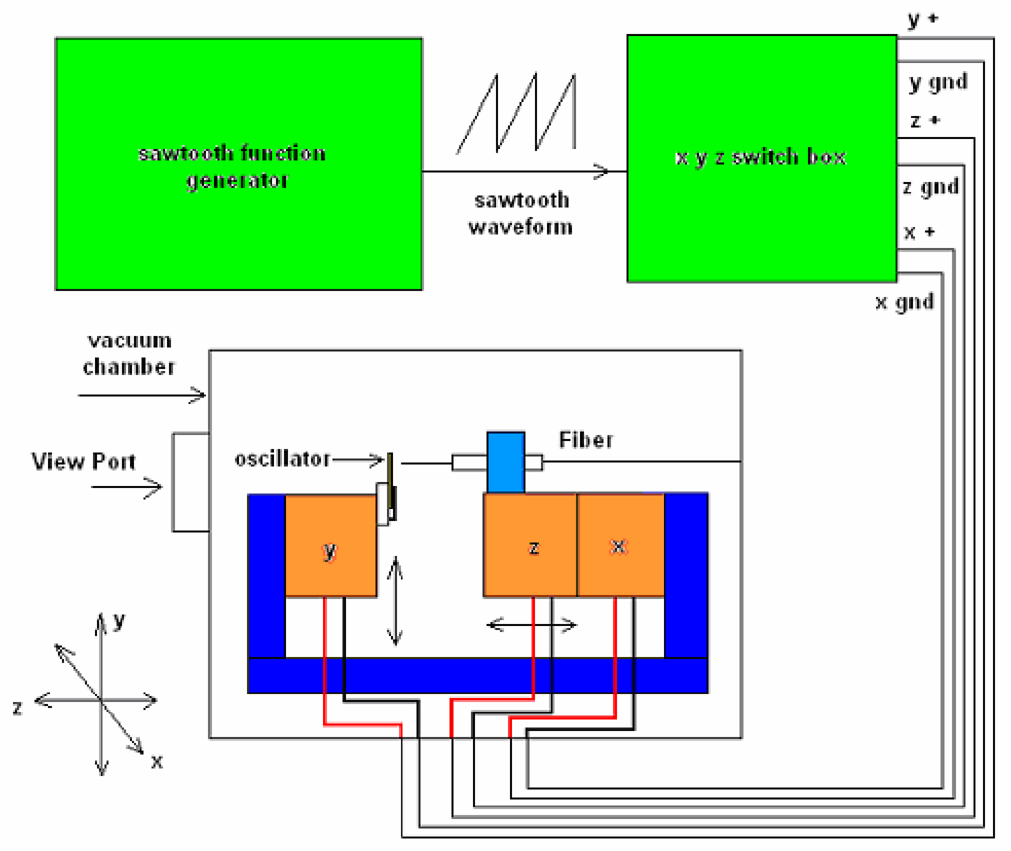

Fig. 4.17: Connection schematic for alignment by our sawtooth generator.

As you can see, we put one switch box immediately before the Attocube stage chamber to guide the sawtooth waveform to the different directional translator stages. Now let's describe how to align the fiber to the oscillator in detail. Usually we are doing the alignment under a microscope through the view port opened on the vacuum chamber. In our setup, as you can see from the above figure (Fig. 4.18), the x and z direction stages control the fiber movement while the y stage controls the oscillator movement. At the very beginning, we roughly move the fiber along the x-direction (left and right) by using a continuous sawtooth waveform with amplitude approximately 10 volts until you can see that the fiber end appears in a small window on the our oscillator chip, Then we switch to the y-direction stage to move the oscillator along the y-direction (up and down) to make sure that the lateral alignment is good. Finally, we do the z-direction approach. We switch to the z-direction control, and apply the forward sawtooth function to the z stage until the fiber nearly touches the oscillator. Watch out here! When doing the z-direction alignment, make sure that the sawtooth function you are going to apply to the piezo element is small enough and that the single sawtooth function mode is chosen. If the voltage is not small enough and the single sawtooth function mode is not chosen, then the fiber will most likely crash the fragile oscillator when it moves too fast. Avoid this case! When the fiber touches the oscillator, switch to the single backward sawtooth waveform with a smaller amplitude, and check the interference level when moving back the fiber from the oscillator. Again, make sure you still have a good interference pattern once you are away from the oscillator. To confirm whether this is a good interference signal, you can do the following. Displace the fiber away from the oscillator. When the laser hits nothing, you should only see the internal reflection from the fiber end. Then move the fiber back toward the oscillator, and you should recover the much larger interference signal. This means that the alignment of the fiber with the oscillator has been achieved.

Chapter 5 Characterization of E-Beam Lithography Fabricated Mechanical Oscillators

In this chapter we are going to show the characterization and analysis results for the double torsional mechanical oscillators that I fabricated. We will show out which vibration mode of our mechanical oscillators has the highest force detection sensitivity.

5.1 Characterization of the 50 μm scale mechanical oscillator

First we characterized the 50 μm scale oscillator by examining their structure with Scanning Electron Microscopy (SEM), as shown in Fig. 5.1.

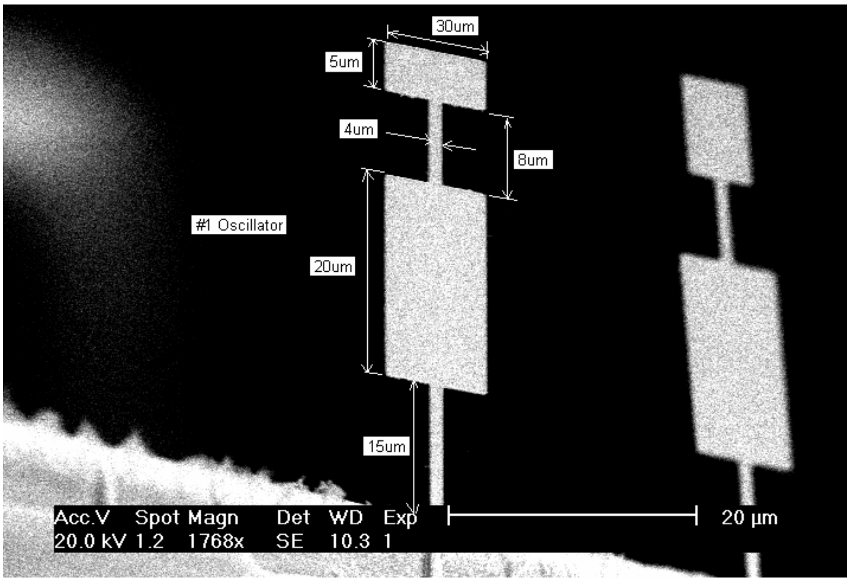

Fig. 5.1: Scanning Electron Micrograph of the 50 μm scale double torsional oscillators.

It is evident from Fig. 5.1 that the oscillators are relatively uniform, and their edges are quite clear; even the 4 μm feature (neck width) is very straight.

Next, we examine the oscillators with our infrared laser (1319 nm) interferometry in a vacuum of 1.4 mTorr. We got the fringe signal with a peak to peak value of 1.01 V (0.245 V-1.251 V). After locking onto the center of the fringe, we did the driven scan measurements on the oscillator shown in Fig. 5.1 to detect its four main oscillation modes (from the lower cantilever mode to the upper torsional mode). We used Labview program to control the DS345 function generator, and let it generate a sinusoidal waveform with an RMS amplitude of 0.1 V to externally drive the shaking piezo with the oscillator attached. The driven scan results are shown in the Fig 5.2(a-d)

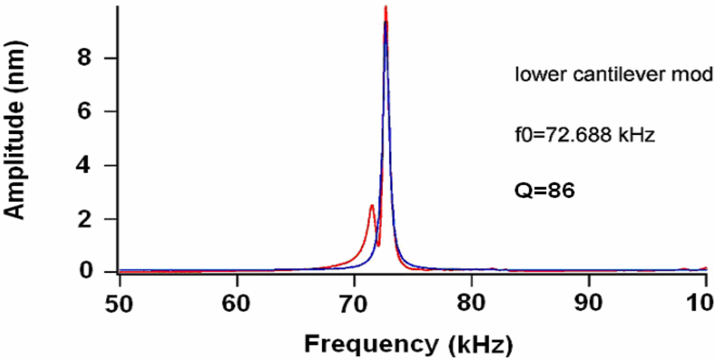

(a)

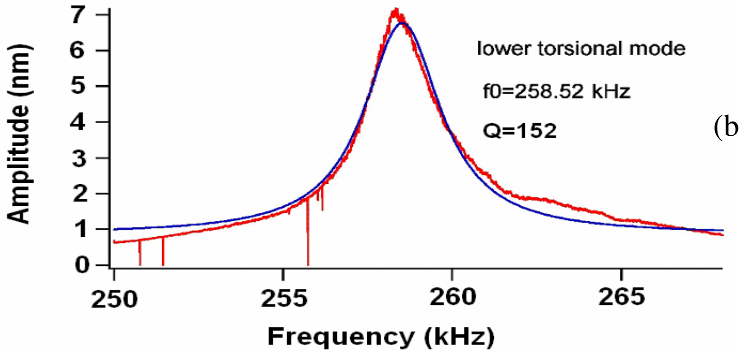

(b)

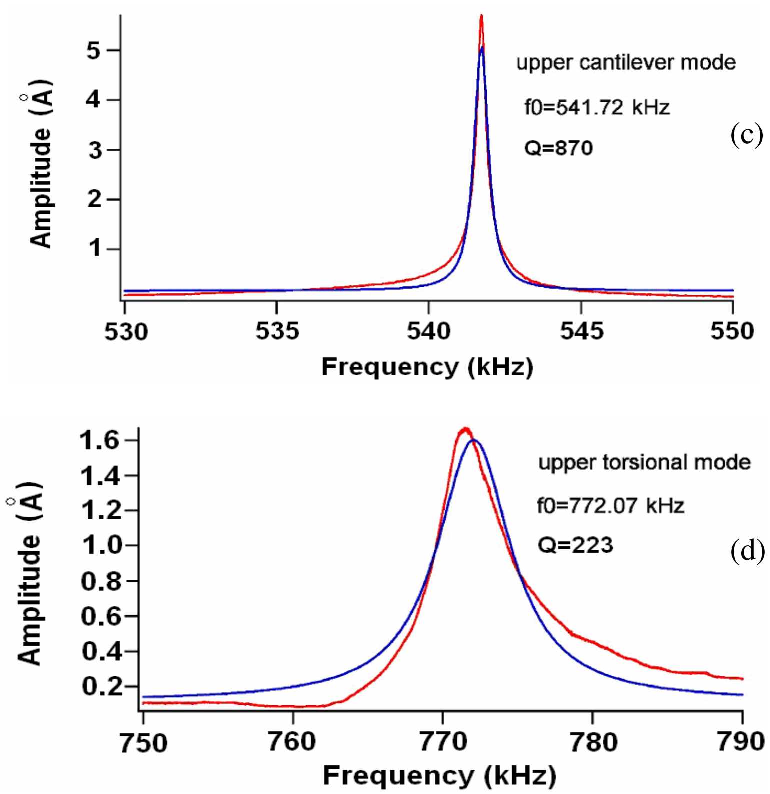

Fig. 5.2: The driven scan of the four vibration modes.

The resonance frequencies were determined from the peak locations, and Q values were determined from the widths. We also applied the FFT and ring down measurement technique to determine the spring constants and to verify the quality factors Q's of those vibration modes, and then we calculated the minimum detectable force for each vibration mode. We list the results in the following tables with the Finite Element Analysis (FEA) results as the comparison.

	Finite Element Analysis	Measurements
Lower Cantilever	69.1 kHz	72.69 kHz
Lower Torsional	237 kHz	258.52 kHz
Upper Cantilever	523 kHz	541.72 kHz
Upper Torsional	720 kHz	772.07 kHz

Table 5.1: The measured resonance frequencies as compared with FEA results *nm*

	Q Value	Effective Spring constant (N/m)	Minimum Detectable Force at room Temperature ($N/\sqrt{Hz}$)	Low T (0.3 K) Force sensitivity (predicted using room temperature Q) ($N/\sqrt{Hz}$)
Lower Cantilever	86	0.12	7.1×10^{-15}	2.3×10^{-16}
Lower Torsional	152	0.11	2.7×10^{-15}	8.6×10^{-17}
Upper Cantilever	870	0.087	6.9×10^{-16}	2.2×10^{-17}
Upper Torsional	223	0.074	1.1×10^{-15}	3.5×10^{-17}

Table 5.2: The minimum detectable force at room temperature and the predicted force detection sensitivity at very low temperature (0.3 kelvin)

5.2 Characterization of 150 μm Scale Mechanical Oscillator

Then we characterized the 150 μm scale double torsional mechanical oscillator similarly. The SEM is shown in Fig. 5.2.

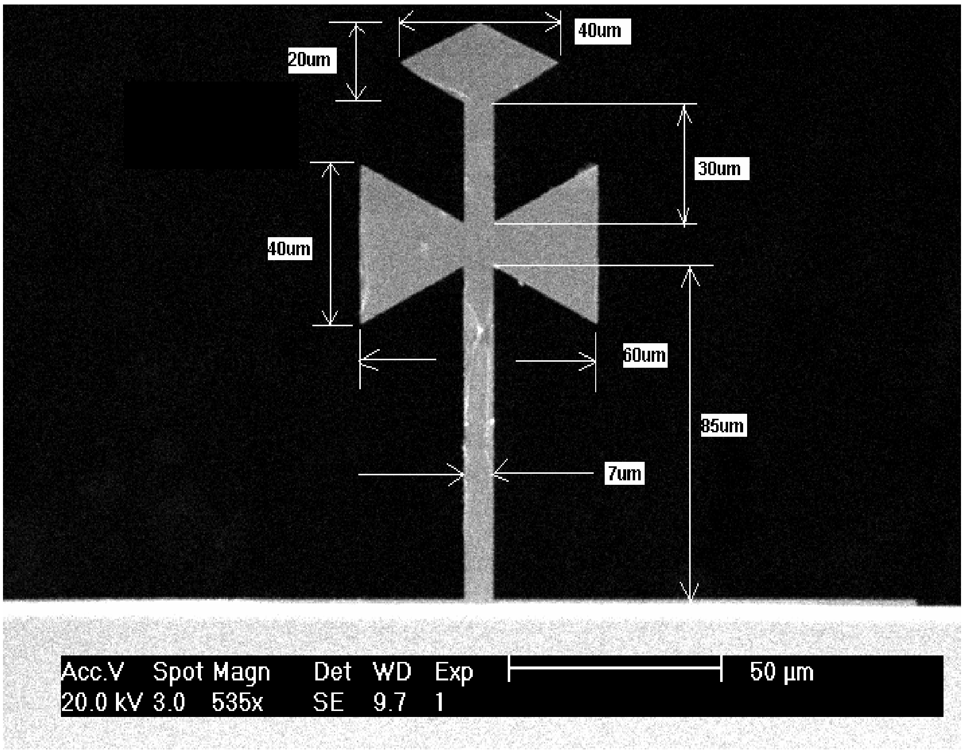

Fig. 5.3: Scanning electron Micrograph of the 150 µm scale double torsional oscillators.

The driven scan results for the four main vibration modes are shown in Fig 5.4(a-d). From the top to the bottom are the lower cantilever mode, lower torsional mode, upper cantilever mode, and upper torsional mode. We then did the same measurements on this oscillator as we did to the 50 µm scale oscillator. We list the results in tables 5.3 and 5.4 with the Finite Element Analysis results as the comparison.

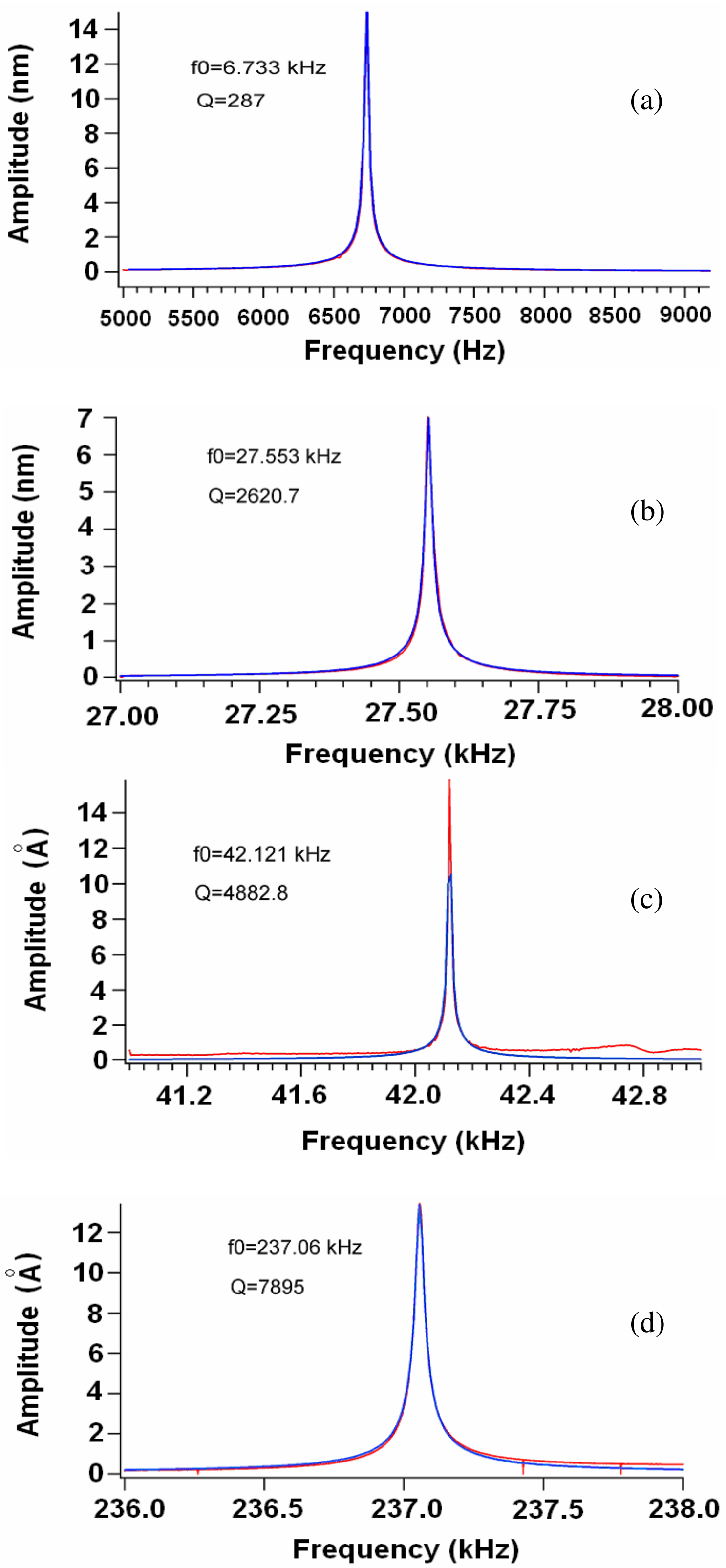

Fig. 5.4: The driven scan of the four vibration modes

	Finite Element Analysis	Measurements
Lower Cantilever	6.91 kHz	6.73 kHz
Lower Torsional	28.70 kHz	27.55 kHz
Upper Cantilever	45.25 kHz	42.12 kHz
Upper Torsional	220.19 kHz	237.06 kHz

Table 5.3: The measured resonance frequencies as compared with FEA results.

	Q Value	Effective Spring constant (N/m)	Minimum Detectable Force at room temperature ($N/\sqrt{Hz}$)	Low T (0.3 kelvin) Force sensitivity (predicted using room temperature Q) ($N/\sqrt{Hz}$)
Lower Cantilever	287	0.025	5.8×10^{-15}	1.9×10^{-16}
Lower Torsional	2621	0.014	7.2×10^{-16}	2.3×10^{-17}
Upper Cantilever	4883	0.009	3.4×10^{-16}	1.1×10^{-17}
Upper Torsional	7895	0.010	1.2×10^{-16}	3.8×10^{-18}

Table 5.4: The minimum detectable force at room temperature and the predicted force detection sensitivity at very low temperature (0.3 kelvin).

After comparison, we can see that the upper torsional mode of the 150 um scale has the highest force detection sensitivity at 0.3 kelvin. We hope this oscillator would help us to do some extremely small force and small mass detection. In the next chapter, we are going to apply this vibration to the gold particle evaporation measurements. Also, for future magnetic force measurements, we are pleased to have reached our targeted detection sensitivity level.

Chapter 6 Gold Micromass Measurements Using a Silicon Mechanical Oscillator

In this chapter we are going to show how to use a mechanical oscillator to measure the extremely small mass deposited onto the oscillator by evaporation of gold from a cooling on a tungsten filament. This is a very basic application of our ultra-sensitive oscillators.

6.1 Introduction

We used filament evaporation to deposit gold onto the mechanical oscillator. First of all, let's review the basic of filament evaporation. Evaporation is a very basic and popular method to implement metallization in the semiconductor industry [53-56]. Metallization is the fabrication step in which proper interconnection of circuit elements is made. The purpose of this step is both to make ohmic contact to the devices and to connect them to the bonding pads on the chip's edge. Roughly speaking, evaporation involves three basic processes: 1) the solid metal must be changed into a gaseous vapor. 2) The gaseous metal material must be transported to the substrate. 3) The gaseous metal must condense onto the substrate. It resembles the familiar process by which liquid water appears on the lid of a boiling pot. Evaporation takes place in a vacuum, i.e., vapors other than the source material, are almost entirely removed before the process begins. In high vacuum (with a long mean free path), evaporated particles can travel directly to the deposition target without colliding with the background gas. In our case, we choose gold as the material to be deposited, and the mechanical oscillator as our evaporation substrate. In the following section we are going to deposit the Au material onto our mechanical oscillator using a tungsten filament, and then measure the amount of Au deposited on the oscillator from measuring the frequency decrease of the oscillator.

6.2 Gold sample preparation and gold micromass measurements

In order to set up our filament evaporation, we have to prepare our tungsten filament first. We wrapped a 10 mil tungsten wire approximately 10 cm long into the desired shape for our filament (Shown in the Fig 6.1). When we apply a DC current through the tungsten wire, we expect the tungsten wire would generate more heat to effectively evaporate gold. Due to the Ohm's law, the longer tungsten wire will generate more heat than the shorter one. Thus, we increase the resistance of the tungsten wire by increasing its length. Also, we need to put our tungsten filament in a very small spacing in a vacuum chamber, so we have to compress the tungsten wire. This is the reason why we wrapped this tungsten wire by multiple turns. The filament tip with a very small radius of curvature, due to needle point discharge, can provide strong potential. So this filament shape can evaporate gold more effectively. Then we immersed the tungsten filament into a Bright Brush Gold from Johnson Matthey Catalog Company, which is a liquid and black color so that the tip of the tungsten filament was covered by some amount of liquid gold. After that, the tungsten filament with bright brush gold was placed into an oven with temperature of 450°C for 15~20 minutes. Then the tungsten filament with Au on the tip was ready for the gold evaporation experiment (shown in Fig 6.1).

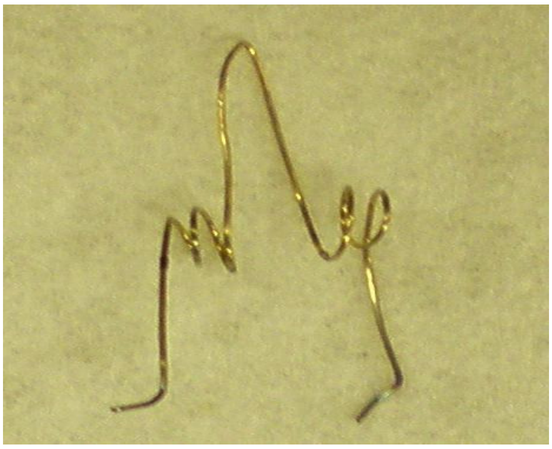

Fig. 6.1: A Tungsten filament with gold sample.

For the measurements, we placed our gold covered tungsten filament into the vacuum chamber and then hooked the tungsten filament up to an external DC power supply with a maximum current output of 2 amps. Once everything was ready, we pumped the vacuum to 1 mTorr using a mechanical pump. We applied a DC current to the tungsten wire after the pressure in the chamber became stable. This DC current was checked by a digital multimeter at all times. We put the tungsten filament approximately 2-3 mm away from the oscillator horizontally, and 1 mm higher than the oscillator vertically. The orientation of the filament with respect to the oscillator is important. The key point here is that the filament can not be placed too close to the oscillator otherwise the heat radiation from the filament will make the gold particles already deposited on the oscillator evaporate again, and as a result you will sacrifice some gold deposit material. If you move the filament too far away from the oscillator, it is very hard for the hot gold atoms to travel over a long distance to hit the oscillator, since they are dispersed over a large solid angle. Besides the horizontal distance, the vertical position also should be taken into account. If we put filament either too high or too low with respect to the oscillator, the Au still does not have a good chance to hit the oscillator. We tried the several different separation distances before finding the best orientation. The schematic setup and a photograph are shown in Fig. 6.5 and Fig. 6.6 respectively.

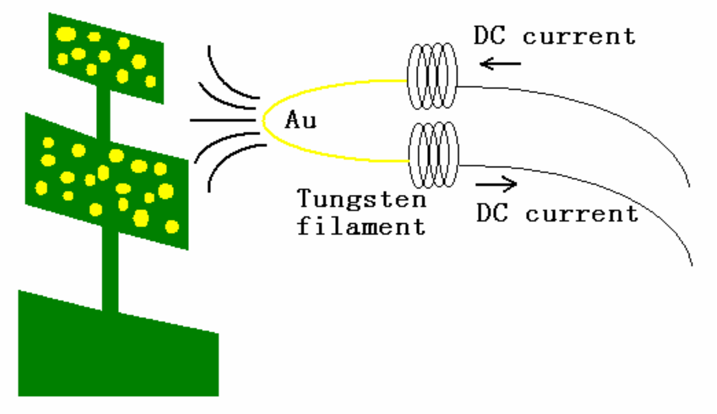

Fig. 6.2: Schematic drawing of the Au evaporation setup.

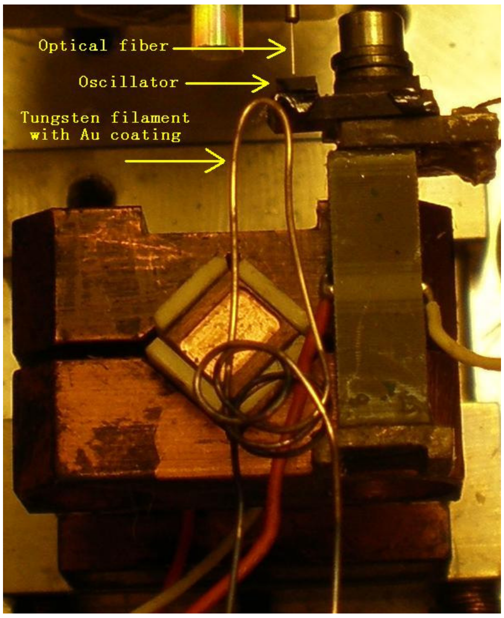

Fig 6.3: Photograph of the Tungsten filament setup.

The DC current makes the tungsten filament visibly hot after 8 seconds. The color becomes fairly bright red when the current is heating the tungsten wire. At this high temperature many gold atoms over the outer layer surface will get enough energy so that they will escape from the gold material layer on the top of the tungsten filament, and eventually some of them will be deposited onto the double torsional mechanical oscillator. When we apply the DC current through the tungsten wire for a while, say, one minute, some gold particles deposited on the oscillator will introduce extra mass which will lower the resonance frequency of the oscillator. The amount of the resonance frequency change depends on how much gold gets attached on the oscillator. Remember the resonance frequency of a mechanical oscillator is related to its mass and spring constant by:

$$\omega = \sqrt{\frac{k}{m}} \tag{6.1}$$

By differentiating Eq. 6.1, we have the following expression:

$$d\omega = \frac{1}{2}\sqrt{\frac{1}{mk}}dk - \frac{1}{2}\sqrt{\frac{k}{m}}\frac{dm}{m} = \frac{1}{2}\frac{\omega}{k}dk - \frac{1}{2}\frac{\omega}{m}dm \tag{6.2}$$

Divided by ω on both sides, Eq. 6.2 becomes:

$$\frac{d\omega}{\omega} = \frac{1}{2}\frac{dk}{k} - \frac{1}{2}\frac{dm}{m} \tag{6.3}$$

Thus, the frequency change of the oscillator is attributed to both the spring constant change and the mass change of the oscillator. First we did the evaporation test on a commercial AFM cantilever. We ran the first frequency sweep to figure out the initial resonance frequency of the AFM cantilever. The result is shown in the figure below.

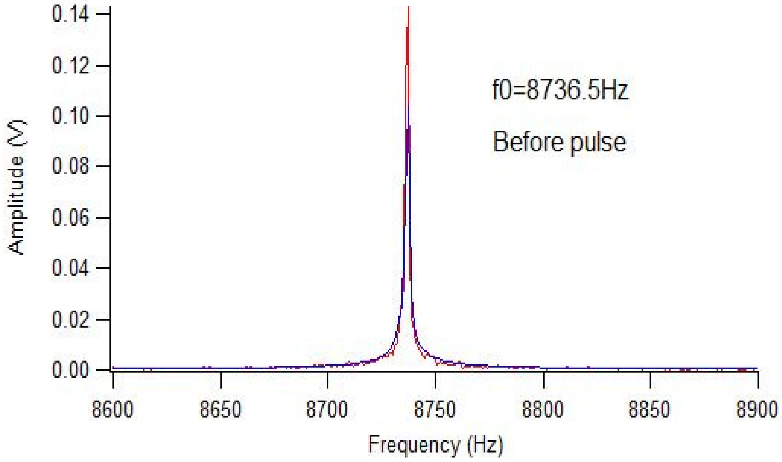

Fig. 6.4: Frequency sweep of the oscillator before the evaporation.

Assume the gold evaporation rate is constant, so the evaporation time should be proportional to the frequency change of the oscillator. We applied the DC current with a period of 2.5 minutes each time, and after each evaporation we did a driven scan to check the frequency change. The results are shown in the Fig. 6.6.

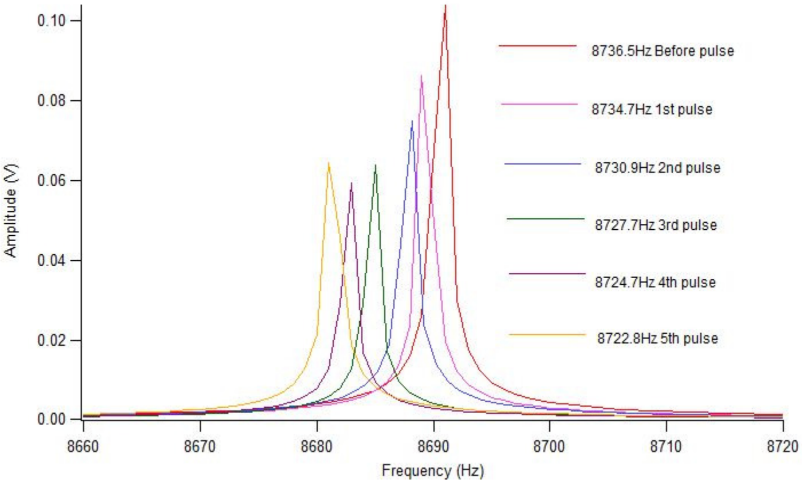

Fig. 6.5: Frequency scans with 6 pulses of DC current evaporation.

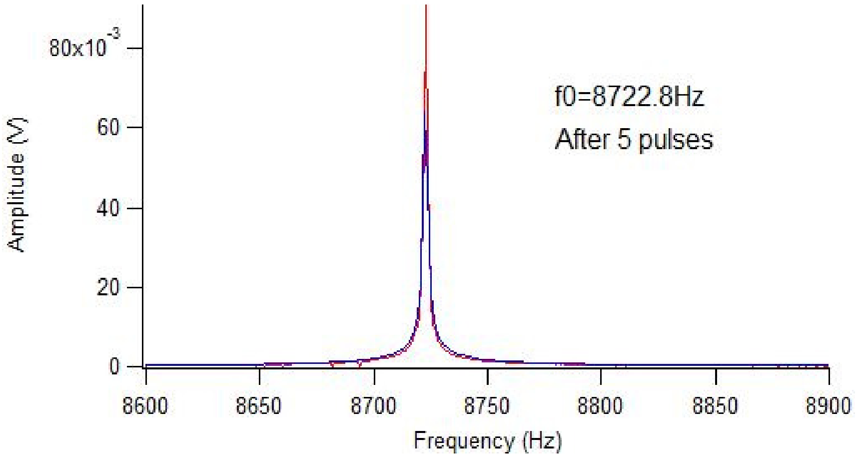

Fig 6.6: Frequency sweep of the cantilever after evaporation.

In this figure, we can see, the resonance frequency of the AFM cantilever keeps going down as we applied a series of DC current pulses. The amplitude also has a tendency to decrease. This makes sense. Because as mass gets accumulated over several evaporations, the resonance frequency should decrease. However we are more interested in how the resonance frequency varies with time. If we apply the DC current in a pulse manner, the amount of Au deposited onto the oscillator will also have a pulse behavior as a function of time. The Au mass deposited on the mechanical oscillator can be detected in terms of the frequency shift of the oscillator. Our previous frequency measurements have been done in the frequency domain. We have not done the frequency measurement as a function of time yet. So now the problem is how to do the time series data of frequency. Driven scans can not satisfy our requirement at this point. Remember when we check the X and Y outputs from the lock in amplifier, these two outputs have different phase behaviors. Based on these two outputs, we can figure out the vibration modes of the oscillator like we did in Chapter 2. Here we are more interested in the X output because it has a zero crossing at the resonance frequency of the oscillator. Once you find the frequency of the zero crossing of this phase signal, you have the resonance frequency. In other words, the zero crossing of the X output from the lock in amplifier is a signature of the resonance frequency of the oscillator. So in order to find out the resonance frequency change, instead of doing a driven scan, we monitor the zero crossing of the X output from the lock-in amplifier at all times, and adjust the frequency to maintain the zero crossing.

For test purposes, we had used a commercial AFM cantilever to do the previous evaporation detection. For a state-of-the-art measurement, we now switch to our mechanical oscillators to measure the gold deposition very precisely. First of all, we did a driven scan measurement of the cantilever before the evaporation to find out the initial resonance frequency of the oscillator. Here we chose the upper torsional mode of the oscillator. The reason for this will be explained in the discussion below. From the first driven scan, the Lorentzian curve is shown in Fig. 6.6 (a) and the curve fitting shows the resonance frequency to be 273.06 kHz.

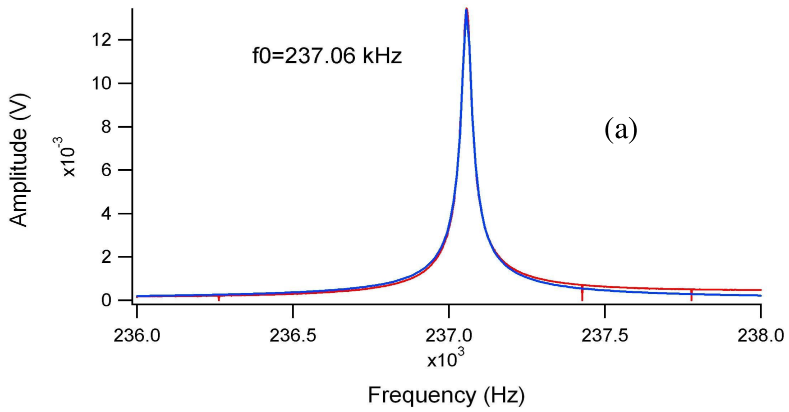

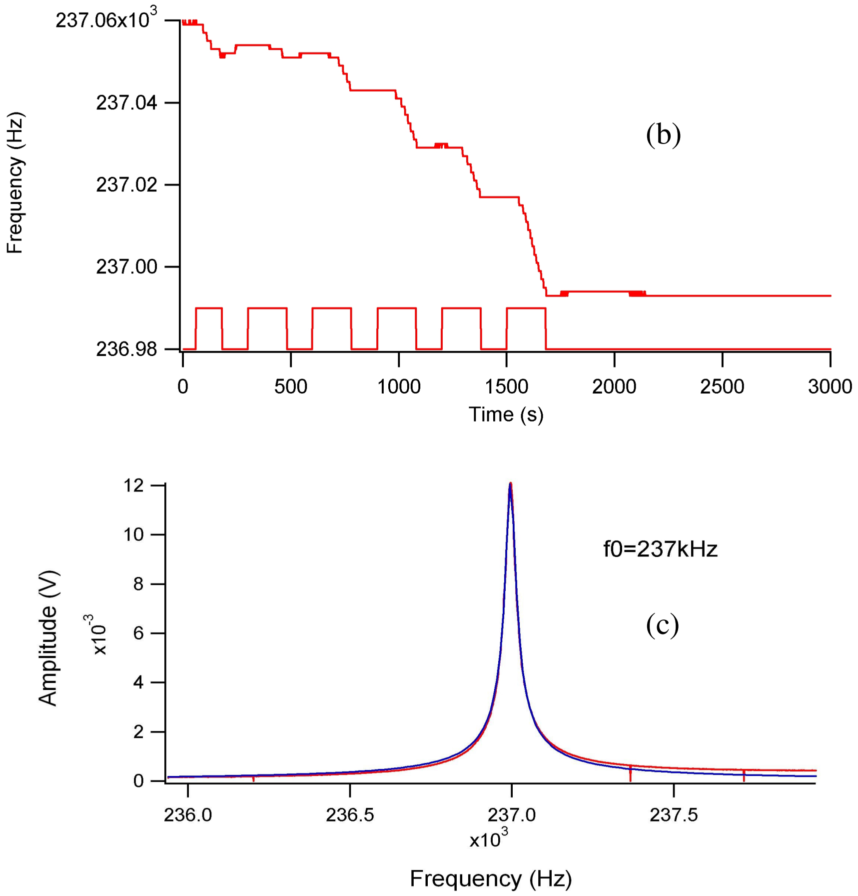

Fig. 6.7: In Fig. (a), we show the Amplitude versus frequency before gold evaporation. Fig. (b) shows the resonance frequency as a function of time during gold evaporation. Fig. (c) is the second Amplitude versus frequency after gold evaporation. The purpose of the second frequency scan is to verify the final resonance frequency of the oscillator after gold evaporation.

Then starting with that frequency, we wrote a Labview program to monitor the zero crossing of the X output. At the very beginning, under the resonance frequency, the X output definitely is equal to zero. At the same time we applied a series of DC current pulses. Based on the X output behavior, we see that if the reference frequency is below the resonance frequency, then the X output will be negative, when the reference frequency is above the resonance frequency, then the X output will be positive. So once the Labview program found the X went to negative, this feedback signal will make the program increase the reference frequency by a small value (e.g 0.5 Hz or 1 Hz), and vice versa. So by doing it this way, we can trace out the resonance frequency change of the oscillator as time goes by. The frequency time during evaporation result is shown in Fig. 6.6(b). For clarity, we put the pulse sequence in the same figure.

In our experiment, the DC current we used is 1.8 Amp, except the first pulse which had a width of 2 minutes, the remaining five pulses are 3 minutes long. The interval between pulses is 2 minutes. We can see a very clear step series. As we expected, during each DC current pulse applied through the tungsten wire, the filament gets hot until it is hot enough to evaporate the gold atoms or particles onto the oscillator. Thus, there is a certain delay for the frequency shift with respect to each pulse edge. Thereafter gold was continuously deposited onto the oscillator until a pulse is shut down. Accordingly, the resonance frequency of the oscillator also keeps going down. The little rise up from resonance frequency most likely comes from a temperature increase of the oscillator; this may also be why the last frequency decrease is so large, since it may also reflect a cool-down of the oscillator. When the Au evaporation by DC current pulse is finished, we will have a new resonance frequency of the oscillator. This frequency value can be easily double checked by another driven scan. The driven scan gave us another Lorentzian curve as shown in Fig 6.7 (c). From curve fitting we got the new resonance frequency which is exactly equal to the resonance frequency from the X output zero crossing monitor. They are in very good agreement with each other. In the following section we are going to briefly discuss the mass change based on the resonance frequency change of the oscillator.

6.3 Discussion and Analysis

As equation (6.1) shows, the resonance frequency change depends on two factors: one is the mass change of the oscillator, the other is the spring constant change of the oscillator. When we are doing the Au evaporation, let's assume that after each pulse, the mass of gold evaporated is dm, and the gold particles are uniformly deposited on the oscillator's surface with of an area of A. So the thickness of the gold layer on the oscillator is given by:

$$t_{Au} = \frac{dm}{\rho_{Au} A} \tag{6.4}$$

, where ρ_{Au} is the mass density of gold. If we simplify the oscillator as a rectangular beam, so the Au layer also has a rectangular shape. Thus the gold layer has the spring constant of [16]:

$$k_{Au} = \frac{Y_{Au} w_{Au} t_{Au}^3}{4L_{Au}^3} \tag{6.5}$$

and the oscillator has a spring constant of:

$$k_{osc} = \frac{Y_{osc} w_{osc} t_{osc}^3}{4L_{osc}^3} \tag{6.6}$$

, where Y_{Au}, Y_{osc} are the Young's modulus of the gold layer and the oscillator, respectively; $w_{Au}, t_{Au}, L_{Au}, w_{osc}, t_{osc}, L_{osc}$ are the width, thickness and length of the gold layer and oscillator, respectively. Now combine the double beams with different materials together-----one is the silicon beam, the other is the gold beam. When we apply an external force on the end of the beams, what happens? Look at the following figure:

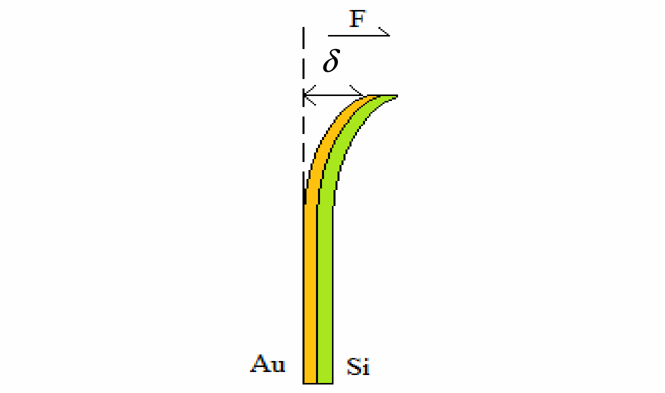

Fig. 6.9: Bending cantilever beam with double layers

If we bend these two beams together, the deflection displacement is δ, the external force is F. For the Au beam on the left, it experiences two forces: one is the external force F, the other is the restoring force F_r from the silicon beam on the right. So for these two beams, we have the equations:

$$\begin{cases} F - F_r = k_{Au}\delta \\ F_r = k_{osc}\delta \end{cases} \tag{6.7}$$

From these equations, we can get:

$$F = k_{Au}\delta + k_{osc}\delta = (k_{Au} + k_{osc})\delta \tag{6.8}$$

Thus the equivalent spring constant of the double layer system is:

$$k = k_{Au} + k_{osc} \tag{6.9}$$

So $dk = k - k_{osc} = k_{Au}$. Plugging everything into the equation (6.3), we have:

$$\begin{aligned}\frac{d\omega}{\omega}&=\frac{1}{2}\frac{dk}{k}-\frac{1}{2}\frac{dm}{m}\\&=\frac{1}{2}\frac{k_{Au}}{k_{osc}}-\frac{1}{2}\frac{dm}{m_{osc}}\\&=\frac{1}{2}\frac{E_{Au}t_{Au}^{3}}{E_{osc}t_{osc}^{3}}-\frac{1}{2}\frac{\rho_{Au}t_{Au}}{\rho_{osc}t_{osc}}\end{aligned}\qquad(6.10)$$

From this equation, we can see that the first term on the right hand side is proportional to $\frac{t_{Au}^3}{t_{osc}^3}$ with constant $\frac{E_{Au}}{E_{osc}}$, while the second term is proportional to $\frac{t_{Au}}{t_{osc}}$ with constant $\frac{\rho_{Au}}{\rho_{osc}}$. Since the thickness of the Au layer is much smaller than the oscillator thickness, i.e. $\frac{t_{Au}}{t_{osc}}$<<1, so $\frac{t_{Au}^3}{t_{osc}^3}$ is a very small number. Besides this, we also have $\frac{E_{Au}}{E_{osc}}=\frac{78\ \text{GPa}}{107\ \text{GPa}}<1$, and $\frac{\rho_{Au}}{\rho_{osc}}=\frac{19300\ \text{kg/m}^3}{2330\ \text{kg/m}^3}$>>1. As a result the first term in Eq. (2.8) is much smaller than the second term, thus we can ignore the first term including Young's modulus. Now we can approximate the frequency shift as a linear function of the thickness ratio of the Au layer to oscillator, and $\frac{\rho_{Au}}{\rho_{osc}}$ is a constant coefficient.

$$\begin{aligned}\frac{d\omega}{\omega_{res}}&=-\frac{1}{2}\frac{\rho_{Au}}{\rho_{osc}}\frac{t_{Au}}{t_{osc}}\\&=-\frac{1}{2}\frac{dm_{Au}}{m_{osc}}=-4.14\frac{t_{Au}}{t_{osc}}\end{aligned}\qquad(6.11)$$

From the frequency shift, we can determine the thickness of deposit gold on the oscillator and with known area A, we can then determine the mass of gold deposited onto the oscillator. In the equation above t_{osc}, m_{osc}, and ω_{res} are constants, and $d\omega$ depends on the frequency resolution of the lock-in amplifier. So in order to make measurement on the dm_{Au} or t_{Au} as small as possible, we can choose the ω_{res} with big value. This is the reason why we chose the upper torsional mode with a high resonance frequency of 237 kHz to take the measurements. By doing this, we can dramatically enhance our measurement sensitivity.

We can calculate the mass of gold added after each pulse by averaging over the last 4 pulses. Using the equation (6.11), we can express the mass of gold evaporation as:

$$dm_{Au} = -2m_{osc} \times \frac{d\omega}{\omega_{res}} = -2t_{osc} A\rho_{osc} \times \frac{d\omega}{\omega_{res}} \tag{6.12}$$

Based on the geometric size of the oscillator and silicon density, we can finally estimate that the average mass of gold after each DC current pulse is 1.99×10^{-16} kg, which corresponds to 6.1×10^{8} gold atoms. Our resolution is approximately $\frac{1}{10}$ of the mass deposited with a single pulse, or 6.1×10^{7} gold atoms.

6.4 Summary future work

We have developed electron-beam lithography techniques, and laser interferometry measurements, to fabricate and characterize ultra-sensitive oscillators. We are planning to apply our mechanical oscillators from electron-beam lithography to superconducting vortex dynamic measurements and one of the most exciting experiments ----Nuclear Magnetic Resonance Force Microscopy (NMRFM). The new generation of micro-oscillators is expected to extend their force detection sensitivity for such experiments from about 1×10^{-16} $\mathrm{N}/\sqrt{\mathrm{Hz}}$ to about 1×10^{-18} $\mathrm{N}/\sqrt{\mathrm{Hz}}$, that is, about 2 orders of magnitude.

Appendices

Appendix A

A-1 The DC current source for a laser diode

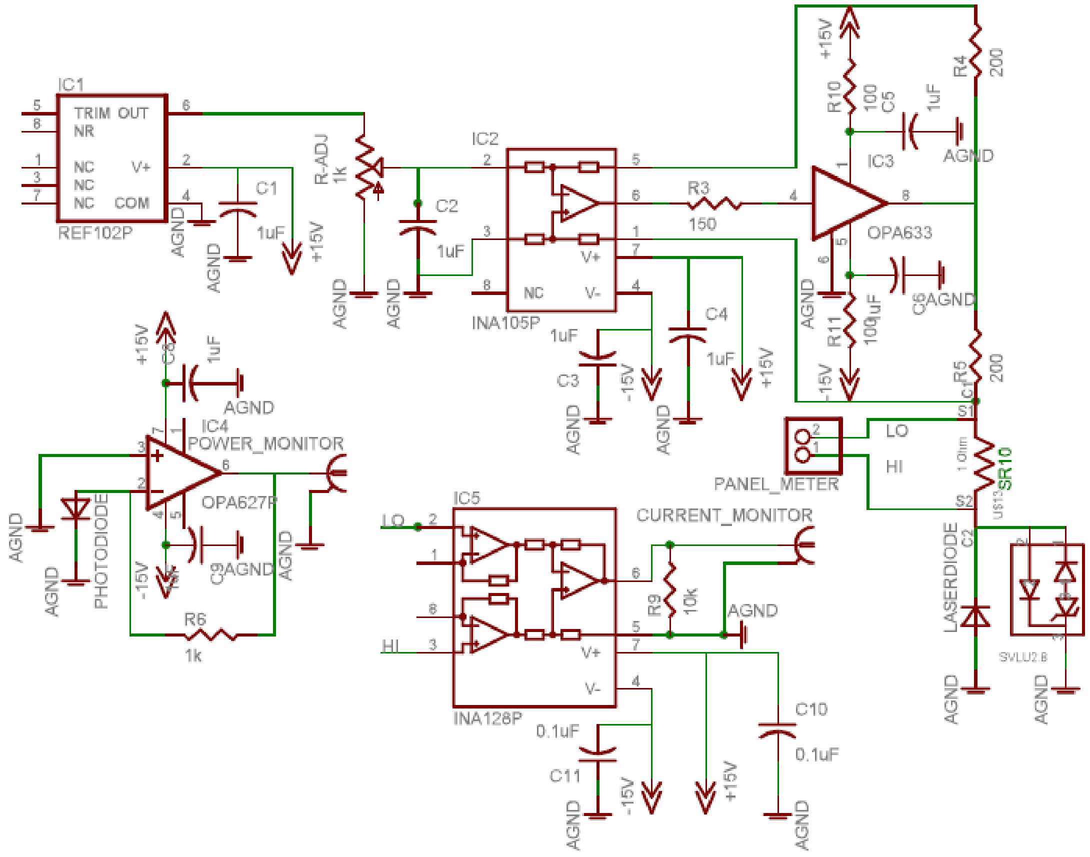

Fig. A-1: Schematic drawing of the DC current source of PD-LD laser diode.

This DC current source can provide 20 mA DC current to drive the laser diode from PD-LD Inc. and let it generate an infrared laser with wavelength of 1310 nm.

A-2 The fringe center lock feedback box

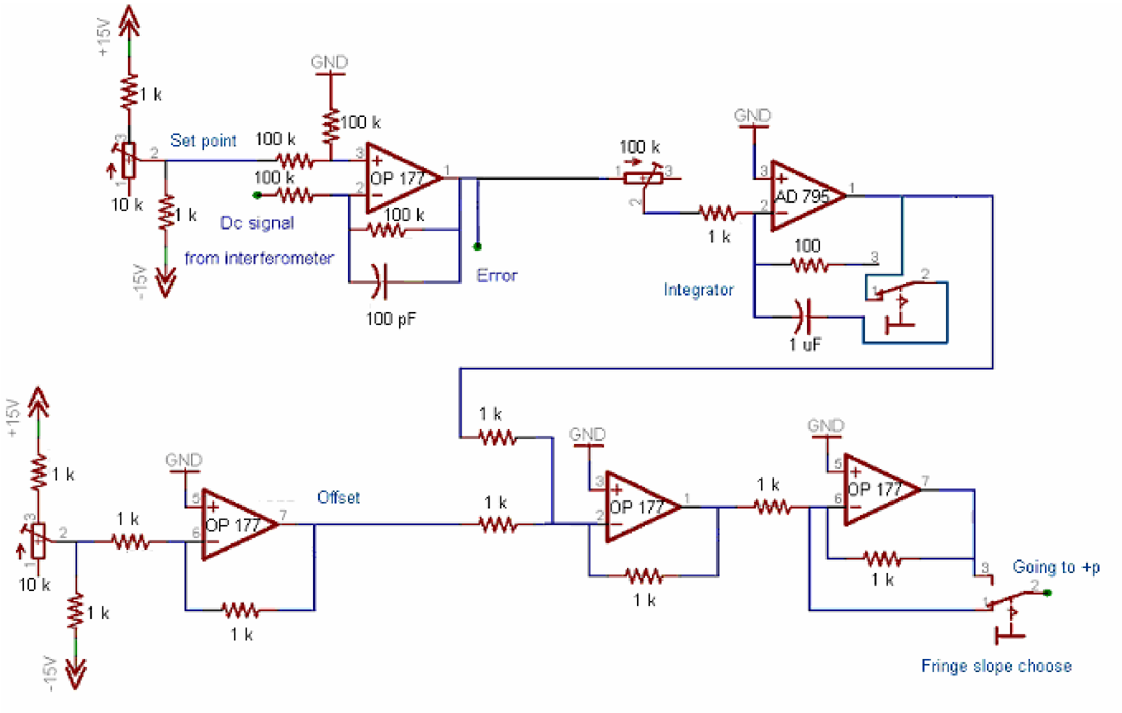

Fig. A-2: Schematic drawing of the fringe center lock feedback box.

Fig. A-2 shows the schematic drawing of our fringe center lock feedback box. This box is powered by a ±15 Volts power supply. We describe the usage of this box as follows.

a) Do alignment of a fiber with an oscillator, until you have a fringe signal. At this point, keep the box in the off position.

b) We turn on this box. Slowly adjust the offset voltage applied to the stack piezo by changing the variable resistor in the "Offset" circuit, and monitor the change of the fringe signal using a voltmeter. When we find the constructive point and the destructive point, we calculate the value of the fringe center, and then go to this fringe center.

c) We check the “error” output from another voltmeter when the fringe is at its middle position. Adjust the variable resistor in the “setpoint” circuit until the “error” outputs becomes zero. At the same time, we need to check the first voltmeter to see whether it is still the average value of the fringe. Usually, we have to change the offset variable resistor by several times before we can make sure the error output is zero when the DC fringe level is at its average level.

d) When we find the center position of the fringe signal with zero reading of the error output, we can turn on the integrator circuit. The purpose of this integrator is to calculate the accumulation of the shift from the center of the fringe due to some mechanism, such as thermal noise, and then to cancel this shift by an inversion amplifier in the last stage. Sometime, when we turn on the integrator, the fringe reading from the first voltmeter will jump to some value other than the average of the fringe signal. If this is the case, we need to turn on the second switch in Fig. A-2 to choose the correct fringe slope, or move to neighboring fringe, and then repeat the procedure from a) to d) until the fringe reading is stable.

e) When the fringe signal reading doesn’t change and the “error” reading is always zero, the center of the fringe is locked successfully. Then, it is ready for our measurements.

A-3 Introduction of Labview programs used in oscillator characterizations

A-3-1 Driven Scan program

The following figure shows the Labview program for driven scan. For details of these programs, please see the Labview files in the directory: C:\Documents and Settings\luweiut\My Documents\LabVIEW 7.1

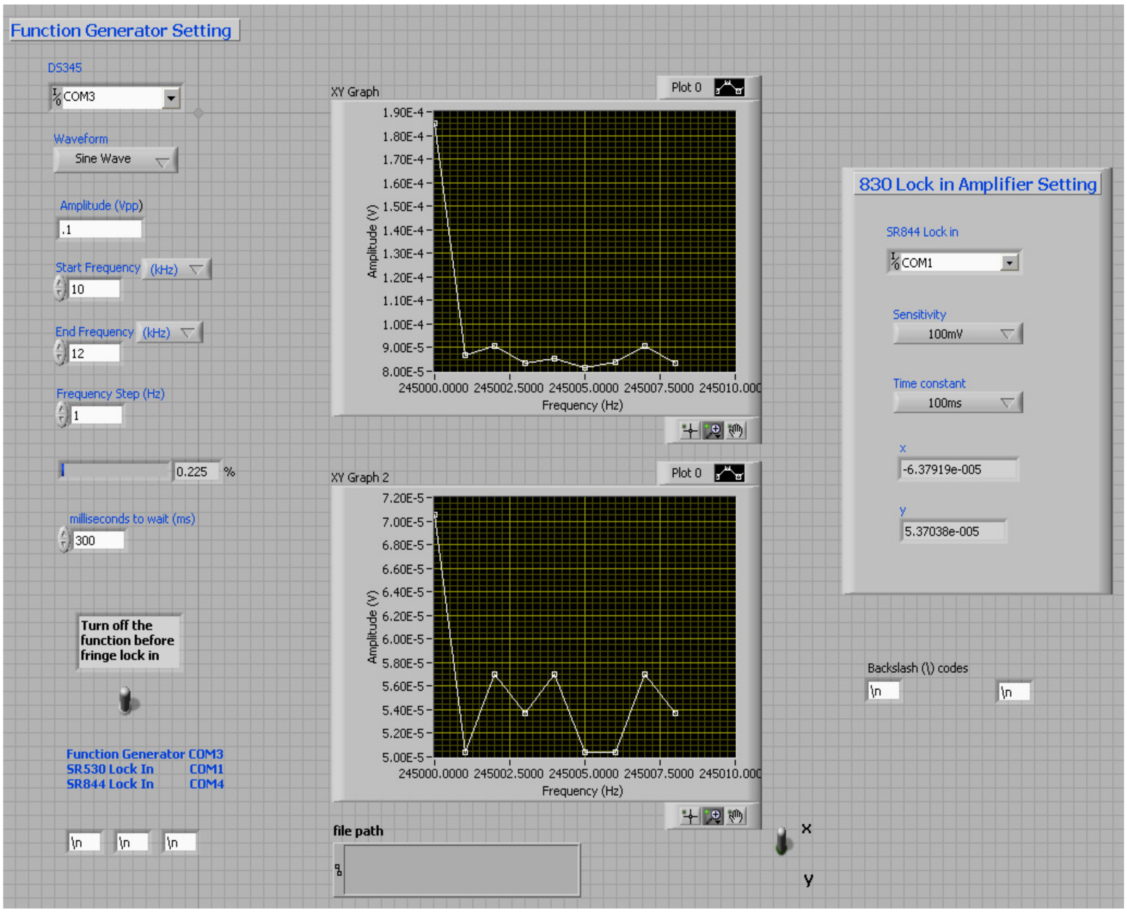

Function Generator Setting

DS345: COM3

Waveform: Sine Wave

Amplitude (Vpp): .1

Start Frequency (kHz): 10

End Frequency (kHz): 12

Frequency Step (Hz): 1

0.225 %

milliseconds to wait (ms): 300

Turn off the function before fringe lock in

Function Generator COM3
SR530 Lock In COM1
SR844 Lock In COM4

\n \n \n

file path

830 Lock in Amplifier Setting

SR844 Lock in: COM1

Sensitivity: 100mV

Time constant: 100ms

x: -6.37919e-005

y: 5.37038e-005

Backslash (\) codes: \n \n

Fig. A-3: The graphic user interfaces of the Labview program for driven scan. The left panel controls the setup for the Standford Research Systems (SRS) DS345, and the right panel controls the setup for the SRS SR844 lock-in amplifier. The top graph in the middle shows R outputs; the bottom graph shows X or Y outputs depending on the position of the toggle switch on the lower right. After the display, the raw data will be stored in a specific data file you define in the "file path" box.

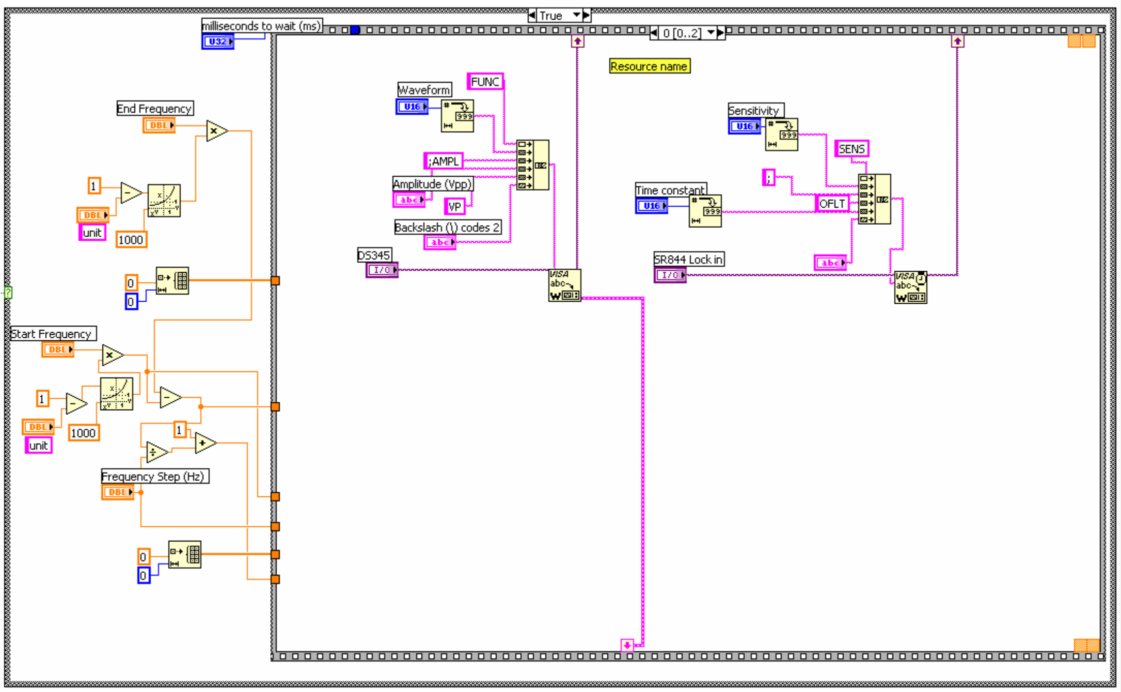

Fig. A-4: The Block diagram of the Labview program for driven scan measurements.

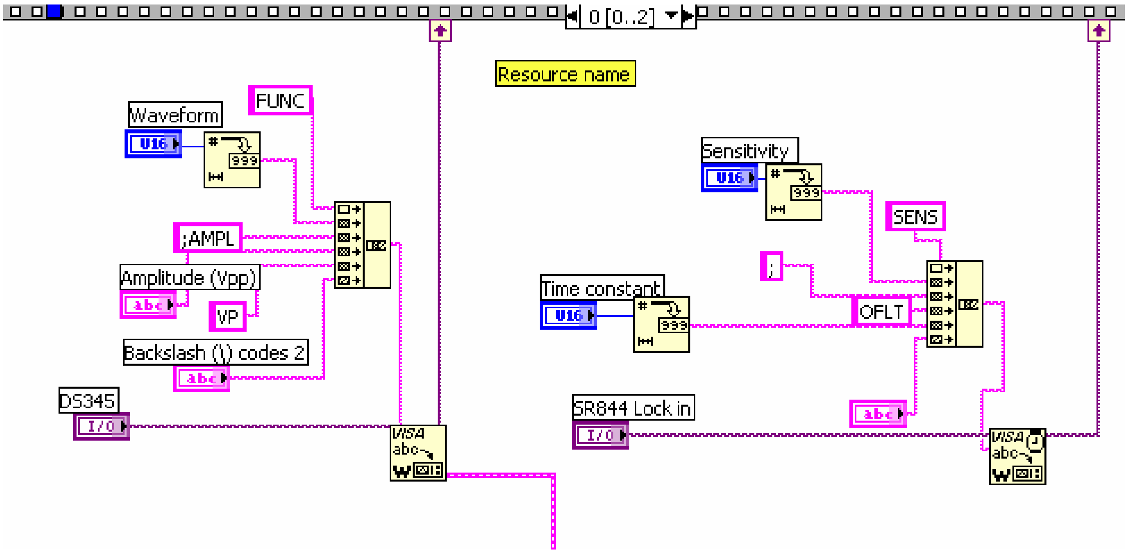

Fig. A-5: The set up for both the lock-in and the function generator.

This part shows the front panel settings for the DS345 and the SR844. It includes the set up such as waveforms, amplitudes, frequencies for the DS345, and time constants and sensitivities for the SR844 (It is also suitable for the SR830).

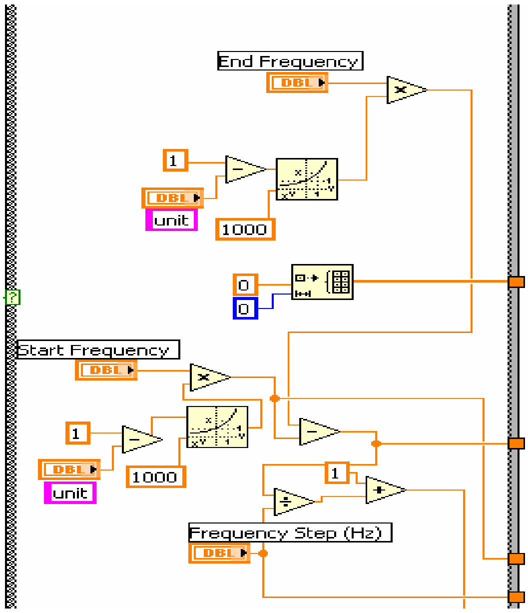

Fig. A-6: The frequency sweep setting for DS345, including the start frequency, the end frequency, and the frequency step.

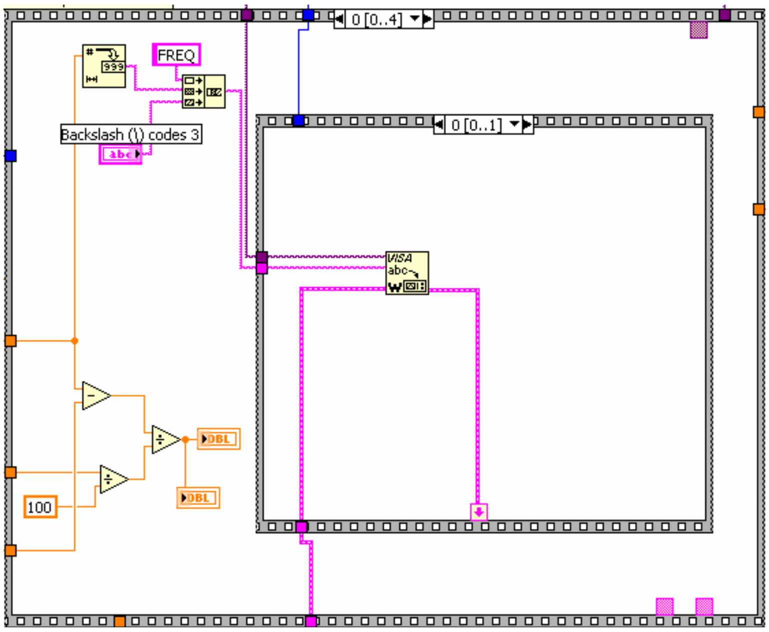

Fig. A-7: Send a frequency value to the DS345.

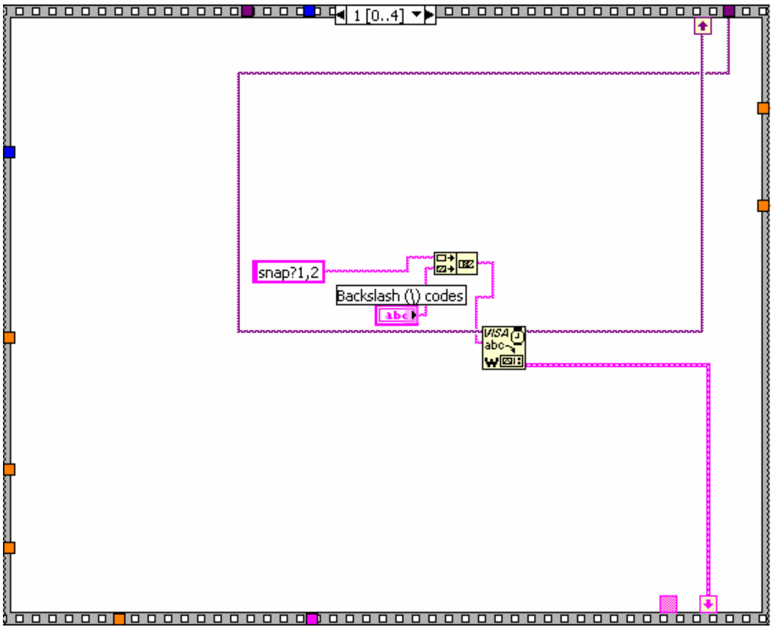

Fig. A-8: Let the lock-in output the X and Y

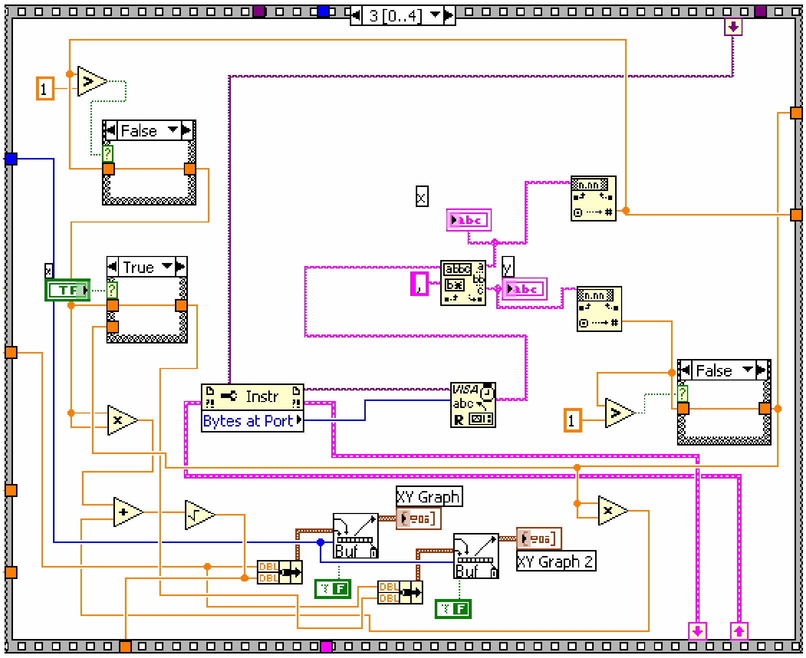

Fig. A-9: Calculate the R value from $R=\sqrt{X^2+Y^2}$, and plot the frequency versus amplitude.

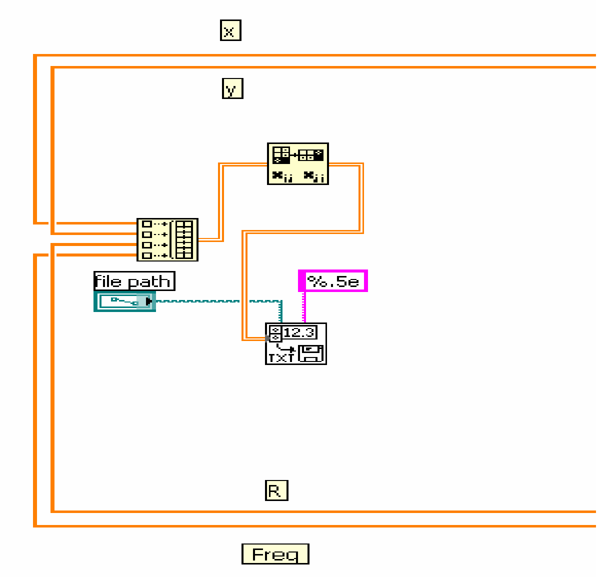

Fig. A-10: Store the X, Y, R, and frequency values in a data file.

A-3-2 Fast Fourier transform program

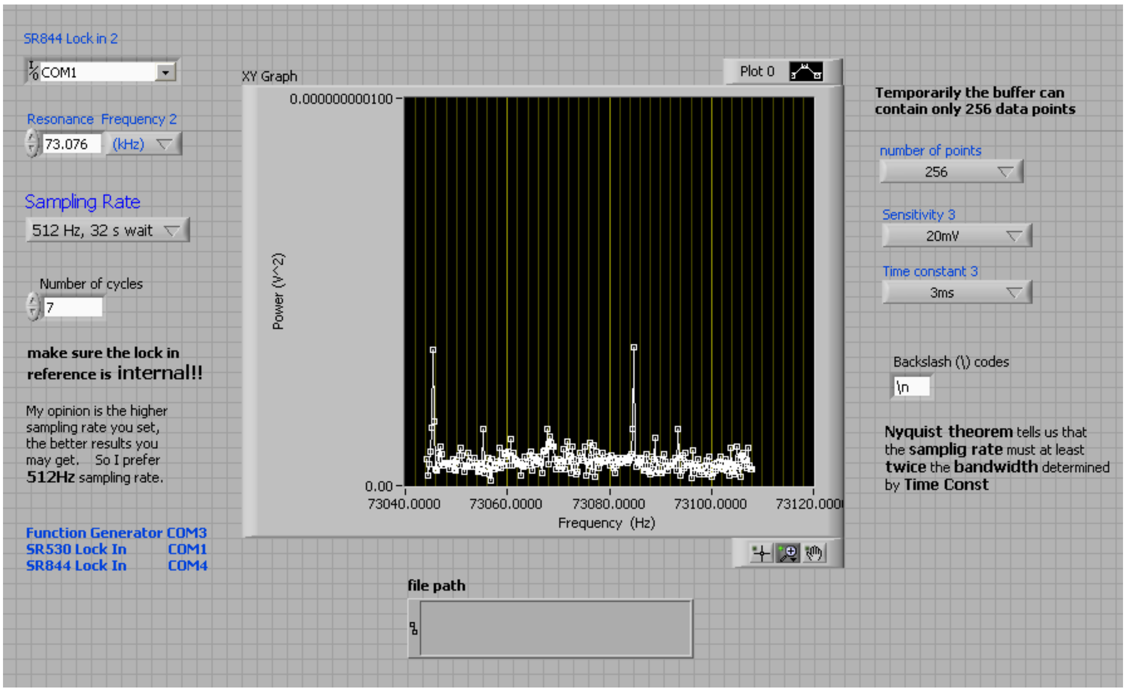

SR844 Lock in 2
COM1

Resonance Frequency 2
73.076 (kHz)

Sampling Rate
512 Hz, 32 s wait

Number of cycles
7

make sure the lock in reference is internal!!

My opinion is the higher sampling rate you set, the better results you may get. So I prefer **512Hz** sampling rate.

Function Generator COM3
SR530 Lock In COM1
SR844 Lock In COM4

file path

Temporarily the buffer can contain only 256 data points

number of points
256

Sensitivity 3
20mV

Time constant 3
3ms

Backslash (\) codes
\n

Nyquist theorem tells us that the **samplig rate** must at least **twice** the **bandwidth** determined by **Time Const**

Fig. A-11: Labview program for fast Fourier transform

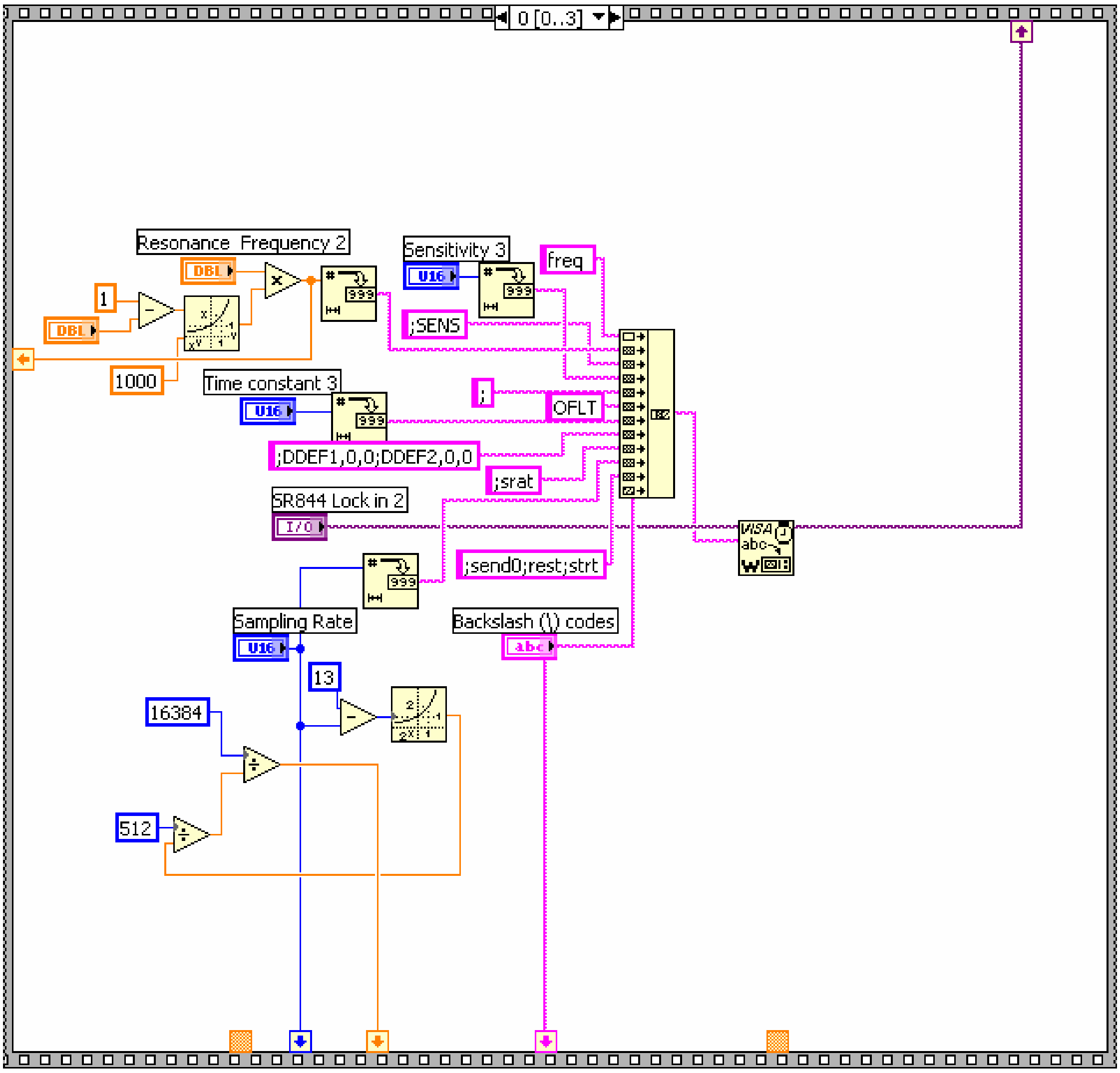

Fig. A-12: In this frame, we set up a reference frequency, a sensitivity, a time constant, raw data to be sampled (X and Y in this case), and a sampling rate, and then start the data acquisition. The full capacity of the lock-in is 16384 data points

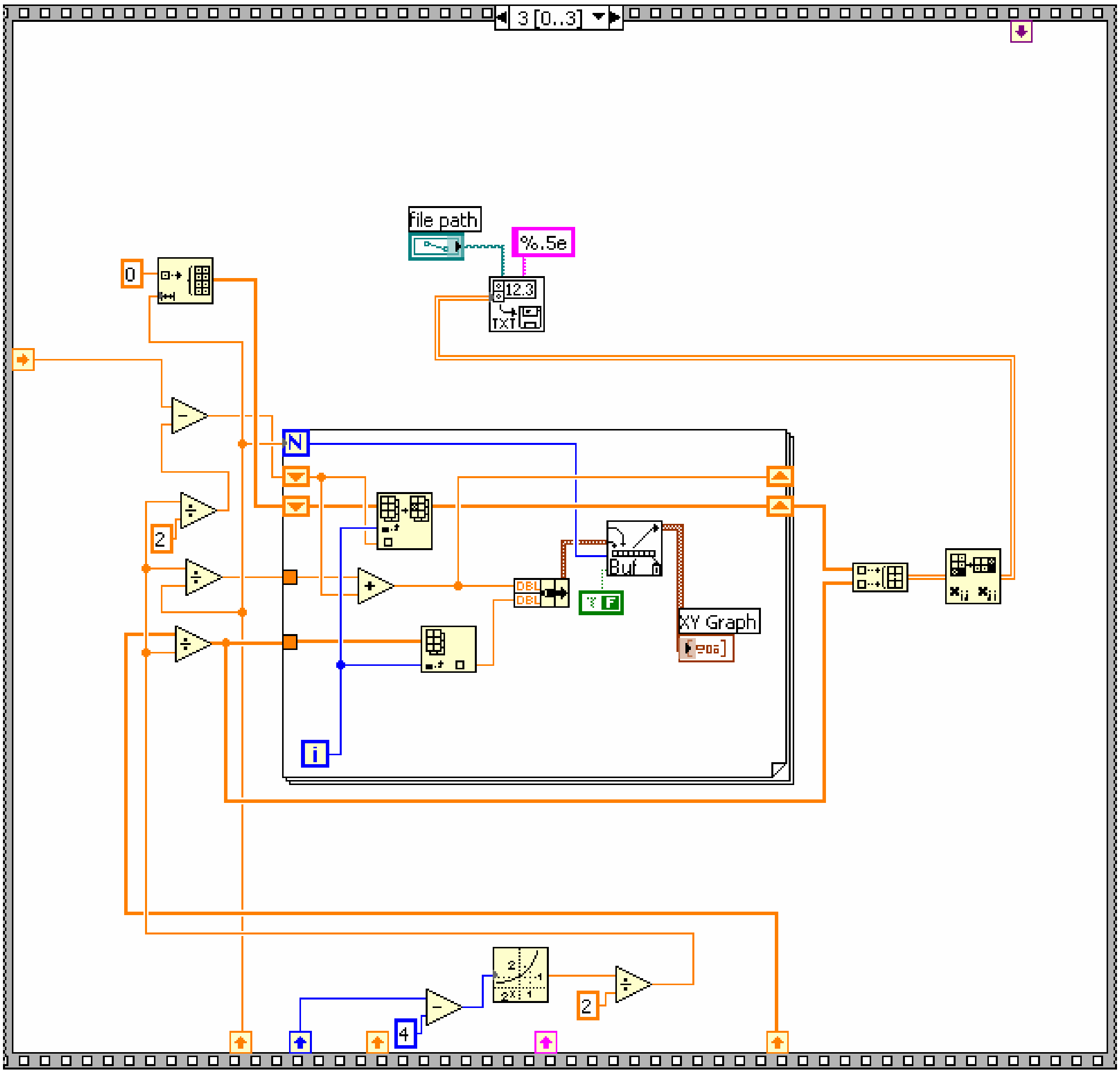

Fig. A-13: After data acquisition, we perform the fast Fourier transform to transfer the time series data into the frequency domain, and display the results in a graph, and then we store the data into a data file.

A-3-3 Ring down experiment

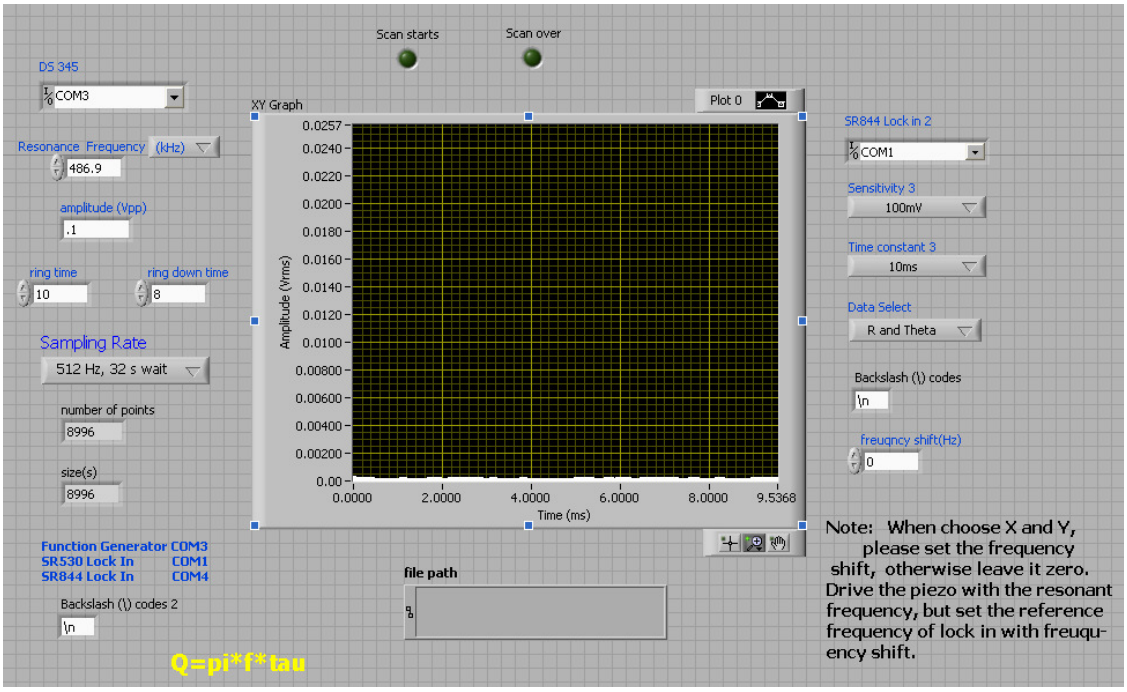
DS 345: COM3

Resonance Frequency (kHz): 486.9

amplitude (Vpp): .1

ring time: 10

ring down time: 8

Sampling Rate: 512 Hz, 32 s wait

number of points: 8996

size(s): 8996

Function Generator COM3
SR530 Lock In COM1
SR844 Lock In COM4

Backslash (\) codes 2: \n

Q=pi*f*tau

SR844 Lock in 2: COM1

Sensitivity 3: 100mV

Time constant 3: 10ms

Data Select: R and Theta

Backslash (\) codes: \n

freugncy shift(Hz): 0

Note: When choose X and Y, please set the frequency shift, otherwise leave it zero. Drive the piezo with the resonant frequency, but set the reference frequency of lock in with freuqu-ency shift.

Fig. A-14: The Labview program for a ring down measurement.

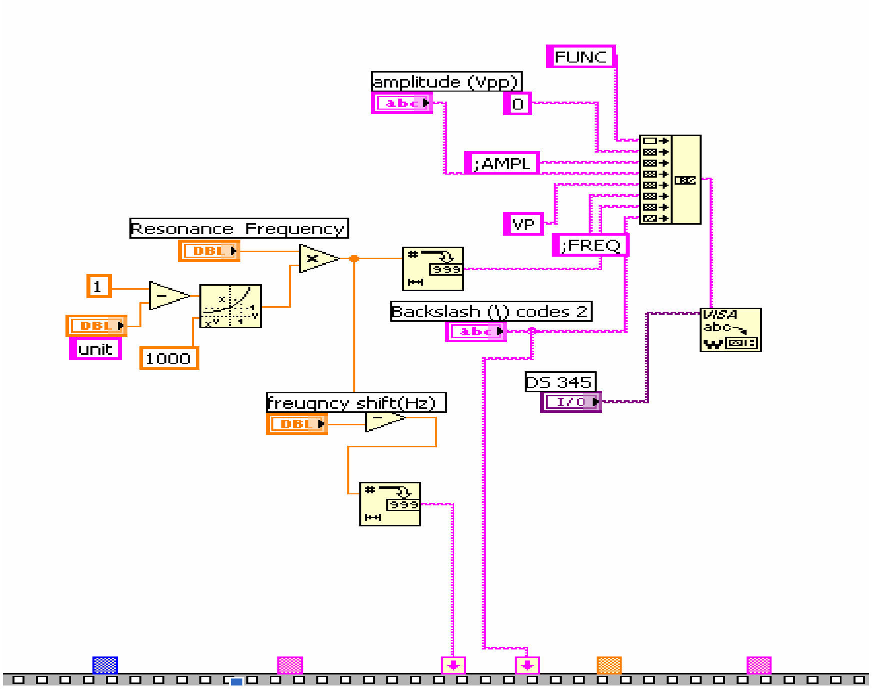

Fig. A-15: Set up a waveform, an amplitude, and a frequency (the resonance frequency of a mechanical oscillator) for DS345 function generator.

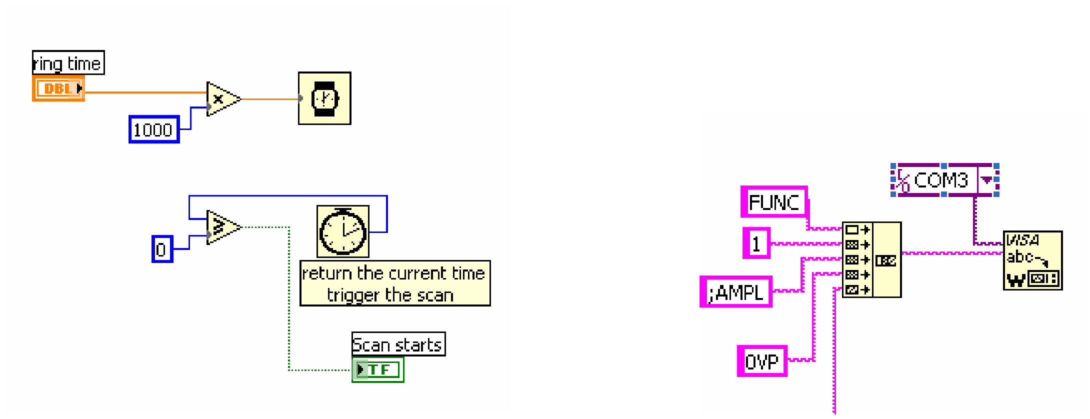

Fig. A-16: We set up a driving time, and then we stop the external driving force to let an oscillator go by itself.

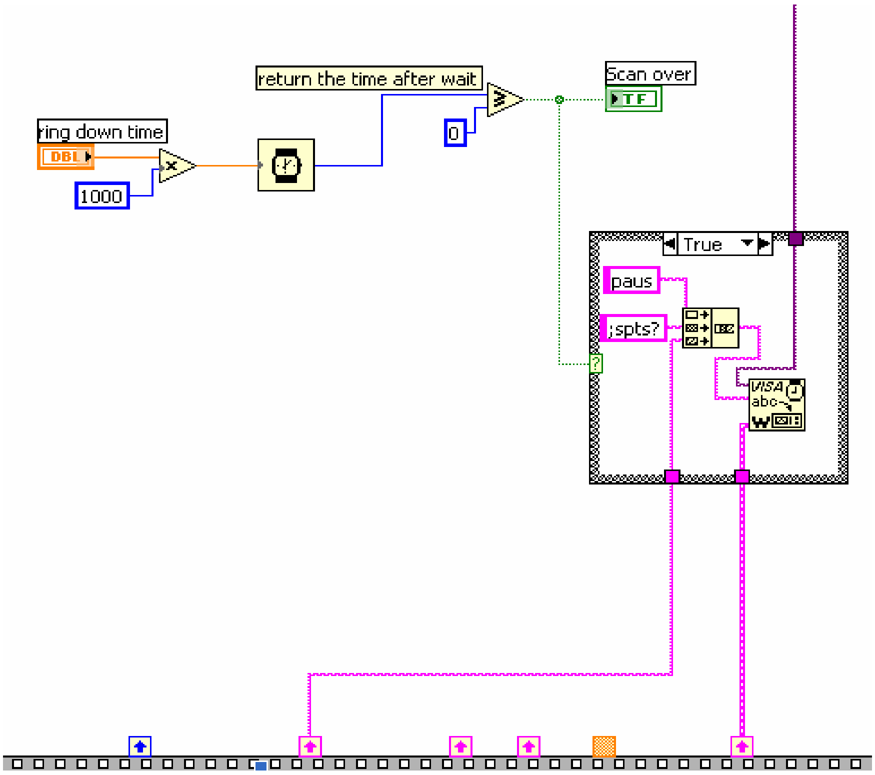

Fig. A-17: Let lock-in take raw data, and store the raw data into its internal buffer.

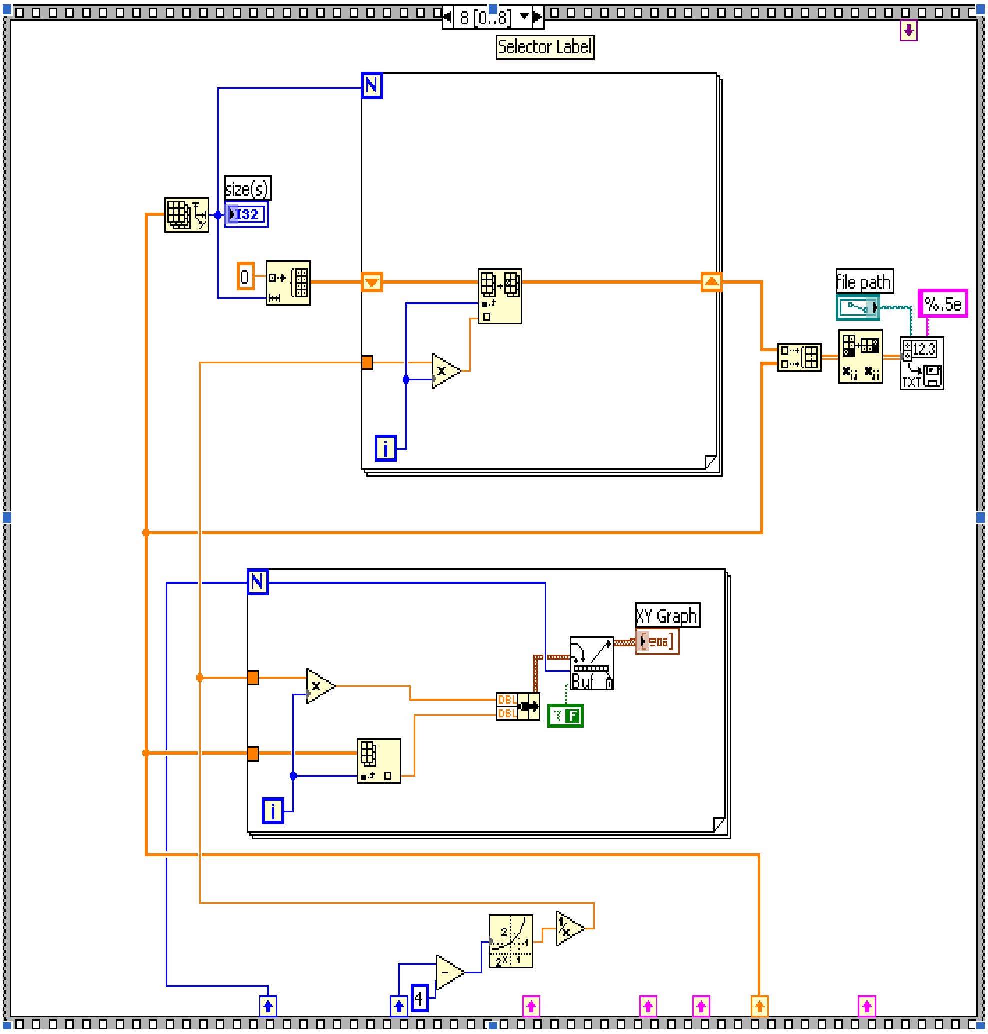

Fig. A-18: Once the data acquisition is finished, we plot the vibration amplitude of the oscillator versus time, and then we store the raw data into a data file.

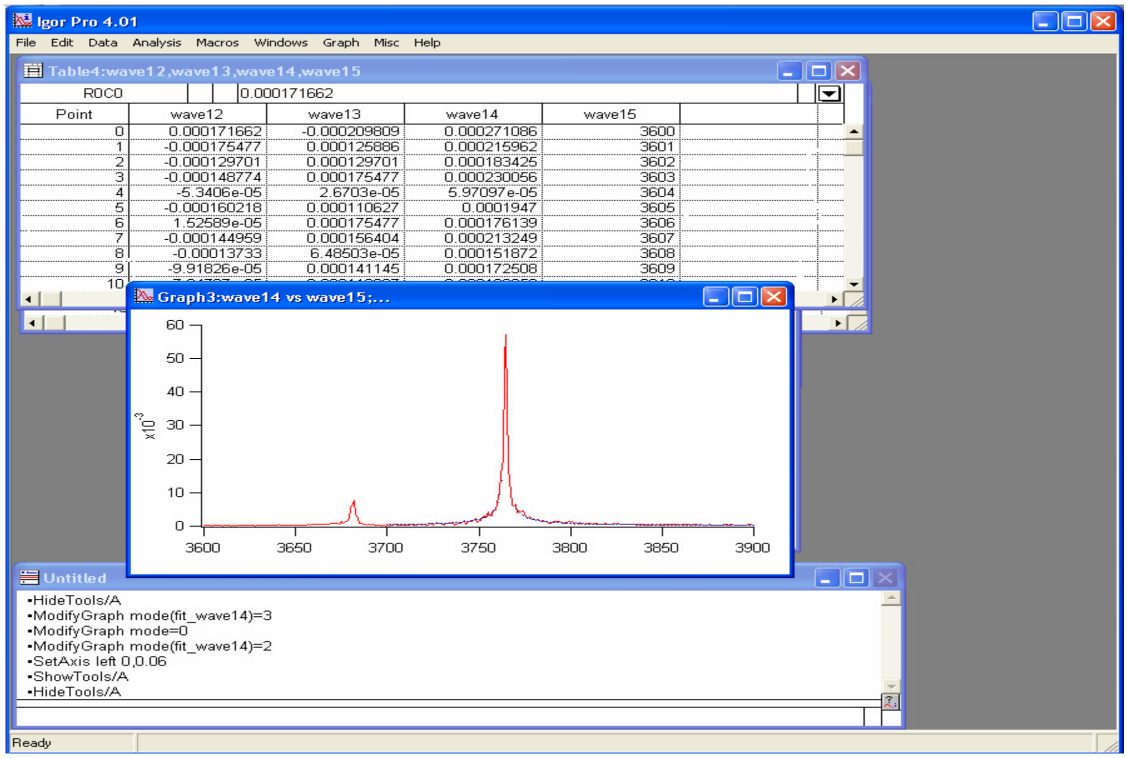

Point	wave12	wave13	wave14	wave15
0	0.000171662	-0.000209809	0.000271086	3600
1	-0.000175477	0.000125886	0.000215962	3601
2	-0.000129701	0.000129701	0.000183425	3602
3	-0.000148774	0.000175477	0.000230056	3603
4	-5.3406e-05	2.6703e-05	5.97097e-05	3604
5	-0.000160218	0.000110627	0.0001947	3605
6	1.52589e-05	0.000175477	0.000176139	3606
7	-0.000144959	0.000156404	0.000213249	3607
8	-0.00013733	6.48503e-05	0.000151872	3608
9	-9.91826e-05	0.000141145	0.000172508	3609
10				

```
•HideTools/A
•ModifyGraph mode(fit_wave14)=3
•ModifyGraph mode=0
•ModifyGraph mode(fit_wave14)=2
•SetAxis left 0,0.06
•ShowTools/A
•HideTools/A
```

Fig. A-19: The interface of Igor Pro 4.01 for data analysis.

Once we finish the data acquisition, we will do the data analysis by using Igor Pro 4.01. First we load raw data form data files in manner of waves into tables. And then we plot the relationships between physical quantities we are interested in from the top "windows" menu. Finally we can do the curve fitting for the waves by using the built-in mathematics functions or the new fit functions you customize. The bottom window shows the results of every operation, such as the curve fitting results.

Appendix B

B-1 The sawtooth waveform from the PCI 6711 DAQ (NI)

Fig. B-1 is the interface of Labview program for the sawtooth waveform generation.

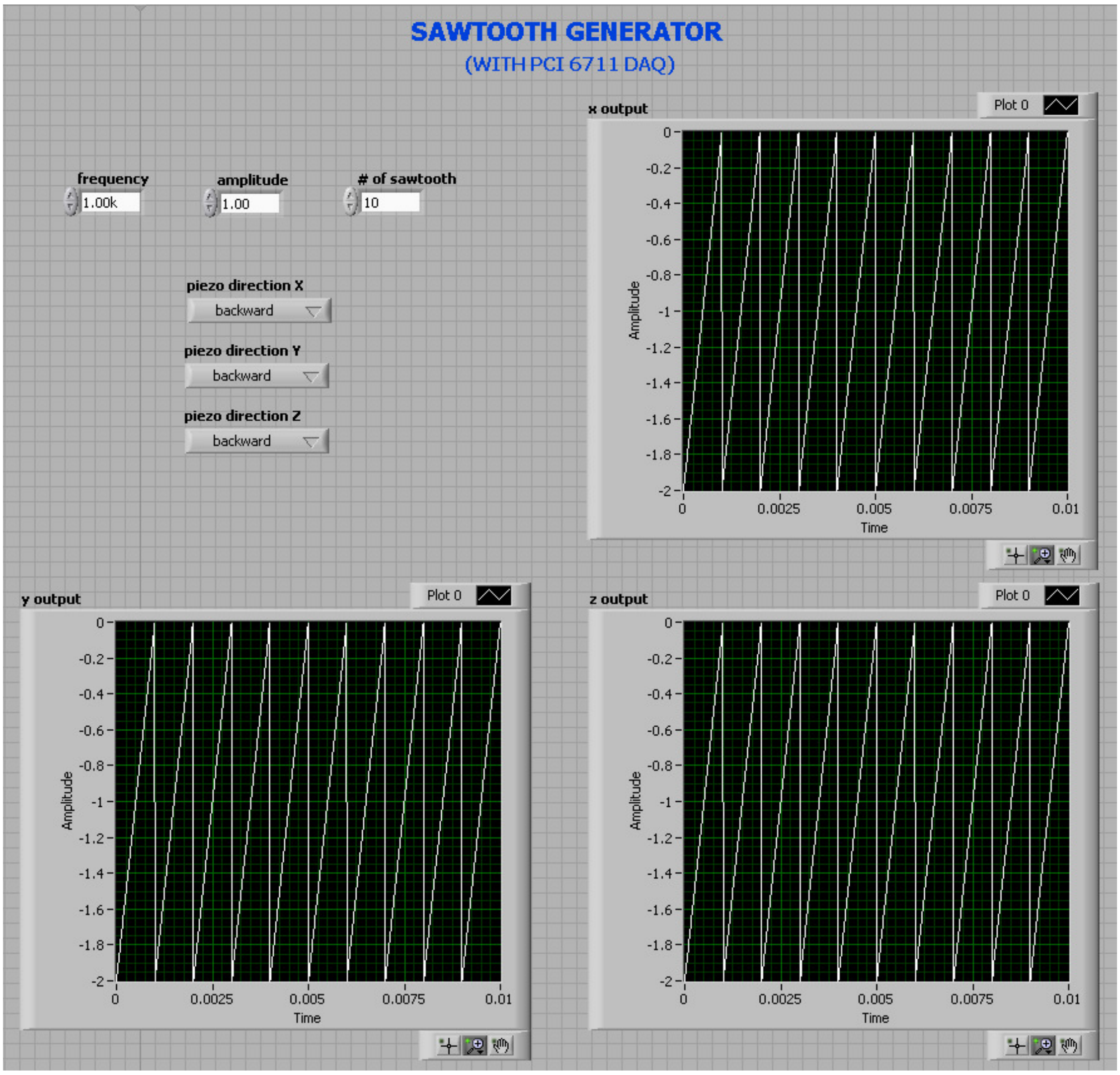

frequency 1.00k

amplitude 1.00

# of sawtooth 10

piezo direction X: backward

piezo direction Y: backward

piezo direction Z: backward

Fig. B-1: The graphic user interface of the sawtooth waveform generation program.

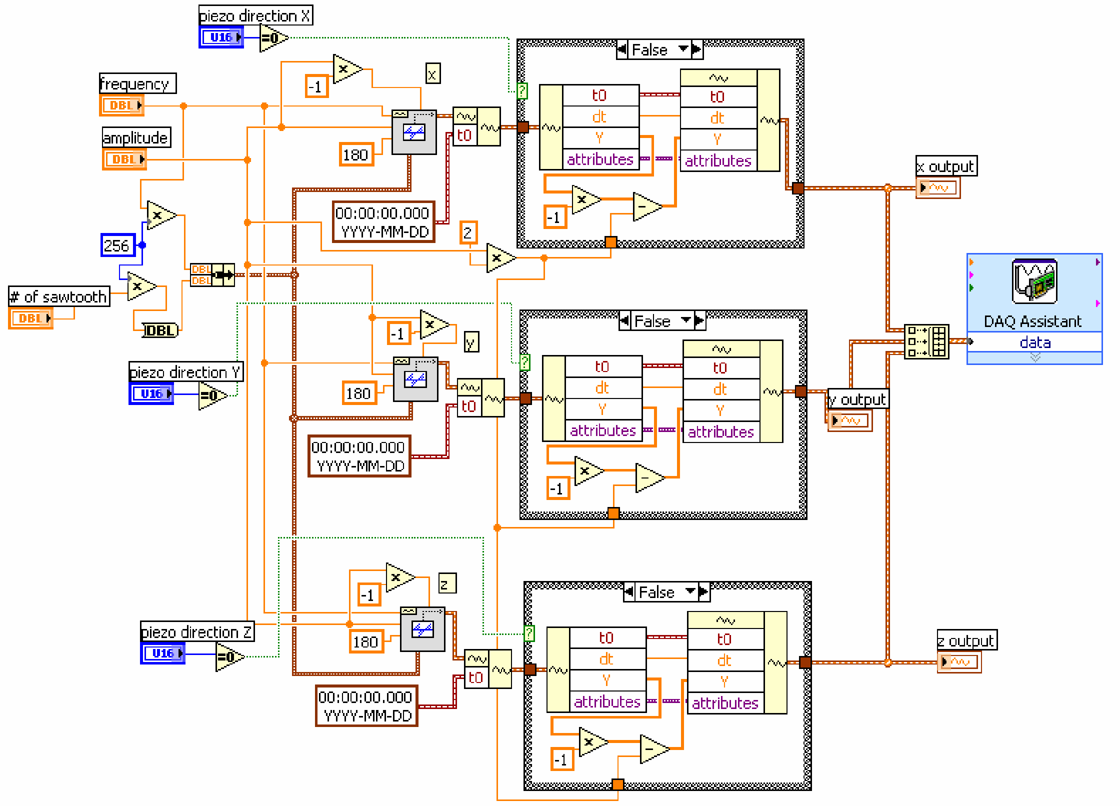

Fig. B-2: The block diagram of the program.

We generate multiple sawtooth waveforms, and send them to the PCI 6711 DAQ (National Instruments) via the DAQ Assistant. The DAQ Assistant is a graphical interface you use to configure measurement tasks and channels, and to customize timing, triggering, and scales without programming. It is a very useful tool provided by the Labview software. For the more usage of the DAQ assistant, please refer tutorial textbook of the Labview program, or go to the forum zone in National Instruments website: http://zone.ni.com/devzone

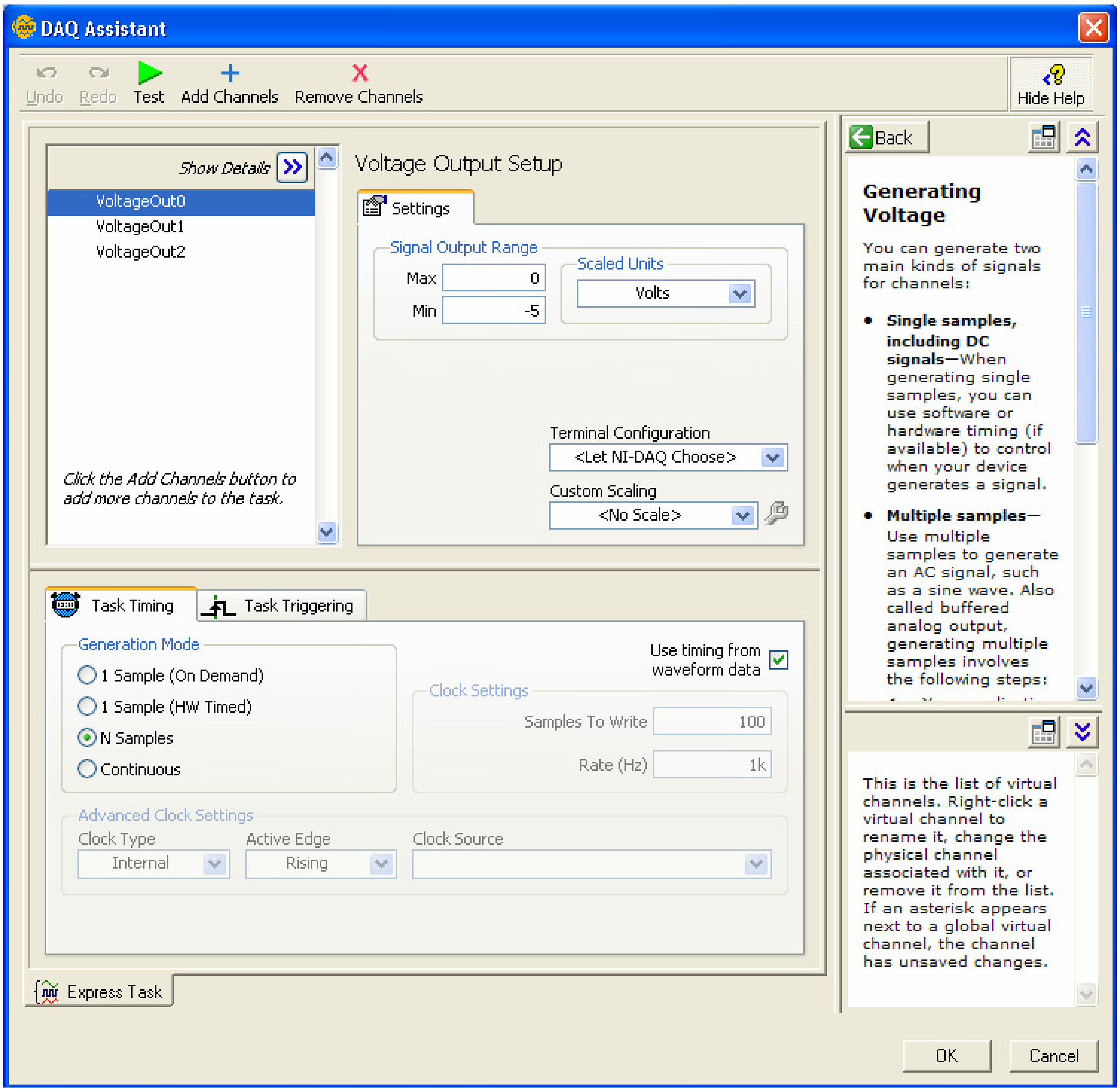

VoltageOut0
VoltageOut1
VoltageOut2

Click the Add Channels button to add more channels to the task.

Max 0
Min -5
Scaled Units: Volts
Terminal Configuration <Let NI-DAQ Choose>
Custom Scaling <No Scale>

○ 1 Sample (On Demand)
○ 1 Sample (HW Timed)
● N Samples
○ Continuous

Use timing from waveform data ☑
Samples To Write 100
Rate (Hz) 1k
Clock Type: Internal
Active Edge: Rising
Clock Source:

Generating Voltage

You can generate two main kinds of signals for channels:

- **Single samples, including DC signals**—When generating single samples, you can use software or hardware timing (if available) to control when your device generates a signal.
- **Multiple samples**—Use multiple samples to generate an AC signal, such as a sine wave. Also called buffered analog output, generating multiple samples involves the following steps:

This is the list of virtual channels. Right-click a virtual channel to rename it, change the physical channel associated with it, or remove it from the list. If an asterisk appears next to a global virtual channel, the channel has unsaved changes.

Fig. B-3: The interface of DAQ Assistant.

Through DAQ Assistant, we can generate the sawtooth waveforms from three channels simultaneously, and feed them to the x, y, and z positioning stage, respectively.

B-2 Sawtooth waveform from the programmed PIC16F84A microcontroller

We use the WinPicProg software to program the 8-bit PIC16F84A microcontroller. You can download this free software from http://www.winpicprog.com. The PIC16F84A microcontroller has 35 instructions, which control registers, memories, inputs and outputs of the microcontroller. We can use any C language compiler, such as Turbo C, C++ etc., to compile an original code. We show the original code of our sawtooth waveform generation as follows.

```
;==Header Section
processor 16F84A
#include <p16F84A.inc>
;===Equate Section==
TEMP equ 0x1C
COUNTER equ 0x1D
DELAY_COUNT equ 0x1E
COMPARE equ 0x1F
;===Vector Section==
org 0X005
goto Main
;===Initialization==
init
BSF STATUS,RP0
MOVLW 0xFF
```

```
MOVWF TRISA
movlw 0x00
;==0xFF for down ramp.==
movwf TRISB
BCF STATUS,RP0
CLRF PORTB
MOVLW 0x00
MOVWF COUNTER
CLRF DELAY_COUNT
MOVLW b'01111'
MOVWF COMPARE
return
;===Delay==
delay
movf DELAY_COUNT,W
movwf TEMP
delay_loop
NOP
decfsz TEMP,F
goto delay_loop
Return
;===One Ramp==
one_ramp
```

```
MOVF COUNTER,W
MOVWF PORTB
CALL delay
INCFSZ COUNTER, F
;==DECFSZ for down ramp==
GOTO one_ramp
CLRF PORTB
Return
;===Main==
Main
call init
WAIT BTFSS PORTA,4
goto WAIT
repeat
MOVF PORTA,W
ANDWF COMPARE,W
MOVWF DELAY_COUNT
INCF DELAY_COUNT,F
call one_ramp
BTFSS PORTA,4
goto WAIT
goto repeat
End
```

After compiling, an ASM file will be created. We burn this ASM file into the PIC16F84A memory using a programmer (shown in Fig. B-6), and convert it into an HEX file. After programming the PIC16F84A, the HEX File in the memory is:

```
281E 1683 30FF 0085 3000 0086 1283 0186

30FF 009D 019E 300F 009F 0008 081E 009C

0000 0000 0000 0000 0B9C 2810 0008 081D

0086 200E 0B9D 2817 0186 0008 2001 1E05

281F 0805 051F 009E 0A9E 2017 1E05 281F

2821
```

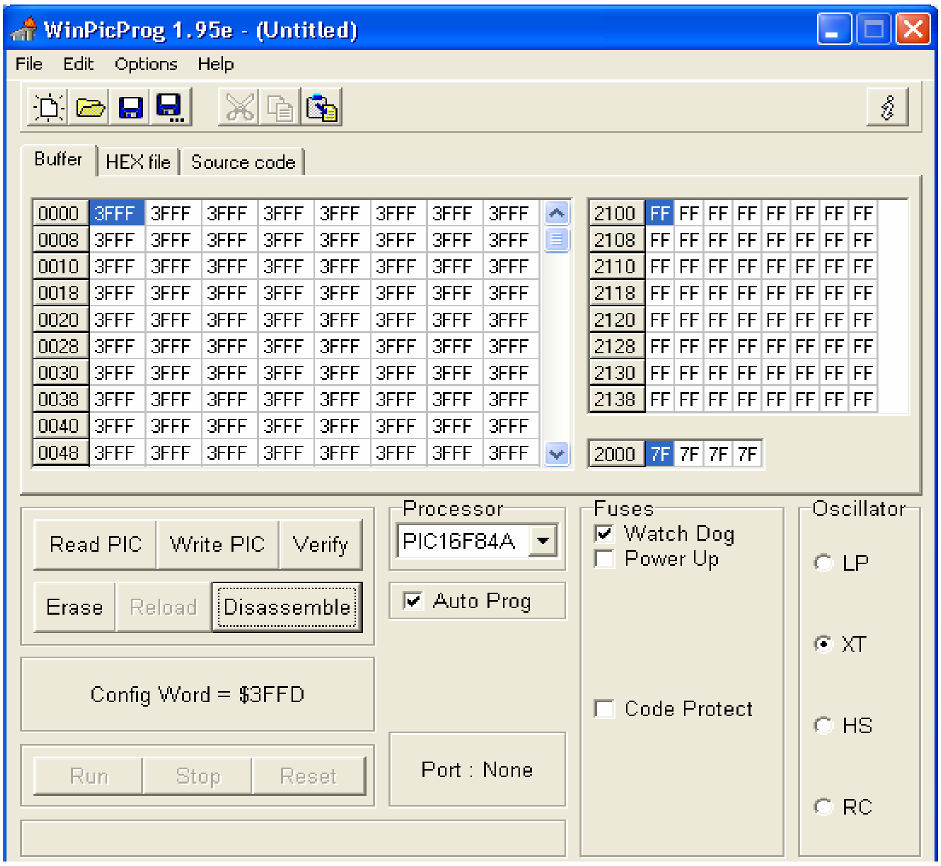

```
0000 3FFF 3FFF 3FFF 3FFF 3FFF 3FFF 3FFF 3FFF
0008 3FFF 3FFF 3FFF 3FFF 3FFF 3FFF 3FFF 3FFF
0010 3FFF 3FFF 3FFF 3FFF 3FFF 3FFF 3FFF 3FFF
0018 3FFF 3FFF 3FFF 3FFF 3FFF 3FFF 3FFF 3FFF
0020 3FFF 3FFF 3FFF 3FFF 3FFF 3FFF 3FFF 3FFF
0028 3FFF 3FFF 3FFF 3FFF 3FFF 3FFF 3FFF 3FFF
0030 3FFF 3FFF 3FFF 3FFF 3FFF 3FFF 3FFF 3FFF
0038 3FFF 3FFF 3FFF 3FFF 3FFF 3FFF 3FFF 3FFF
0040 3FFF 3FFF 3FFF 3FFF 3FFF 3FFF 3FFF 3FFF
0048 3FFF 3FFF 3FFF 3FFF 3FFF 3FFF 3FFF 3FFF

2100 FF FF FF FF FF FF FF FF
2108 FF FF FF FF FF FF FF FF
2110 FF FF FF FF FF FF FF FF
2118 FF FF FF FF FF FF FF FF
2120 FF FF FF FF FF FF FF FF
2128 FF FF FF FF FF FF FF FF
2130 FF FF FF FF FF FF FF FF
2138 FF FF FF FF FF FF FF FF

2000 7F 7F 7F 7F
```

Processor: PIC16F84A

☑ Auto Prog

Config Word = $3FFD

Port : None

Fuses: ☑ Watch Dog ☐ Power Up ☐ Code Protect

Oscillator: ○ LP ● XT ○ HS ○ RC

Fig. B-4: The Interface of WinPicProg software for programming the PIC16F84A.

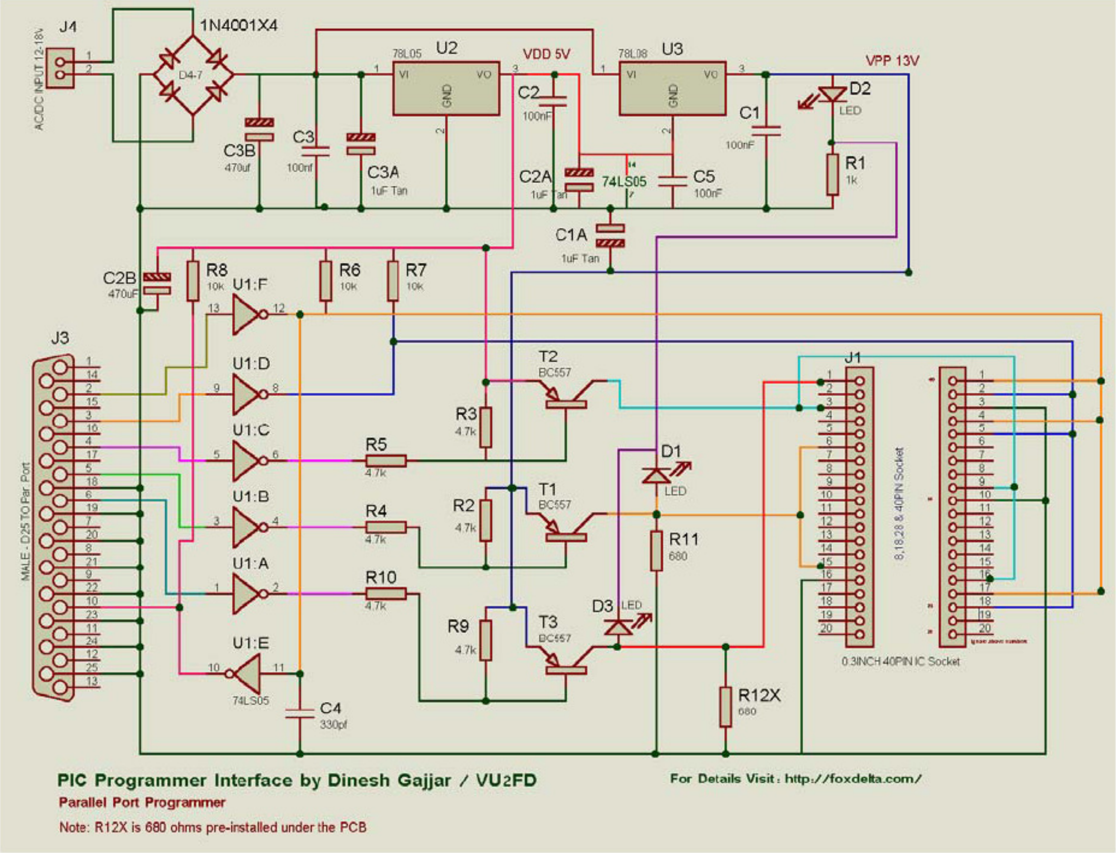

Fig. B-5: Schematic of the programmer for the PIC16F84A microcontroller.

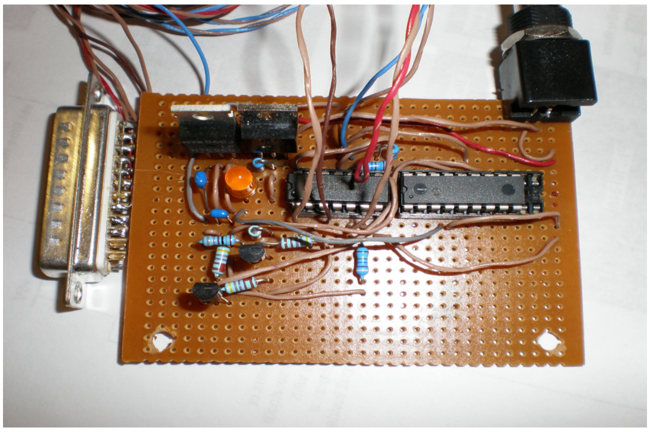

Fig. B-6: Assembly code programmer for PIC16F84A microcontroller.

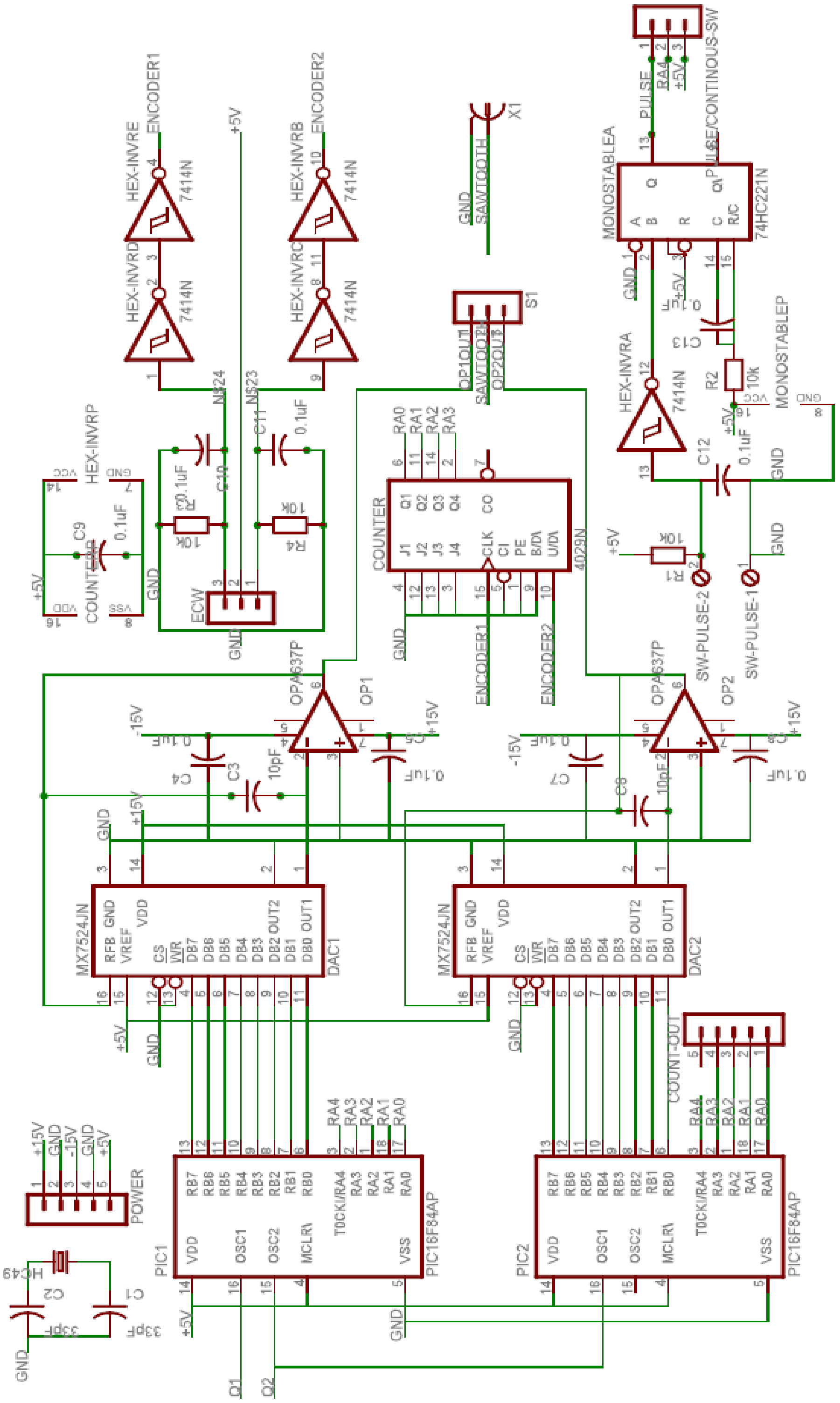

Fig. B-7: Schematic drawing of the sawtooth waveform generator by programming the PIC16F84A.

Appendix C

Fig. C-1 is the interface of the Labview program for gold micromass measurements.

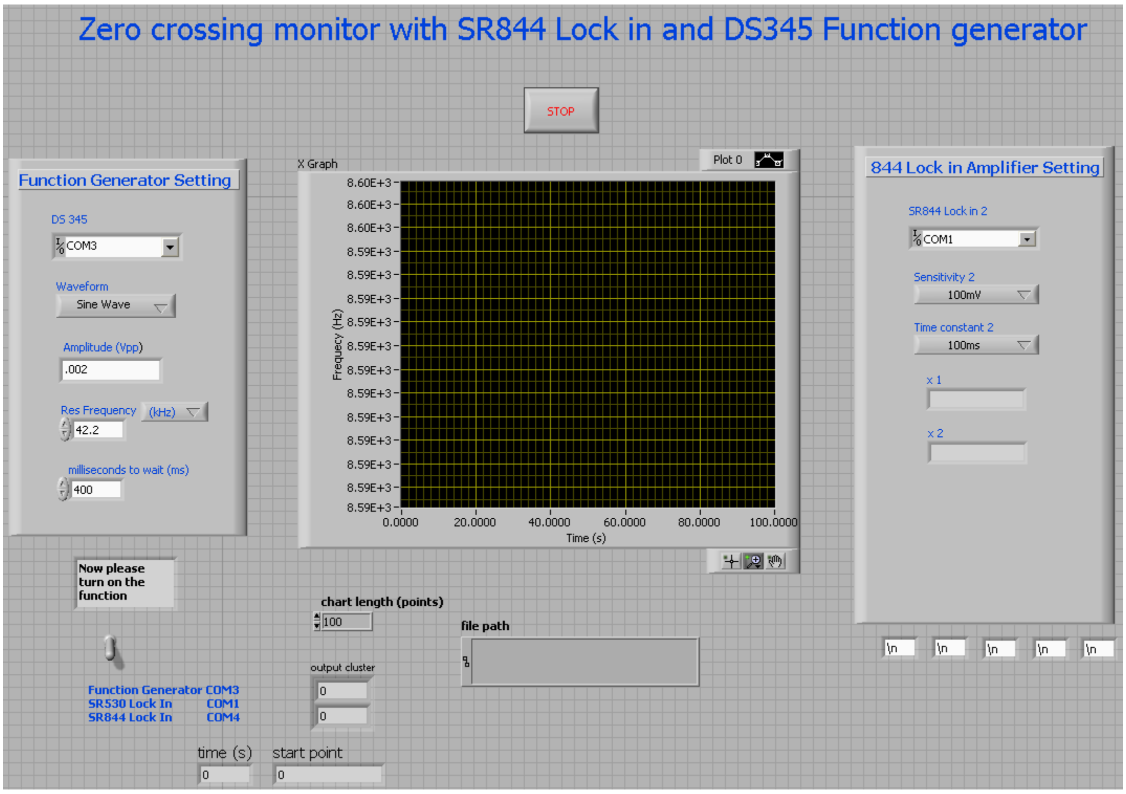

Zero crossing monitor with SR844 Lock in and DS345 Function generator

Function Generator Setting

DS 345: COM3

Waveform: Sine Wave

Amplitude (Vpp): .002

Res Frequency (kHz): 42.2

milliseconds to wait (ms): 400

Now please turn on the function

Function Generator COM3
SR530 Lock In COM1
SR844 Lock In COM4

chart length (points): 100

output cluster: 0, 0

time (s): 0

start point: 0

844 Lock in Amplifier Setting

SR844 Lock in 2: COM1

Sensitivity 2: 100mV

Time constant 2: 100ms

Fig. C-1: The interface of the Labview program for gold micromass measurements. In this program, we monitor the zero-crossing of the X output from the lock-in, and adjust the frequency to maintain the zero crossing.

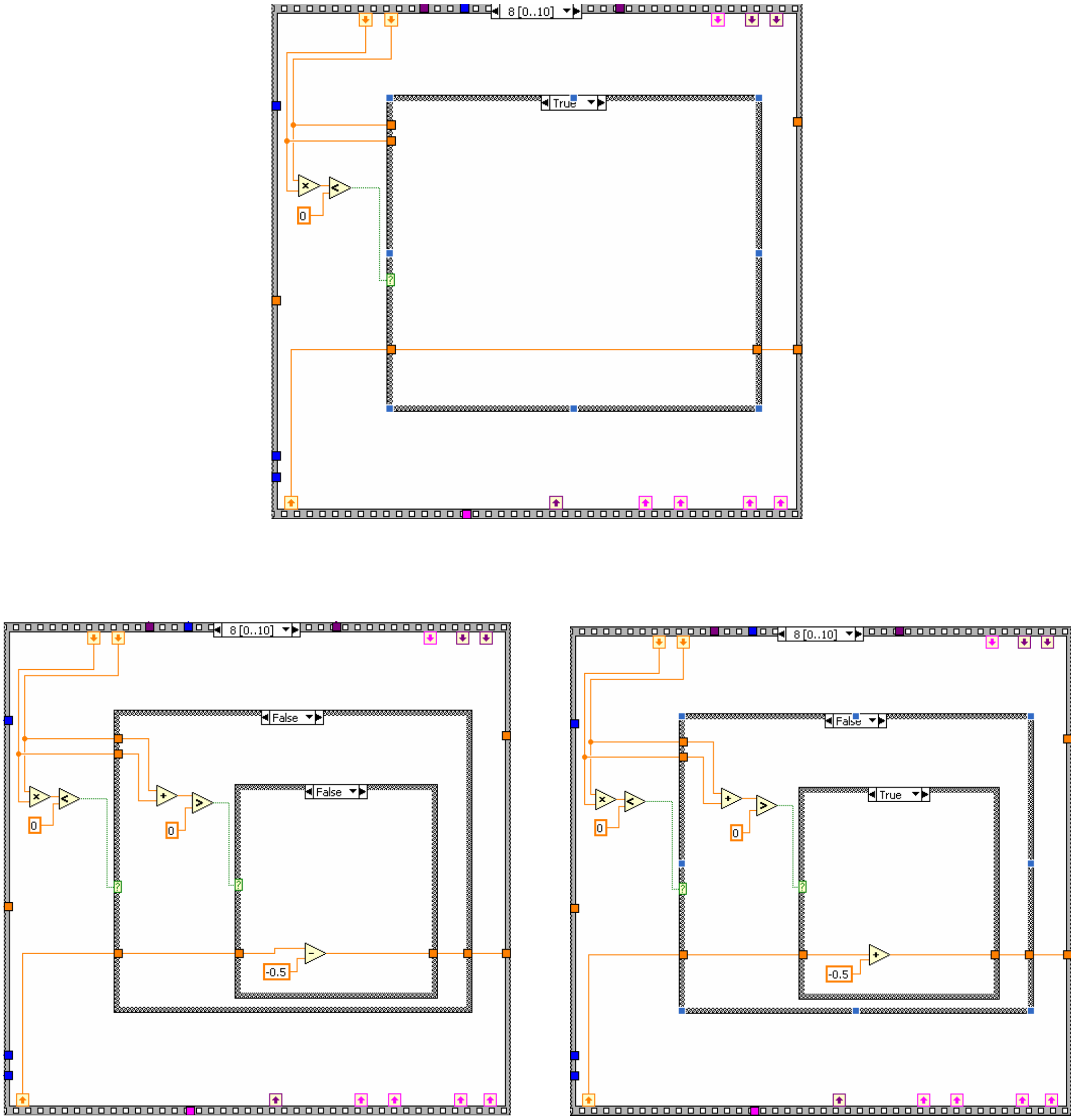

Fig. C-2: If the reference frequency is below the resonance frequency, then the X output will be negative, when the reference frequency is above the resonance frequency, then the X output will be positive. So once the Labview program found the X went to negative, this feedback signal will make the program increase the reference frequency by a small value (e.g 0.5 Hz or 1 Hz), and vice versa.

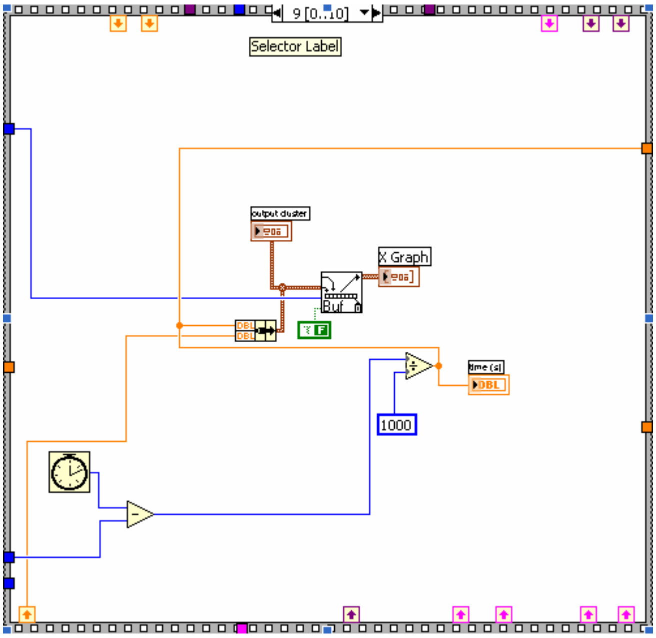

Fig. C-3: We plot the frequency as a function of the time. From the small frequency shift of a mechanical oscillator, we can estimate the extremely small gold mass evaporated on an mechanical oscillator.

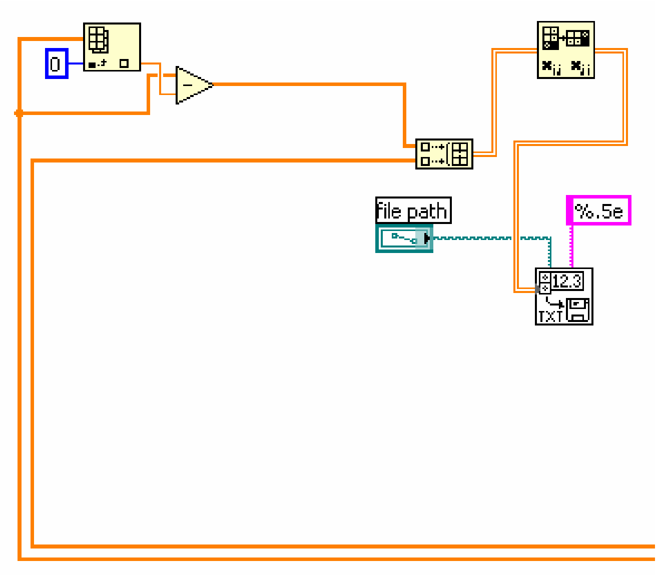

Fig. C-4: Save raw data into a data file for data analysis.

Bibliography

[1] J. A. Sidles, Phys. Rev. Lett, **68**, 1124 (1992).

[2] J. A. Sidles, J. L. Garbini, and G. P. Drobny, Rev. Sci. Instrum. **8**, 3881 (1992).

[3] D. Rugar, C. S. Yannoni, and J. A. Sidles, Nature **363**, 563 (1992).

[4] O. Zuger and D. Rugar, Appl. Phys. Lett. **63**, 2496 (1993).

[5] K. Wago, D. Botkin, and D. Rugar, Phys. Rev. B. **57**, 1108 (1998).

[6] K. Wago, O. Zuger, J. Wegener, R. D. Kendrick, C. S. Yannoni, and D. Rugar, Rev. Sci. Instrum. **68**, 1823 (1997).

[7] K. J. Bruland, J. Krzystek, J. L. Garbini, and J. A. Sidles, Rev. Sci. Instrum. **66**, 2853 (1995).

[8] G. Tobias, Master thesis, The Univeristy of Texas at Austin, 1998.

[9] K. Y. Yasumura, T. D. Stowe, and D. Rugar et al., J. Micro.S. **9**, 117 (2000).

[10] T. B. Gabrielson, IEEE Trans. Eletron Devices, **40**, 903 (1993)

[11] X. Liu, S. F. Morse, J. F. Vignola, and D. M. Photiadis, A. Sarkissian, et, al., Appl. Phys. Lett. **78**, 1346 (2001)

[12] B. H. Houston, D. M. Photiadis, M. H. Marcus, J. A. Bucaro, and X. Liu, Appl. Phys. Lett. **80**, 1300 (2001)

[13] D. A. Walters, J. P. Cleveland, N. H. Thomson, and P. K. Hansma, Rev. Sci. Instrum. **66**, 2853 (1995).

[14] C. W. Miller, Ph.D. thesis, The Univeristy of Texas at Austin, 2003.

[15] T. D. Stowe, K. Y. Yasumura, T. K. Kenny, D. Botkin, K. Wago, and D. Rugar,

Appl. Phys. Lett. **71**, 288 (1997)

[16] M. D. Chabot, Ph.D. thesis, The Univeristy of Texas at Austin, 2001.

[17] M. D. Chabot and J. T. Markert, Proceedings of SPIE: Materials in Device Characterization in Micromachining II, **3875**, 104 (1999).

[18] M. D. Chabot, T. C. Messina, V. Mancevski, C. W. Miller, and J. T. Markert, Proceedings of SPIE: MEMS Components and Applications to Industry, **4559**, 24 (2001).

[19] J. H. Choi, U. M. Mirsaidov, C. W. Miller, Y. J. Lee, S. Guchhait, M. D. Chabot, W. Lu, and J. T. Markert, Proceedings of SPIE: Smart Electronics, MEMS, BioMEMS, and Nanotechnology, (2004).

[20] M. D. Chabot, J. M. Moreland, L. Gao, S. H. Liou, and C. W. Miller, J. Microelectromech. Syst, (2005).

[21] K. R. Williams and R. S. Muller, J. Microelectromech. Syst, **5**, 256 (1996).

[22] K. R. Williams et al., J. Microelectromech. Syst, **12**, 761 (2003).

[23] K. Biswas and S. Kal, Microelectronics Journal, **37**, 519 (2006).

[24] O. Tabata, R. Asahi, H. Funabashi, K. Shimaoka and S. Sugiyama, Sens. Actuators **A34,** 51 (1992).

[25] P. Hei et al., Sens. Actuators**. A93**, 132 (2001).

[26] E. Palik and O. Glembocki, J. Appl. Phys. **70**, 3291 (1991).

[27] J.T.L. Thong, W.K. Choi and C.W. Chong, Sens. Actuators. **A63**, 243 (1997).

[28] Weste, Neil H. E., *CMOS VLSI design : a circuits and systems perspective*, Boston : Pearson/Addison-Wesley, (2005).

[29] I. Barycka and I. Zubel, Sens. Actuators**. A70** 250 (1998).

[30] H. Seidel, L. Csepregi, A. Heuberger and H. Baumgartel, J. Electrochem. Soc. **137,** 3612 (1990).

[31] W. R. Runyan and K. E. Bean, *Semiconductor Integrated Circuit Process Technology*, MA: Addison-Wesley (1990).

[32] HTTP://www.microchem.com/products/pdf/PMMA_Data_Sheet.pdf

[33] HTTP://www.azonano.com/

[34] S. K. Ghandi, *VLSI Fabrication Principles*, New york: Wiley, (1983).

[35] H. Kikuama, N. Miki, and S. Saka et al., Trans. Semicond. Manufact. **4**, 26 (1991)

[36] J. S. Judge, J. Electrochem. Soc, **118**, 1772 (1971).

[37] D. L. Kendall, J. Vac. Sci. Technol. A. **8**, 3598 (1990).

[38] H. Seidel et al., J. Electrochem. Soc, **137**, 3626 (1990).

[39] C. V. Macchioni, J. Vac. Sci. Technol. A. **9**, 2302 (1991).

[40] L. Stiharu, R. Bhat, M. Kahrizi, and L. Landsberger, Proc. SPIE. **2015**, 254 (1993).

[41] A. E. T. Kuiper and E. G. C. Lathouwears, J. Electrochem. Soc, **139**, 2594 (1992).

[42] M. Wong, M. Moslehi, and R. A. Bowling, J. Electrochem. Soc, **140,** 205 (1993).

[43] D. W. Pohl, Rev. Sci. Instrum. **58 (1)**, 54 (1987).

[44] J. W. G. Wildoer, et al., Rev. Sci. Instrum. **65 (9)**, 2849 (1987).

[45] Karrai, US Patent 5912527 Issued on 1999.

[46] R. Euler, U. Memmert, and U. Hartmann, Rev. Sci. Instrum. **68 (4)**, 1776 (1997)

[47] S. H. Pan, E. W. Hudson, and J. C. Davis, Rev. Sci. Instrum. **70 (2)**, 1459 (1999)

[48] S. H. Pan, Intrenational Patent Publication Number WO 93/19494 (International Bureau, World Intellectual Property Oraganization), Sept, 30, 1993

[49] HTTP://www.attocube.com/nanoPOSITIONING/nanopositioning.htm

[50] C. Meyer, O. Sqalli, and K. Karrai, Rev. Sci. Instrum. **76**, 063706 (2005).

[51] Y. J. Lee, Ph.D. thesis, The Univeristy of Texas at Austin, 2006.

[52] T. M. Chunag, Ph.D. thesis, The Univeristy of Texas at Austin, 2006.

[53] D. Besson, L. Bardotti, A. Hoareau, B. Prével, M. Treilleux, and C. Esnouf, Materials Science and Engineering B, **60**, 51 (1999)

[54] A. J. Perrotta, D. K. Grubbs, W. H. Quayle, T. B. Gurganus, US Patent 4892693 Issued on January 9, 1990

[55] A. Singh, J. Phys. E: Sci. Instrum. **10,** 960 (1997)

[56] S. M. Vaezi-Nejad, Selected Topics in Advanced Solid State and Fibre Optic, Chap 7, pp 221 (2000).

Vita

Wei Lu was born in Lanzhou, P. R. China, on November 16, 1975, the son of Shaoquan Chen and Chunyi Lu. When he was a child, he was very interested in fine arts, mathematics and physics.

He received the Bachelor of Science degree in Physics from the University of Science and Technology of China in Hefei in June 1998. During his 4 years of study, he did his undergraduate research on the nonlinear plasma physics under Prof. Yinhua Chen. After his undergraduate study, he entered the graduate school of the University of Science and Technology of China in the same year and continued the research on nonlinear plasma physics by numerical calculation methods under the guide of Prof. Yinhua Chen. He received the Master of Science degree in Physics from the University of Science and Technology of China in June 2001.

After graduating from the University of Science and Technology of China in 2001, he was accepted and started graduate studies at the University of Texas at Austin in 2001. Instead of continuing the computational physics on nonlinear plasma physics, he switched to the experimental physics. In 2002, he joined the Nuclear Magnetic Resonance Force Microscopy (NMRFM) group in Dr. Markert's lab and focused on the design, fabrication, characterization, and application of mechanical oscillators for use in NMRFM.

Permanent address: 10306 Morado Cove, APT 252, Austin, Texas 78759

This dissertation was typed by the author